

RAPID PARAMETER ESTIMATION OF GRAVITATIONAL WAVE
SOURCES & HOMOLOGOUS EXPANSION IN COMMON ENVELOPE
EVENTS

by

Vinaya Valsan

A Dissertation Submitted in
Partial Fulfillment of the
Requirements for the Degree of

Doctor of Philosophy

in Physics

at

The University of Wisconsin-Milwaukee

August 2024

ABSTRACT

RAPID PARAMETER ESTIMATION OF GRAVITATIONAL WAVE SOURCES & HOMOLOGOUS EXPANSION IN COMMON ENVELOPE EVENTS

by

Vinaya Valsan

The University of Wisconsin-Milwaukee, 2024

Under the Supervision of Professor Patrick Brady, Jolien Creighton, and Philip Chang

Binary star systems are crucial for advancing our understanding of the universe. My doctoral research focuses on two related topics within the domain of binary star dynamics: gravitational waves from compact binary stars, and the evolution of the common envelope in stellar mass binaries.

In the era of multi-messenger astrophysics, swift identification and characterization of gravitational wave events is important for subsequent electromagnetic observations. The development of low-latency parameter estimation techniques is essential for providing astronomers with crucial information regarding the potential electromagnetic counterparts to gravitational wave signals. RapidPE is a highly parallelized parameter estimation scheme that achieves low-latency parameter estimation by limiting the intrinsic parameter space to a grid and utilizing Monte Carlo sampling in the extrinsic parameter space. My work introduces an improved intrinsic grid placement scheme called Adaptive Mesh Refinement (AMR) for RapidPE, enabling it to efficiently compute posterior distributions for intrinsic parameters by prioritizing computation in high-likelihood regions and overcoming biases from gravitational wave detection pipelines. With AMR, RapidPE can produce reliable source classification and posterior probability distribution for gravitational wave events within a minute with GPUs.

Common envelope evolution (CEE) is a phase in the evolution of a binary star system

where two stars orbit inside a shared gaseous envelope and is crucial for the formation of many systems of astrophysical interest. Despite its importance, CEE is not well understood due to the complexity of the physics involved and the different timescales of its evolution. These complexities pose challenges for both simulation and observation of CEE. Once a system enters a Common Envelope phase, uncertainties persist regarding whether it ends in a merger and/or envelope ejection as well as the timescale and efficiency of the envelope ejection. To address these questions, I conduct a long timescale 3D simulation of a CEE using the moving-mesh hydrodynamic solver MANGA. This work shows that, if evolved long enough, complete envelope ejection can be achieved with solely the orbital energy alone without the need for reheating from recombination or jets. Additionally, the envelope enters a phase of homologous expansion in our simulation. This homologous expansion of the envelope would likely simplify calculations of the observational implications such as light curves.

© Copyright by Vinaya Valsan, 2024
All Rights Reserved

To my parents.

TABLE OF CONTENTS

Abstract	ii
List of Figures	ix
List of Tables	xiii
List of Symbols and Abbreviations	xiv
Acknowledgements	xvi
1 Introduction	1
1.1 Gravitational Waves	1
1.1.1 GW150914: First Detection of GW	3
1.1.2 GW170817 and GRB170817A: Multi-Messenger Astronomy	3
1.1.3 Third Observing Run	5
1.1.4 In this Dissertation	6
1.2 Common Envelope Evolution	6
1.2.1 In this Dissertation	8
2 Parameter Estimation with Gravitational Waves	10
2.1 Gravitational Wave under linearized gravity approximation	13
2.2 Gravitational Wave Strain and Detector Data	16
2.2.1 Intrinsic and Extrinsic Parameters	16
2.2.2 GW Strain at the detector	18
2.3 Bayesian Inference in Parameter Estimation	18

2.3.1	Likelihood Ratio	21
2.4	Rapid Parameter Estimation	22
2.4.1	Waveform Decomposition	23
2.4.2	Likelihood	25
2.4.3	Intrinsic Grid	26
2.4.4	Extrinsic Sampling	26
2.5	Limitation of Fischer Matrix Scheme of RapidPE	28
3	Adaptive Mesh Refinement in RapidPE	29
3.1	Initial Region Identification and Grid Placement Algorithm	30
3.2	Likelihood Interpolation	33
3.3	Testing on Simulated GW Events	34
3.3.1	Comparing different grid placement schemes	35
3.3.2	Validation of AMR RapidPE	38
3.4	Conclusion	43
4	Rapid Parameter Estimation in O4	44
4.1	Low-Latency pipelines in O4	45
4.2	RapidPE-RIFT	46
4.3	P-Astro: Source Classification	50
4.3.1	Comparison with Search Pipeline P-Astro	53
4.4	AMR RapidPE-RIFT in O4	54
5	Common Envelope Evolution	59
5.1	Overview	59
5.1.1	Phases of CEE	61
5.1.2	Energy Formalism	63

5.2	Observations	66
5.3	Simulating CEE	68
5.3.1	Equations of Hydrodynamics	68
5.3.2	Smooth Particle Hydrodynamics	69
5.3.3	Eulerian Grid Codes	70
5.3.4	Arbitrary Lagrangian-Eulerian Schemes	71
5.4	CEE: An Extraordinary Physics Problem	73
6	Envelope Ejection and Homologous Expansion	75
6.1	Numerical Setup	76
6.1.1	Initial Conditions	77
6.2	Results	78
6.2.1	Homologous Expansion	83
6.2.2	1-D Model	90
6.3	Discussion	98
7	Conclusion	102
7.1	Rapid parameter estimation of Gravitational Waves	102
7.1.1	Current and Future Work	103
7.2	Envelope Ejection and Transition to Homologous Expansion in Common Envelope Evolution	104
7.2.1	Current and Future Work	105
	Bibliography	106

LIST OF FIGURES

- 3.1 The top three panels represent a fiducial cell and inset grid point (blue), a single level of refinement (red), and a second level of refinement (green). The bottom three panels display the same procedure, but with a split initial region to highlight the interlocked but overlapping refined cells. In all cases, the black cells are the previous level underlaid for reference. Grid points that have already been evaluated (the center point, zero offset refined cell) are not included in the next refinement level. 32
- 3.2 This figure shows the logarithm of the reduced likelihood obtained through marginalization scatter plotted against \mathcal{M}_c and η for event #10184. The left panel is the result of the prerenement method, the middle is the (pruned) serial grid refinement method, and the right is the Fisher matrix method. The magenta cross marks the search-identified point from which the intrinsic grid was computed, while the red x marks the injected parameters. In this figure, the contour represents the posterior obtained from `lalinference_mcmc`. The squares, circles, and triangles indicate the first, second, and third grid levels, respectively. 36

3.3	This figure shows the logarithm of the reduced likelihood obtained through marginalization scatter plotted against \mathcal{M}_c and η for event #14631. The left panel is the result of the preresinement method, the middle is the (pruned) serial grid refinement method, and the right is the Fisher matrix method. The magenta cross marks the search-identified point from which the intrinsic grid was computed, while the red x marks the injected parameters. In this figure, the contour represents the posterior obtained from <code>lalinference_mcmc</code> . The squares, circles, and triangles indicate the first, second, and third grid levels, respectively.	37
3.4	Intrinsic posterior plots of event #10184 for three grid levels of the preresine scheme. The blue posterior is from RapidPE and the black posterior is from <code>lalinference_mcmc</code> . The red lines indicate the injected values, while the green lines indicate the search-recovered values.	39
3.5	Intrinsic posterior plots of event #14631 for three grid levels of the refine (prune) scheme. The blue posterior is from RapidPE and the black posterior is from <code>lalinference_mcmc</code> . The red lines indicate the injected values, while the green lines indicate the search-recovered values.	40
3.6	AMR RapidPE results on 100 three-detector F2Y 2016 injections for the serial refinement method with three grid levels. The colored lines represent the fraction of events within a given confidence interval (C.I.) for intrinsic and extrinsic parameters. The gray regions mark the cumulative 1-, 2-, and 3- σ confidence intervals in order of decreasing opacity.	42
4.1	Histogram of runtime using RIFT's ILE (with GPU and distance marginalization) on AMR RapidPE estimated for 29 events from O4 each using a 5×5 initial grid for intrinsic parameters with one level of refinement.	47

4.2	Sankey Diagrams comparing the source classification from RapidPE and GstLAL in count and percentage.	49
4.3	Histogram of runtime for AMR RapidPE-RIFT for events in O4. The red dashed line represents the mean of the histogram.	55
4.4	Comparison between P-Astro from PyCBC and AMR RapidPE-RIFT taken from GraceDB for the event S240413p in O4b	56
5.1	Examples of evolutionary channels of some binary star systems involving common envelope phase, reprinted from Ivanova et al. (2013)	60
6.1	Projection of density on to the $x - z$ plane (left panel) and $x - y$ plane (right panel) at different time slices (503 d, 1006 d, 2013 d) from the simulation. The '+' sign marks the center of mass of the system.	79
6.2	Smoothed separation between the center of mass of the red giant and the main-sequence star as a function of t . There is an initial rapid plunge of the two centers toward each other, but this plateaus to about $5 R_{\odot}$ after 200 d.	80
6.3	Fraction of unbound mass, f_{unb} , as a function of time, t . We only consider the mechanical energy in this case.	82
6.4	Radial velocity (top) and scaled density (bottom) as a function of scaled radius for different times (2000 d, 2500 d and 3000 d). We also show a power-law fit (solid black line) for $v_r \propto r_s^{0.86}$ (top).	86
6.5	The fractional change in the velocity of all particles compared to the final average velocity as a function of time. The dashed line represents the mean and the shaded area represents the standard deviation of the fractional change in the particle velocity.	87
6.6	Ratio of thermal energy to kinetic energy as a function of time.	88

6.7	Mean density ($\bar{\rho}$) of the envelope as a function of t (blue solid curve). The black dotted curve is the t^{-3} fit and is fitted for $t \in [500, 2000]$ d. Note that the average density profile follows a t^{-3} power-law closely.	91
6.8	Scaled density, ρ_s as a function of scaled radius, r_s from 1-D simulations, for 10 (red), 20 (blue), 50 (magenta), and 100 (yellow) yr and a heating parameter of $\lambda = 1$	92
6.9	Radial velocity, v_r , as a function of scaled radius from 1-D simulations. The times and λ are the same as in Figure 6.8. The solid black line is the best fit of $v_r \propto r_s^{0.95}$	93
6.10	Scaled density (ρ_s) and radial velocity (v_r) as a function of scaled radius (r_s), for 10 yr and different heating parameters λ	97

LIST OF TABLES

4.1	Data for Sankey Diagrams	50
-----	------------------------------------	----

LIST OF ABBREVIATIONS

AGN	Active Galactic Nuclei
ALE	Arbitrary Lagrangian Eulerian
AMR	Adaptive Mesh Refinement
BBH	Binary Black Hole
BH	Black Hole
BNS	Binary Neutron Star
CBC	Compact Binary Coalescence
CE	Common Envelope
CEE	Common Envelope Evolution
CHANGA	Charm N-body GrAvity solver
CO WD	Carbon-Oxygen White Dwarf
CSPNe	Central Star of Planetary Nebulae
EM	electromagnetic
F2Y	First 2 Year mock data challenge
GRB	Gamma-Ray Burst
GW	Gravitational Wave
GWTC	Gravitational- Wave Transient Catalog
ILOT	Intermediate Luminosity Optical Transients
KDE	Kernal Density Estimation
LIGO	Laser Interferometer Gravitational-wave Observatory
LRN	Luminous Red Novae
MANGA	moving-mesh CHANGA

MC	Monte Carlo
MCMC	Markov-Chain Monte Carlo
MESA	Modules for Experiments in Stellar Astrophysics
MM	Moving Mesh
MS	Main Sequence
NS	Neutron Star
NSBH	Neutron Star Black Hole
O1	first observing run
O2	second observing run
O3	third observing run
O4	fourth observing run
O4a	first half of fourth observing run
O4b	second half of fourth observing run
PNe	Planetary Nebulae
RGB	Red-Giant Branch
sGRB	short Gamma-Ray Burst
SPH	Smoothed-Particle Hydrodynamics
WD	White Dwarf

ACKNOWLEDGMENTS

I sincerely thank my advisors, Patrick R. Brady, Jolien Creighton, and Philip Chang, at UWM for their exceptional guidance, unwavering support, and constant encouragement. Thank you for allowing me to explore various research areas and participate in multiple projects that constitute this dissertation.

Part of this work was conducted as a member of the LIGO Scientific Collaboration (LSC). I acknowledge the support from the NSF through grants PHY-1912649 and PHY-2207728. I acknowledge the use of computing resources of the LIGO Data Grid and facilities provided by the Leonard E. Parker Center for Gravitation, Cosmology, and Astrophysics (CGCA) at the University of Wisconsin-Milwaukee (UWM). Simulations in Chapter 6 were completed on the Mortimer HPC System at UWM, funded by the NSF Campus Cyberinfrastructure Award OAC-2126229 and UWM.

I would like to thank my collaborators Caitlin Rose, Anarya Ray, Sarah Villanova Borges, and Logan Prust for their contributions to this work. Special gratitude is extended to Daniel Wysocki and Cody Messick for their guidance and contributions to this work.

Completing this PhD would not have been possible without the exceptional support, resources, and environment provided by the Department of Physics and CGCA at UWM. Thanks to Heidi Matera and Kate Valerius for their invaluable assistance.

I would also like to express my gratitude to Kavya and her family for their support throughout this journey.

Lastly, and most importantly, I owe my deepest gratitude to my parents, my husband, and my brother for their endless love and encouragement.

CHAPTER 1

Introduction

Binary star systems are crucial for advancing our understanding of the universe. They play an important role in the formation of many widely studied phenomena in the universe such as Compact Binary Coalescence, Gamma Ray Bursts, X-ray binaries, Type 1a supernovae, cataclysmic variables, etc. Binaries are as common as single stars in the universe ([Duchêne & Kraus, 2013](#)). Within the population of stars that complete their nuclear evolution in Hubble Time the fraction of stars in binary system varies from 40% – 60% for stellar mass stars ($M \approx M_{\odot}$) to almost 100% for more massive stars ([Duquennoy & Mayor, 1991](#); [Raghavan et al., 2010](#); [Chini et al., 2012](#)).

In this dissertation, I discuss two related topics in the evolution of binary star systems. Firstly, the emission of Gravitational Waves and the subsequent coalescence of compact binary systems. Secondly, the evolution of stellar mass binaries involving Common Envelope Evolution.

1.1 GRAVITATIONAL WAVES

Gravitational waves (GW) are ripples in space-time caused by some of the most violent and energetic processes in the universe. GWs provide new means to observe the universe. While we look at the universe through electromagnetic (EM) waves, we "listen" to the universe through GWs. In 1916 in his general theory of relativity, Albert Einstein predicted the existence of GW ([Einstein, 1916](#)). The theory predicted that massive accelerating objects would perturb space-time in such a way that the waves of the perturbed space would radiate from the source. These ripples carry information about their origins. However, it took several years to collect observational evidence of GWs. Observations of

the Hulse-Taylor pulsar showed that the rate of decrease of the binary orbit of this system is in agreement with the predicted rate through GW emissions ([Hulse & Taylor, 1975](#); [Weisberg & Taylor, 2005](#)). The 1993 Nobel Prize in Physics was awarded to Hulse and Taylor for this discovery.

It took almost 100 years after Einstein's prediction to make a direct observation of GW. In 2015, the detection of GW (GW150914) from a binary black hole (BBH) merger by Advanced Laser Interferometric Gravitational Wave Observatory (aLIGO) has opened a new observational window to our universe ([Abbott et al., 2016b](#)). The basic principle of gravitational wave detectors is the detection of tiny distortions in spacetime caused by passing gravitational waves using highly sensitive instruments capable of measuring minuscule changes in distance or geometry. The first attempt to make a direct measurement of GW is by using a resonant mass detector ([Weber, 1960](#)). However, the sensitivity of these detectors was not enough to capture the GWs from any astrophysical sources. The idea of using interferometry to detect GWs proposed in 1971¹ eventually led to the construction of the Laser Interferometer Gravitational-wave Observatory (LIGO)². The Nobel Prize in Physics for the year 2017 was granted to Rainer Weiss, Kip Thorne, and Barry Barish in recognition of their pivotal roles in conceiving and establishing LIGO and their significant contributions to the detection of GWs.

In addition to the aLIGO ([Aasi et al., 2015](#)) there are multiple ground-based interferometric detectors around the globe participating in GW detection efforts (Advanced Virgo ([Acernese et al., 2015](#)), KAGRA ([Akutsu et al., 2021](#)), TAMA ([Takahashi & TAMA Collaboration, 2004](#)), GEO600 ([Lück et al., 2006](#))). Three observational campaigns of Advanced LIGO and Advanced Virgo have been successfully concluded. The initial observing period, designated as O1, spanned from September 12, 2015, to January 19, 2016, exclusively

¹<https://dcc.ligo.org/LIGO-M890001/public>

²<https://dcc.ligo.org/LIGO-P720002/public>

utilizing Advanced LIGO. Subsequently, Advanced LIGO embarked on its second observational phase, O2, commencing on November 30, 2016, and concluding on August 25, 2017. Advanced Virgo formally joined O2 on August 1, 2017, and participated in O2 until August 25, 2017, thereby providing the first time three detectors (two aLIGO detectors and an Advanced VIRGO detector) were used to search for gravitational waves. The third observing run, O3, started on April 1, 2019, and ended on March 27, 2020. The current observing run O4 started on May 24, 2023, has completed its first half (O4a) with aLIGO detectors, and the second half (O4b) started on April 2024 with aLIGO and VIRGO. KAGRA is expected to join O4b in December 2024. There are multiple notable GW detections over these observational campaigns.

1.1.1 GW150914: First Detection of GW

As noted earlier, GW150914 is the first direct detection of GW ([Abbott et al., 2016b](#)). This was detected during O1 on September 14, 2015, with aLIGO detectors. With detailed parameter estimation of the source, this signal was attributed to the coalescence of two black holes (BH). The detection itself carried a great scientific significance as the first-ever direct measurement of GW and thereby confirming the existence of binary black hole. Additionally it also showed that the stellar mass BH can merge within the Hubble time to be detectable with GWs and laid down the foundation of the future of gravitational wave astronomy. O1 had one more BBH detection identified as GW151226 ([Abbott et al., 2016a](#))

1.1.2 GW170817 and GRB170817A: Multi-Messenger Astronomy

Compact binary systems containing neutron stars (NS) are particularly significant due to their potential emission in the electromagnetic spectrum post-merger. The detection

of gravitational waves resulting from the merger of a binary neutron star (BNS) system offers various additional possibilities compared to observing a BBH system. NS consists of matter, and therefore, during a BNS merger, electromagnetic radiation is expected to be emitted. It has been suggested in theory that BNS mergers could serve as a potential source for short gamma-ray bursts (sGRB) (Lattimer & Schramm, 1974). During a binary merger, BHs effectively act as point particles, while NS undergo tidal distortion as they approach each other. The tidal gravitational field induces mass quadrupole moments in the NS, leading to an accelerated coalescence rate of the binary system (Damour et al., 1992; Flanagan & Hinderer, 2008; Li & Paczynski, 1998; Tanaka & Hotokezaka, 2013). This effect can be calculated and incorporated into the waveform, suggesting the potential to extract information about the nuclear equation of state from the observation of GWs resulting from a BNS merger (Chatziioannou, 2020; Damour et al., 2012; Vines et al., 2011; Read et al., 2013). Although a BNS merger could result in the formation of a BH, there is a chance that some of the matter involved in the collision could be expelled, potentially becoming observable as kilonova (Li & Paczynski, 1998). During this process, rapid neutron capture would occur, leading to the formation of heavy elements such as gold and platinum (Lattimer & Schramm, 1974; Metzger, 2020). Additionally, by combining GW detector data, which provides the luminosity distance of the source, with electromagnetic observations of neutron star mergers, cosmological implications arise. Specifically, such observations enable the determination of the redshift of the merger event, which, when paired with the luminosity distance estimate, offers an independent measurement of the Hubble constant (Nissanke et al., 2010; Schutz, 1986).

The second observing run (O2) of aLIGO and VIRGO made the first detection of GW signal from the inspiral of two low-mass compact objects consistent with a BNS merger GW170817 (Abbott et al., 2017c). This was followed by the detection of an sGRB identi-

fied as GRB170817A (Abbott et al., 2017b) independently by the Fermi Gamma-ray Burst Monitor (Fermi-GBM) (Goldstein et al., 2017) and the INTErnational Gamma-ray Astrophysics Laboratory (INTEGRAL) (Savchenko et al., 2017). This was the first GW event observed with an electromagnetic counterpart, thereby marking a significant breakthrough for multi-messenger astronomy. Subsequent follow-up of this event resulted in the detection of kilonova (Coulter et al., 2017). This signal was also detected across the electromagnetic spectrum (Abbott et al., 2017d). This provided the means to study numerous important astrophysical and fundamental physics effects and became the foundation of multi-messenger astronomy.

Combining O1 and O2, there are 11 reported CBC events in the first Gravitational-Wave Transient Catalog (GWTC-1) (Abbott et al., 2021a).

1.1.3 Third Observing Run

The third observing run (O3) also has some notable CBC detections. The event GW190814 involves very asymmetric masses, with uncertainty surrounding the nature of the lighter component. It could either be the lightest black hole (BH) or the heaviest neutron star (NS) ever detected (Abbott et al., 2020c). GW190521 is the CBC with the heaviest BH so far (Abbott et al., 2020b). The remnant of this merger ($m \sim 148M_{\odot}$) falls in the upper mass gap region produced by (pulsational) pair-instability supernova processes (Fraley, 1968). LIGO and Virgo have announced the detection of GW from another possible binary neutron star merger GW190425 (Abbott et al., 2020a). However, no electromagnetic counterpart was detected for this event. LIGO and Virgo also have reported possible neutron star black hole (NSBH) mergers in O3, GW200105, and GW200115 (Abbott et al., 2021c). Neither of these were followed by an electromagnetic counterpart.

After O3, LIGO-Virgo has a total of 90 CBC detections in three catalogs: GWTC-2

([Abbott et al., 2021b](#)), GWTC-2.1 ([Abbott et al., 2024](#)) and, GWTC-3 ([Abbott et al., 2023](#)).

1.1.4 In this Dissertation

The success of joint detection of GW and GRB (and the following kilonovae and emission across the electromagnetic spectrum) in O3 can be largely attributed to our ability to locate the source of GW accurately. This was possible with the parameter estimation pipeline designed to locate the source of a GW detection. With more and more events being detected in every observational campaign, it is important that we use the telescope resources and computational resources efficiently to follow up on any such future detections. For this purpose, before the start of the fourth observing run (O4) I (along with my collaborators) developed a rapid parameter estimation pipeline. The main purpose of this pipeline is to assist the electromagnetic follow-up of detected GW by classifying the source of detected GW into one of the astrophysical categories (BNS, NSBH, and BBH) to help the astronomers decide if the GW trigger is worth following up in the EM spectrum.

In Chapter 2, I outline the fundamental concepts of parameter estimation in GW data analysis, along with introducing the foundational principles of the rapid parameter estimation pipeline, which forms the groundwork for my work. Chapter 3 explains our work on the rapid parameter estimation pipeline and Chapter 4 explains our work on utilizing the rapid parameter estimation pipeline in O4 to assist multi-messenger astronomy.

1.2 COMMON ENVELOPE EVOLUTION

Common Envelope Evolution (CEE) is an important phase in the life of many binary star systems ([Paczynski, 1976](#)). The Common Envelope (CE) phase occurs when one component of a binary star system gets engulfed by the envelope of its companion. The envelope is gravitationally bound to both stars and exerts a drag force on the secondary, which can

be thought of as a separate core within the envelope of the primary. This drag force causes the two cores to begin an inspiral phase, during which the orbital energy and angular momentum are transferred to the envelope, causing it to heat up and expand. Ultimately, this could result in two outcomes: if the envelope is too tightly bound, the inspiral will continue until the two cores merge into a single star. Alternatively, if the envelope is ejected, a short-period close binary forms.

CE phase plays an important role in the formation and evolution of GW sources by bringing the stars close together to lead to a merger within the age of the universe (Bethe & Brown, 1998; de Mink & Mandel, 2016; Belczynski et al., 2020; Dominik et al., 2012, 2015; Rodriguez et al., 2016; Mapelli & Giacobbo, 2018; Vigna-Gómez et al., 2018). CE is also important for explaining other astrophysical phenomena such as X-ray binaries, Type 1a supernovae, cataclysmic variables, Gamma-ray Bursts, etc (Webbink, 1984; Kalogera & Webbink, 1998; Taam, 1996).

CEE presents a significant theoretical challenge due to its complexity. Once a binary enters a CE phase, if it leads to the ejection of the envelope, and/or the merger of the binary components is difficult to predict. Modeling efforts for the CE phase have primarily utilized two methodologies: hydrodynamic simulations and analytic prescriptions. While hydrodynamic simulations offer detailed insights into the fluid dynamics and intricate interactions within the envelope, their computational demands limit their applicability to a wide range of binary systems. The analytic prescriptions provide a simplified yet insightful approach that can be applied to a broader spectrum of binary configurations with relatively lower computational costs.

Hydrodynamic simulations, despite their utility, encounter notable constraints when it comes to modeling CEE. Their primary focus lies in capturing the initial phase of CEE, known as the plunge-in phase, wherein the envelope of one star rapidly engulfs its com-

panion and the orbit shrinks. This phase happens on a dynamical timescale. The subsequent stages of CEE involve a more gradual process, where the envelope heats up and expands due to the energy released during the inspiral. During these later stages, accurate modeling demands a consideration of complex physics such as the radiative and convective mechanisms of energy transfer that significantly influence the behavior of different layers of the envelope, and equations of state for these layers. Moreover, the pre-CEE phase, preceding the onset of envelope ejection, presents its own set of challenges for hydrodynamic simulations. This phase often involves complex dynamics, such as unstable mass transfer between the binary components or other structural instabilities. But most hydrodynamic simulations approximate these conditions by initiating the plunge-in phase artificially, this approach inherently oversimplifies the early CEE dynamics. Crucial factors like tidal effects and mass transfer, which can affect the binary's structure, are often ignored in these simplified setups. Furthermore, the computational demands associated with hydrodynamic simulations pose practical limitations as they involve different time scales and complex physics.

1.2.1 In this Dissertation

In the last decade, advances in computing and algorithms have made high-resolution, long-timescale simulations of CEE possible. Being able to simulate a CEE through its different phases within a reasonable computing time is extremely useful as it helps to unravel many relevant physics of CEE. One longstanding question about CEE is the time scale and the efficiency of envelope ejection. Once a binary enters a CE phase, when it leads to a merger and when it leads to an envelope ejection is still unclear to us from our theoretical understanding. Some three-dimensional numerical computations of CEE have found a wide variance in the ejection efficiency of the envelope. Motivated from

some recent works, I (along with my collaborators) study the time scale and efficiency of CEE as well as the evolution of the envelope with a long time scale simulation CEE using moving-mesh hydrodynamics code (MANGA).

In Chapter 5, I briefly review CEE, binary systems involving CEE, explaining the different phases involved, timescales and energy of each phases, observations attributed to CEE and state of the art hydrodynamic code used for simulating CEE. Chapter 6 describes my work on simulating long-term simulation to study the evolution of the envelope and the envelope ejection.

CHAPTER 2

Parameter Estimation with Gravitational Waves

On September 14, 2015, a new era of astronomy began with the first detection of GW from a merging BBH (GW150814,) by the Advanced LIGO detectors ([Abbott et al., 2016b](#)). During the subsequent observing runs, LIGO Detectors along with VIRGO detectors detected around 100 CBC events ([Abbott et al., 2021a,b, 2024, 2023](#)). The most notable detection among these is the first detection of a BNS merger, GW170817 ([Abbott et al., 2017c](#)). While the detection of these CBC signals from the GW detector data is important, equally important is a methodology to accurately and quickly estimate the parameters characterizing the physical waveform describing these signals. Particularly, the importance of a fast and accurate parameter estimation scheme is greatly displayed during the detection of GW170817. Following the detection of the GW170817, astronomers detected a sGRB (GRB170817A) with a time delay of 1.7s with respect to the merger of GW170817 ([Abbott et al., 2017b](#)). The location of the source of the GW signal was consistent with the location of the source of the sGRB. The localization of the source allowed to identify the host galaxy NGC 4993 leading to further observation from this merger which included emissions in X-ray, UV, optical, IR, and Radio wavelengths ([Abbott et al., 2017d](#)). The spectroscopic analysis and the time scales of each emission supported the hypothesis that GW170817A is indeed a result of the merger of BNS followed by the sGRB and a kilonova/macronova powered by the radioactive decay of r-process nuclei synthesized in the ejecta ([Abbott et al., 2017d](#)). Additionally, this detection led to further studies on the measurement of Hubble Constant ([Abbott et al., 2017a](#)) and the estimation of the speed of gravity ([Abbott et al., 2017b](#)).

Considering the short time between the detection of GW and sGRB in the joint obser-

vation of GW170817 and GRB170817A, it becomes extremely important that we promptly conduct follow-up observations in the electromagnetic spectrum for future GW detections. Localization provides crucial guidance for subsequent observations, yet it is equally essential to assess the significance of pursuing an event in the electromagnetic spectrum. This is owing to the fact that not all compact binary coalescence events are anticipated to yield an electromagnetic counterpart. While localization tells us where to look during a follow-up, we also need to know if it is worth following up on an event in the electromagnetic spectrum. This is because not all CBC events are expected to produce an electromagnetic counterpart. Generally, BBH mergers are least expected to produce an EM counterpart while a binary system with a NS (like GW170817) has much higher chances of producing an electromagnetic counterpart. So, the information about the masses of the component stars and thereby the information on the type of star involved in the merger (a BH or a NS) is as important as the sky localization.

During the past three observing runs and the current fourth observing run of the ground-based GW detectors, multiple pipelines are used for parameter estimation all of which are based on Bayesian Inference. All these pipelines estimate the posterior distribution of the parameters characterizing the gravitational wave strain with varying latency and accuracy. The basic principle of each Bayesian Inference parameter estimation pipeline relies on the use of Bayes theorem to find the posterior probability distribution of each parameter which is achieved through some method of random sampling over the parameter space (For a detailed description of the basics of Bayesian Inference, see Section 2.3). Each pipeline has its significance and is designed to address a particular challenge in GW astronomy. For example, LALInference ([Veitch et al., 2015a](#); [LIGO Scientific Collaboration et al., 2018](#)) is a C-based library for Bayesian parameter estimation that is designed to produce accurate estimates for parameters defining the GW strain

data. Historically this was the primary tool that is being used for accurate parameter estimation by LIGO and VIRGO. Similarly, Bilby ([Ashton et al., 2019](#)), a Python-based library is a Bayesian parameter estimation pipeline aiming to provide more user-friendly tools than LALInference. Both these Bayesian pipelines are accurate but computationally expensive; calculations can take from hours to days to complete. The Bayesian sky localization pipeline known as BAYESTAR was developed to rapidly localize an event ([Singer & Price, 2016](#)). BAYESTAR can produce sky localization within minutes. This is achieved by fixing the values of the mass parameters to the values from the detection pipeline (or search pipeline) and computing the posterior distribution of the parameters that define the sky-localization. Since BAYESTAR reduces the number of unknown parameters in the calculation by relying on the estimates from the detection pipeline such as the mass parameters estimated by search pipelines, the time delay between the arrival time at each detector in the detector network, and the amplitude and phase on arrival, the estimation is fast. However, the accuracy can be affected by any bias in the estimates from the search pipeline. Nevertheless, this trade-off is acceptable given BAYESTAR's objective of delivering swift and approximate sky-localization.

To ensure effective and efficient electromagnetic follow-up, in addition to the swift sky-localization, we require a fast and reliable parameter estimation pipeline that can provide information on the component masses of the binary and compute the probability of having an NS component on that merger in a small time scale. Additionally, while the BAYESTAR skymap is quick and helpful for follow-up, a parameter estimation pipeline that can provide a better localization with slightly higher latency but with a latency less than other parameter estimation pipelines like LALInference or Bilby will be useful for continued follow-up. For this purpose, we have developed a parameter estimation pipeline that can produce reliable results in a time scale of minutes after the merger.

Chapter 3 discusses the details of this parameter estimation pipeline. In this chapter, I will lay down the fundamentals of Bayesian parameter estimation and the basics of the rapid parameter estimation pipeline that led the work in Chapter 3.

In this chapter, Section 2.3 describes the basic principles of using Bayesian Inference in GW parameter estimation problems. Section 2.4 describes the rapid parameter estimation pipeline that was designed to reduce computational time and cost. We have improved this method to overcome some of the limitations and developed a parameters estimation pipeline that is currently being used in the fourth observing run. Section 3 describes this improved algorithm.

2.1 GRAVITATIONAL WAVE UNDER LINEARIZED GRAVITY APPROXIMATION

Gravitational waves are perturbations in spacetime. Assuming that these perturbations are small, we can write the space-time metric ($g_{\mu\nu}$) as

$$g_{\mu\nu} = \eta_{\mu\nu} + h_{\mu\nu}, \quad (2.1)$$

where $\eta_{\mu\nu}$ is the flat spacetime metric and $h_{\mu\nu}$ is the perturbation in the flat space time. In a far-field zone, where the wavelength of the gravitational wave is much smaller than the distance between the source and the observer and the size of the source is much smaller than the wavelength of the gravitational wave, the time evolution of the metric perturbation can be written as (see [Creighton & Anderson \(2011\)](#) for detailed review)

$$h_{ij}^{TT}(t) = \frac{2G}{c^4 r} \ddot{I}^{ij}(t - r/c), \quad (2.2)$$

where G is the gravitational wave constant, c is the speed of light, r is the distance to the source. The quadrupole moment tensor (\ddot{I}) for the mass distribution ρ of the gravitational

wave source is given by is

$$I^{ij} = \int x^i x^j \rho(t, x) dx^3. \quad (2.3)$$

The gravitational wave flux which is the amount of gravitational wave energy dE passing through an area element dA of a sphere of radius r surrounding the gravitational wave source in a time dt can be written in terms of the quadrupole moment as

$$\frac{dE}{dAdt} = -\frac{G}{8\pi c^5 r^2} \langle \ddot{I}^{ij} \ddot{I}_{ij} \rangle. \quad (2.4)$$

Here $\langle \dots \rangle$ denotes an average over a spacetime region containing several GW oscillations or wavelengths.

Let's consider a binary system of two-point particles with masses m_1 and m_2 and in a circular orbit with separation between two masses a . Then for an observer at a distance r along its orbital angular momentum vector, the two polarizations of gravitational wave can be written as

$$h_+ = -\frac{4G\mu a^2 \omega^2}{c^4 r} \cos(2\phi), \quad (2.5)$$

$$h_\times = -\frac{4G\mu a^2 \omega^2}{c^4 r} \sin(2\phi). \quad (2.6)$$

Here μ is the reduced mass of the system given by $\mu = m_1 m_2 / (m_1 + m_2)$ and ω is the orbital angular momentum and $\phi = \omega t$ is the orbital phase.

For an observer not on the orbital axis but at an angle of inclination ι from the axis the gravitational waveform can be written as

$$h_+ = -\frac{2G\mu}{c^2 r} (1 + \cos^2 \iota) \left(\frac{v}{c}\right)^2 \cos(2\phi), \quad (2.7)$$

$$h_\times = -\frac{4G\mu}{c^2 r} \cos^2 \iota \left(\frac{v}{c}\right)^2 \sin(2\phi), \quad (2.8)$$

where $v = \sqrt{\frac{G(m_1+m_2)}{a}}$.

The gravitational wave luminosity of this system is given by

$$-\frac{dE}{dt} = L_{\text{GW}} = \frac{32}{5} \frac{c^5}{G} \eta^2 \left(\frac{v}{c}\right)^{10}, \quad (2.9)$$

where $\eta = \mu/(m_1 + m_2)$ is the symmetric mass ratio. The energy lost from the system comes from the orbital energy which is given by

$$E = -\frac{1}{2} \mu v^2, \quad (2.10)$$

Combining Equations 2.9 and 2.10 and integrating starting from an orbital velocity of $v_0 \ll c$ to the time until coalescence τ_c gives

$$\int_{v_0/c}^{\infty} \frac{d(v/c)}{(v/c)^9} = \frac{32\eta}{5} \frac{c^3}{GM} \int_0^{\tau_c} dt. \quad (2.11)$$

Solving for τ_c gives

$$\tau_c = \frac{5}{256\eta} \frac{GM}{c^3} \left(\frac{c^2 a_0}{GM}\right), \quad (2.12)$$

where a_0 is the orbital separation corresponding to v_0 .

Equating Equation 2.9 with a time derivative of Equation 2.10 and writing in terms of the gravitational wave frequency $f_{\text{GW}} = 2f = \omega\pi$ gives

$$\frac{f_{\text{GW}}}{dt} = \frac{96}{5} \pi^{8/3} \left(\frac{GM_c}{c^3}\right)^{5/3} f_{\text{GW}}^{11/3}, \quad (2.13)$$

where \mathcal{M}_c is called the chirp mass. The chirp mass is particularly important in the discussion on the gravitational waves from orbiting stars in Newtonian order because the chirp mass is the only combination of mass that defines the evolution of the frequency and

amplitude of the gravitational waves. We can see this when we rewrite the gravitational wave polarizations in the following way,

$$h_+(t) = \frac{GM}{rc^2} \frac{1 + \cos^2\iota}{2} \left(\frac{c^3(t_c - t)}{5GM} \right)^{-1/4} \cos \left[2\phi_c - 2 \left(\frac{c^3(t_c - t)}{5GM} \right)^{5/8} \right] \quad (2.14)$$

$$h_\times(t) = \frac{GM}{rc^2} \cos\iota \left(\frac{c^3(t_c - t)}{5GM} \right)^{-1/4} \sin \left[2\phi_c - 2 \left(\frac{c^3(t_c - t)}{5GM} \right)^{5/8} \right] \quad (2.15)$$

where t_c is the time of coalescence and ϕ_c is the phase at coalescence.

2.2 GRAVITATIONAL WAVE STRAIN AND DETECTOR DATA

In a network of detectors, the data (d_k) collected at each detector is a combination of the noise at that detector (n_k) and a possible gravitational wave strain (h_k),

$$d_k(t) = n_k(t) + h_k(t) \quad (2.16)$$

Note that while Section 2.1 gives a simplified description of the waveform for leading orders, in practice, we use a more detailed description with Post-Newtonian approximations (see [Creighton & Anderson \(2011\)](#) for a detailed description).

2.2.1 Intrinsic and Extrinsic Parameters

Based on physical nature we can group the parameters defining the gravitational wave strain from compact binaries into two categories: the intrinsic parameters ($\vec{\lambda}$) and the extrinsic parameters ($\vec{\theta}$). Combined, let's call the set of parameters $\vec{\mu} = \{\vec{\lambda}, \vec{\theta}\}$

The intrinsic parameters ($\vec{\lambda}$) are fundamental to the description of the binary. Typically this includes the masses and spins of the compact object component of a binary system. For a non-spinning binary system, the intrinsic parameters are the two-component

masses (m_1 and m_2) or any two parameters that are a combination of the component masses. Some such parameters are

$$\text{chirp mass : } \mathcal{M}_c = \frac{(m_1 m_2)^{3/5}}{(m_1 + m_2)^{1/5}} \quad (2.17)$$

$$\text{symmetric mass ratio : } \eta = \frac{m_1 + m_2}{(m_1 + m_2)^2} \quad (2.18)$$

$$\text{total mass : } M = m_1 + m_2 \quad (2.19)$$

$$\text{mass ratio : } q = m_2/m_1 \quad (2.20)$$

and chirptime parameters (in seconds)

$$\tau_0 = \frac{5}{256(\pi f_l)^{8/3}} \frac{f_l}{M^{5/3}\eta} \quad (2.21)$$

$$\tau_3 = \frac{\pi}{8(\pi f_l)^{5/3}} \frac{f_l}{M^{2/3}\eta} \quad (2.22)$$

where f_l is the lower cut-off frequency of the signal.

If the component stars are spinning, $\vec{\lambda}$ will include one to three spin parameters from each component of the binary system. We also use some combination of masses and spins as intrinsic parameters. Additionally, parameters defining precession and tidal deformation can be added to the set of intrinsic parameters.

The Extrinsic parameter describes the relative position and orientation of the binary in space and time with respect to the detectors. These are

$$\vec{\theta} = \{\alpha, \delta, \iota, D, \psi, \phi_c, t_{geo}\} \quad (2.23)$$

where α and δ are the right ascension and declination, ι is the inclination angle of the binary's angular momentum vector and the line of sight to Earth, D is the distance to

the binary, ψ is the polarization angle, and ϕ_c is the orbital phase of the binary at coalescence and t_{geo} is the time at which the coalescence point of the waveform arrives at the geocenter.

2.2.2 GW Strain at the detector

The gravitational wave strain measured by k^{th} interferometer in a detector network is given by

$$h_k(t) = F_{+,k}(\alpha, \delta, \psi, t_{geo})h_{+,k}(t) + F_{\times,k}(\alpha, \delta, \psi, t_{geo})h_{\times,k}(t), \quad (2.24)$$

where $F_{+,k}$ and $F_{\times,k}$ are the antenna pattern function of k^{th} detector and $h_{+,k}$ and $h_{\times,k}$ are the plus and cross-polarization of the gravitational wave strain evaluated at k^{th} detector (Refer Appendix A.1 of [Creighton & Anderson \(2011\)](#) for a detailed derivation of the antenna pattern functions.). When considering a network of detectors the antenna pattern function will depend on the relative orientation of a detector with respect to the Earth's fixed coordinate. Note that, because of the Earth's rotation, the antenna patterns change as a function of time. Considering the short duration of the signal detected by the detector and the Earth's rotational velocity, the change in antenna pattern as a function of time can be neglected. However, as instruments become more sensitive to longer binary coalescence waveforms, it will become necessary to account for this.

2.3 BAYESIAN INFERENCE IN PARAMETER ESTIMATION

Bayesian Inference is a very effective tool widely used in Gravitational Wave Astronomy data analysis including signal detection and parameter estimation.

In this section, I will limit the discussion to a single detector data. This formalism can be easily extended to multiple detectors. For a single detector, the data collected

at the detector ($d(t)$) is a combination of the noise at that detector ($n(t)$) and a possible gravitational wave signal ($h(t)$),

$$d(t) = n(t) + h(t). \quad (2.25)$$

Depending on whether the signal is present or not one can define two hypothesis

- Null Hypothesis (\mathcal{H}_0) when signal is not present : $d(t) = n(t)$
- Alternate Hypothesis (\mathcal{H}_1) when signal is present : $d(t) = n(t) + h(t)$

such that

$$p(\mathcal{H}_1|d) + p(\mathcal{H}_0|d) = 1, \quad (2.26)$$

where $p(\mathcal{H}_1|d)$ is the probability that the data contains signal and $p(\mathcal{H}_0|d)$ is the probability that the data is purely noise. We can write,

$$p(d) = p(d|\mathcal{H}_0)p(\mathcal{H}_0) + p(d|\mathcal{H}_1)p(\mathcal{H}_1), \quad (2.27)$$

where

$$p(d|\mathcal{H}_1) = \int p(d|\vec{\mu}, \mathcal{H}_1)\pi(\vec{\mu}, \mathcal{H}_1)d\vec{\mu}. \quad (2.28)$$

Here $\vec{\mu}$ represents the set of parameters defining the gravitational wave under the hypothesis \mathcal{H}_1 and $\pi(\vec{\mu}, \mathcal{H}_1)$ is the prior distribution of $\vec{\mu}$. It is useful to define

$$\pi(\vec{\mu}|\mathcal{H}_1) = \frac{\pi(\vec{\mu}, \mathcal{H}_1)}{p(\mathcal{H}_1)} \quad (2.29)$$

Using Bayes theorem, the probability of the data containing gravitational wave signal

with parameters $\vec{\mu}$ under the hypothesis \mathcal{H}_1 can be written as

$$p(\vec{\mu}, \mathcal{H}_1|d) = \frac{p(d|\vec{\mu}, \mathcal{H}_1)\pi(\vec{\mu}, \mathcal{H}_1)}{p(d)}. \quad (2.30)$$

Rewriting Equation 2.30 by substituting Equations 2.27, 2.28 and 2.29 gives

$$p(\vec{\mu}, \mathcal{H}_1|d) = \frac{p(d|\vec{\mu}, \mathcal{H}_1)\pi(\vec{\mu}|\mathcal{H}_1)p(\mathcal{H}_1)}{p(d|\mathcal{H}_0)p(\mathcal{H}_0) + p(\mathcal{H}_1) \int p(d|\vec{\mu}, \mathcal{H}_1)\pi(\vec{\mu}, \mathcal{H}_1)d\vec{\mu}}. \quad (2.31)$$

Defining likelihood Ratio ($\mathcal{L}(\vec{\mu}, d)$) as,

$$\mathcal{L}(\vec{\mu}, d) = \frac{p(d|\vec{\mu}, \mathcal{H}_1)}{p(d|\mathcal{H}_0)} \quad (2.32)$$

and, the evidence ratio (\mathcal{Z}) as

$$\mathcal{Z} = \int \mathcal{L}(\vec{\mu}, d)\pi(\vec{\mu}, \mathcal{H}_1)d\vec{\mu} \equiv \frac{p(d|\mathcal{H}_1)}{p(d|\mathcal{H}_0)}. \quad (2.33)$$

Expressing posterior in terms of the evidence ratio and the likelihood ratio,

$$p(\vec{\mu}, \mathcal{H}_1|d) = \frac{\mathcal{L}(\vec{\mu}, d)\pi(\vec{\mu}|\mathcal{H}_1)}{\mathcal{Z} + \frac{p(\mathcal{H}_0)}{p(\mathcal{H}_1)}}. \quad (2.34)$$

The likelihood ratio is the only term that carries both the data and the signal parameters. Generally, the functional form of the likelihood ratio is such that the posterior will be maximized at the most accurate values for the set of parameters $\vec{\mu}$.

To estimate the posterior distribution of the parameters, we need to estimate different components of Equation 2.34 by randomly sampling the parameter space. Estimating the likelihood ratio involves computing the waveform at each sample and computing the inner product of this waveform with the detector data (see Section 2.3.1). This is a

computationally expensive process and the major cost of Bayesian-based parameter estimation. There are different sampling methods to make the sampling efficient. For example, LALInference uses parallel tempering Markov Chain Monte Carlo (MCMC) scheme (Gilks et al., 1998) and nested sampling (Skilling, 2012). Bilby has a choice of MCMC samplers (emcee (Foreman-Mackey et al., 2013), ptmcee (Vousden et al., 2016) and, PyMC3 (Salvatier et al., 2015)) and various version of nested samplers (dynesty (Speagle, 2020), Nestle (Nestle, 2014), CPNest (Veitch et al., 2022), etc.)

2.3.1 Likelihood Ratio

Under the Null Hypothesis and under the assumption that the noise at each detector is Gaussian, the noise at each detector is characterized by the power spectral density function $S(f)$ given by

$$\langle \tilde{n}(f)\tilde{n}^*(f') \rangle = \frac{1}{2}S(|f|)\delta(f - f'). \quad (2.35)$$

In this discussion, we define noise-weighted inner product $\langle a|b \rangle$ as

$$\langle a|b \rangle_k = 2 \int_{-\infty}^{\infty} df \frac{\tilde{a}^*(f)\tilde{b}(f)}{S_k(f)}. \quad (2.36)$$

Under the Gaussian noise assumption, we can write

$$p(d|\mathcal{H}_0) \propto e^{-\langle d|d \rangle/2}, \quad (2.37)$$

$$p(d|\vec{\mu}, \mathcal{H}_1) \propto e^{-\langle d-h(\vec{\mu})|d-h(\vec{\mu}) \rangle/2} \quad (2.38)$$

Then we can write the likelihood ratio as,

$$\mathcal{L}(\vec{\mu}|d) = \frac{e^{-\frac{1}{2}\langle d-h(\vec{\mu})|d-h(\vec{\mu}) \rangle}}{e^{-\frac{1}{2}\langle d|d \rangle}}. \quad (2.39)$$

For a network of detectors,

$$\mathcal{L}(\vec{\mu}, d) = \prod_k \frac{e^{-\frac{1}{2}\langle d-h(\vec{\mu})|d-h(\vec{\mu})\rangle_k}}{e^{-\frac{1}{2}\langle d|d\rangle_k}}. \quad (2.40)$$

2.4 RAPID PARAMETER ESTIMATION

[Pankow et al. \(2015\)](#) introduced a Bayesian-based architecture for rapid parameter estimation (RapidPE from hereafter) of gravitational wave sources. Unlike other parameter estimation pipelines discussed earlier, RapidPE is designed to provide quick and reliable parameter estimation in a timescale of minutes to assist low-latency electromagnetic follow-ups. They achieved this by efficient evaluation of the likelihood, highly-parallelized Monte Carlo integration, and using input derived from gravitational-wave search and sky localization pipelines to limit the parameter space.

As I have described earlier, the computational cost of likelihood evaluation has been the limiting step of gravitational wave parameter estimation. Multiple factors contribute to this cost. The first is the cost of generating the waveform for each sample that the algorithm draws during the sampling process. Depending on the mass of the system the length of signal that needs to be generated changes. While a typical black hole binary spends a second in the frequency band of LIGO detectors, the binary neutron star could spend minutes. For example, the GW170817 spends $\sim 100s$ ([Abbott et al., 2017c](#)) in the LIGO frequency band.

This means that for binary neutron star events which need a quick parameter estimation result for effective electromagnetic follow-up, the length of the signal adds to the cost and time of likelihood estimation.

RapidPE reduces the cost of likelihood evaluation in three steps. First, it separates the intrinsic and extrinsic parameters in the likelihood so that the extrinsic parameters enter

the equation only as a coefficient to the expensive gravitational wave strain term which depends only on the intrinsic parameters (Section 2.4.1 and 2.4.2). Second, limiting the intrinsic sample to a grid so that the waveform calculation only needs to be performed on this grid point and that can be used by scaling with the appropriate coefficient based on the random samples for the extrinsic parameters (Section 2.4.3). Third, since the samples of intrinsic parameters are in a grid and the extrinsic sampling is performed on each of these grid points, the whole calculation can be parallelized to each grid point. So the overall time of completing the calculation is equivalent to the time taken to compute the likelihood at a single grid point (Section 2.4.4). For a detailed description these, see [Pankow et al. \(2015\)](#).

2.4.1 Waveform Decomposition

Let's first modify the time of arrival t_{geo} in the extrinsic parameters to account for the time difference between each detector in a network of detector. Define the time of arrival of the coalescence at each detector as

$$t_k = t_{\text{geo}} - \frac{\vec{x}_k(t_{\text{geo}}) \cdot \hat{N}(\alpha, \delta)}{c}, \quad (2.41)$$

where \vec{x}_k is a vector pointing from the geo-center to the k^{th} detector and $\hat{N}(\alpha, \delta)$ is the direction of gravitational wave propagation. So, each detector in the network of the detector will have an offset relative to the geo-center time depending only on the sky location.

Writing the complex valued strain at each detector in terms of the spin-2-weighted spherical harmonics as

$$h_{+,k}(t) - ih_{\times,k}(t) = \frac{D_{\text{ref}}}{D} \sum_{lm} Y_{lm}^{(-2)}(\iota, -\phi_c) \hat{h}_{lm}(\mathcal{M}_c, \eta, t_k; t) \quad (2.42)$$

evaluated at some fixed distance D_{ref} . If we define a complex-valued antenna pattern function at each detector as

$$F_k = F_{+,k} + iF_{\times,k}, \quad (2.43)$$

then we can express the strain at the k^{th} detector as

$$h_k(\vec{\lambda}, \vec{\theta}; t) = \text{Re} \frac{D_{\text{ref}}}{D} F_k(\alpha, \delta, \psi, t_{\text{geo}}) \sum_{lm} Y_{lm}^{(-2)}(\iota, -\phi_c) \hat{h}_{lm}(\mathcal{M}_c, \eta, t_k; t). \quad (2.44)$$

Note that in Equation 2.44, aside from t_k we now have separated all intrinsic parameters into \hat{h}_{lm} terms and the extrinsic parameters into F_k and $Y_{lm}^{(-2)}$.

Now let's write the gravitational wave strain in the frequency domain via a Fourier Transform

$$\tilde{h}(f) = \int_{-\infty}^{\infty} h(t) e^{-2\pi i f t} dt. \quad (2.45)$$

If $\tilde{h}(t_k; f)$ is the frequency domain representation of the gravitational wave strain at some arrival time t_k , then the same strain at a different arrival time t'_k can be represented as

$$\tilde{h}(t'_k; f) = \tilde{h}(t_k; f) e^{-2\pi i f (t'_k - t_k)}. \quad (2.46)$$

If we work with frequency domain waveform, arrival time t_k can be factored out as $e^{-2\pi i f t_k}$ thus completing the separation of intrinsic and extrinsic parameters into different terms.

In this decomposition above, I have only considered the mass parameters as intrinsic parameters. But in general, the intrinsic parameters can include any other parameters that come from any other physical properties of the binaries such as spin, precession, and tidal effect. There will always be seven extrinsic parameters that enter the gravitational wave strain equation through the inexpensive geometric terms and all intrinsic parame-

ters through the expensive h_{lm} terms.

2.4.2 Likelihood

Now we can separate the likelihood ratio (Equation 2.40) into intrinsic and extrinsic terms by utilizing the decomposition explained in Section 2.4.1. To do this, let's define the following quantities

$$Q_{lm}(\vec{\lambda}, t_k) \equiv \langle h_{lm}(\lambda, t_k) | d \rangle_k = 2 \int_{-\infty}^{\infty} \frac{e^{2\pi i f t_k} \tilde{h}_{lm}^*(\vec{\lambda}; f) \tilde{d}(f)}{S_k(|f|)} df, \quad (2.47)$$

$$U_{k,lm,l'm'} \equiv \langle h_{lm} | h_{l'm'} \rangle_k, \quad (2.48)$$

$$V_{k,lm,l'm'} \equiv \langle h_{lm}^* | h_{l'm'} \rangle_k. \quad (2.49)$$

Plugging these into Equation 2.40

$$\begin{aligned} \ln \mathcal{L}(\vec{\lambda}, \vec{\theta}) &= \frac{D_{\text{ref}}}{D} \text{Re} \sum_k \sum_{lm} (F_k Y^{(-2)lm})^* Q_{k,lm}(\vec{\lambda}, t_k) + \\ &- \frac{D_{\text{ref}}^2}{4D^2} \sum_k \sum_{lm'l'm'} \left[|F_k|^2 [Y_{lm}^{(-2)}]^* Y_{l'm'}^{(-2)} U_{k,lm,l'm'}(\vec{\lambda}) + \text{Re}(F_k^2 Y^{(-2)lm} Y_{l'm'}^{-2} V_{k,lm,l'm'}(\vec{\lambda})) \right]. \end{aligned} \quad (2.50)$$

Note that the intrinsic parameters enter this equation through $Q_{k,lm}$, $U_{k,lm,l'm'}$ and $V_{k,lm,l'm'}$ terms which are computationally expensive as it involves computing different modes of the waveform h_{lm} , the inner products of these and the Fourier Transforms. By contrast, the extrinsic parameters enter the equation through F_k and $Y_{lm}^{(-2)}$ which are much cheaper to compute.

2.4.3 Intrinsic Grid

In [Pankow et al. \(2015\)](#), the intrinsic parameters are fixed to a grid and the extrinsic parameters are marginalized using Monte Carlo integration. To identify the region in the intrinsic space to lay down the intrinsic grid, RapidPE uses the intrinsic parameter identified by the search pipelines. Let's call this "search identified point" hereafter. Then RapidPE identifies a constant overlap region based on some predetermined overlap threshold using Fisher Matrix calculations. This involves calculating the overlap between the search identified point $\vec{\lambda}_i$ and the points in the search pipeline's template bank $\vec{\lambda}_j$,

$$\mathcal{O}_{ij} = \frac{|\langle h(\vec{\lambda}_i) | h(\vec{\lambda}_j) \rangle|}{\sqrt{\langle h(\vec{\lambda}_i) | h(\vec{\lambda}_i) \rangle \langle h(\vec{\lambda}_j) | h(\vec{\lambda}_j) \rangle}}. \quad (2.51)$$

The grid placed based on the Fisher Matrix scheme will have points along a radial spike centered at the search-identified point. See Figure 1 in [Pankow et al. \(2015\)](#).

2.4.4 Extrinsic Sampling

As noted above, RapidPE used a Monte Carlo Sampling to sample over extrinsic parameters for each intrinsic grid point in the intrinsic grid. This gives likelihood evaluated at each grid point as a function of the extrinsic parameters ($\mathcal{L}(\vec{\lambda}_i, \vec{\theta})$ for each intrinsic grid point i). RapidPE marginalizes over the extrinsic parameters using Monte Carlo integration to get the reduced likelihood which is defined as

$$\mathcal{L}_{\text{red}}(\vec{\lambda}_i) = \int \mathcal{L}(\vec{\lambda}_i, \vec{\theta}) p(\vec{\theta}) d\vec{\theta}, \quad (2.52)$$

where $p(\vec{\theta})$ is the prior over the extrinsic parameters. In practice, when we numerically evaluate this integral the sampling function used for sampling the extrinsic parameters

$(p_s(\vec{\theta}))$ modifies this equation as,

$$\mathcal{L}_{\text{red}}(\vec{\lambda}_i) = \int \frac{\mathcal{L}(\vec{\lambda}_i, \vec{\theta})p(\vec{\theta})}{p_s(\vec{\theta})} [p_s(\vec{\theta})d\vec{\theta}]. \quad (2.53)$$

If we draw N samples for i th intrinsic grid point, then for the q th extrinsic samples, we can define a weight for each sample as

$$w_q = \frac{\mathcal{L}(\vec{\lambda}_i, \vec{\theta}_q)p(\vec{\theta}_q)}{p_s(\vec{\theta}_q)}. \quad (2.54)$$

Then the reduced likelihood is equivalent to

$$\mathcal{L}_{\text{red}}(\vec{\lambda}_i) \equiv \frac{1}{N} \sum_q w_q. \quad (2.55)$$

To decide how many samples (N) are needed to efficiently compute $\mathcal{L}_{\text{red}}(\vec{\lambda}_i)$, at a regular interval (say after every n_{chunk} of samples) RapidPE calculates the ‘effective number of samples’ defined as

$$n_{\text{eff}} \equiv \frac{\sum_q w_q}{\max\{w_q\}}. \quad (2.56)$$

Here n_{eff} measures how many independent samples produce similar weights near the highest likelihood sample (largest observed weight). In the implementation, RapidPE pre-defines the maximum number of samples n_{max} and the expected $n_{\text{eff}}^{\text{exp}}$, and the sampling is stopped if the current estimated n_{eff} reached the expected $n_{\text{eff}}^{\text{exp}}$ or the current numbers of samples N reaches n_{max} .

2.5 LIMITATION OF FISCHER MATRIX SCHEME OF RAPIDPE

RapidPE scheme uses information from the gravitational wave search pipelines to determine the intrinsic grid region. From the search-identified point, the scheme then identifies a region in the intrinsic parameter space based on overlap calculation (Equation 2.51) between the search-identified point and the templates in the template bank of the search pipeline. This region was constructed in the shape of an ellipsoid which corresponds to a constant overlap surface. The intrinsic grid points placed in this region are placed along radial lines centered at the search-identified point. There are some limitations to this method. First, If there is some bias in the search-identified point, then the intrinsic grid points placed will also be biased. Since the intrinsic grid points are centered around the search-identified points and are elliptical in shape, the grid might fail to cover the region of highest posterior support if the search pipeline estimate has significant bias. Secondly, once the intrinsic grid is placed and the likelihood is calculated, there is no algorithm to refine or add more intrinsic grid points to get a denser estimate of likelihood. Lastly, this grid placement algorithm gets complicated to expand to more intrinsic parameters like component spin. To overcome these, I (and my collaborators) developed a new way of grid placement called Adaptive Mesh Refinement ([Rose et al., 2022](#)) which I will discuss in detail in Chapter 3.

CHAPTER 3

Adaptive Mesh Refinement in RapidPE

This chapter is reproduced in part from [Rose et al. \(2022\)](#), which is being prepared for publication under the title "Supplementing rapid Bayesian parameter estimation schemes with adaptive grids". A preprint version of this work can be found at <https://arxiv.org/abs/2201.05263>

To overcome the issues discussed in the earlier chapter, we introduced an alternate grid placement algorithm for RapidPE called Adaptive Mesh Refinement (AMR) in [Rose et al. \(2022\)](#) (AMR RapidPE hereafter). In this version of grid placement, we continue to use the search estimated intrinsic point to identify the region in the intrinsic space within which we expect to identify the peak of the posterior. However, instead of the elliptical-shaped radial arrangement of grid points, we employ a more flexible rectilinear grid with a scheme to place more grid points in the region of most posterior support for computational efficiency. The AMR version of RapidPE continues to use the waveform decomposition (Section 2.4.1) and the posterior and likelihood formalism (Section 2.4.2) and the highly parallelized computations. With the improvement in the intrinsic grid, we show that the AMR RapidPE can overcome search biases.

The AMR grid method presented in this chapter used the overlap calculation to determine the initial region. Note that in the O4, the AMR grid placement is not based on overlap but based on the estimated biases from the search pipeline. This method determining the initial region based on the search bias is presented in [Rose \(2024\)](#).

3.1 INITIAL REGION IDENTIFICATION AND GRID PLACEMENT ALGORITHM

In AMR RapidPE, we continue using the overlap calculation between the template bank and search identified points to decide the initial region to place the intrinsic grid point (Equation 2.51). However, instead of placing the grid in an elliptical shape, we use a simplified rectilinear grid structure. At each point of this rectilinear initial grid, we can employ adaptive mesh refinement to place additional grid points in regions where the posterior has the most support, thus mapping out the posterior more efficiently.

For efficient identification of the initial region for grid placement, we pre-compute the overlap. The overlap of every template in the template bank is calculated with every other template and stored as an overlap bank using Equation 2.51. Using this overlap bank, we identify all templates within the template bank which has an overlap with the search-identified value above a threshold. Based on this, a rectilinear region in the intrinsic space is identified to contain all these selected templates.

Once the region is identified, the grid placement scheme can be applied. The grid can be constructed in any parameter in intrinsic space. Then we place a grid of $N_p \times N_p$ points along the coordinate axis of selected intrinsic parameters. To better capture the shape of the posterior support with efficient computations, we recalculate the overlap over the initial grid and deactivate all grid points which do not meet the overlap threshold criteria used to create the preliminary region. This process is called pruning.

A fixed grid will only capture the peak of the distribution to the resolution of the grid. The easiest solution to this problem is to increase N_p , the initial number of grid points on a side. While the pruning strategy above can avoid some wasted computations, the overall increase in the resolution will still increase the computational cost. Instead, we employ adaptive mesh refinement (Berger & Colella, 1989), which can concentrate points where the posterior has the most support and increase the number of effective samples (Equation

2.56) collected in the integration process. AMR is used heavily in numerical relativity and computational astrophysics (Dubey et al., 2014), where precise control over resolution is required to accurately represent the spacetime around singularities or efficiently represent quantities with complex dynamics and dynamic ranges. We face a similar situation where the peak of the posterior scales as $\exp(+\bar{\rho}^2)$ where $\bar{\rho}$ is the expected signal-to-noise ratio. Even small mismatches between templates on the grid and a template at the true signal parameters can cause a significant underestimate of the peak of the posterior.

We implement a simple mesh refinement scheme where a grid point is added at the midpoint between grid points and their diagonals as in Figure 3.1. While the sample refinement scheme in Figure 3.1 is refining around every grid point in one level to go to the next level of the grid, in practice the strategy is slightly different. Instead of refining around every grid point we choose a subset of grid points based on the likelihood or overlap calculation and refine only around that. I will describe this selection criteria later in this section. Once the grid points to be refined are selected, each selected grid point is considered to be at the center of a cell extending to the midpoint between the grid point neighbors, so the new subgrid points will lie along the edges and vertices of the cell. For example, in a 2×2 grid, refining a single grid point will add 8 points around that grid point. This procedure can be repeated as many times as needed or computationally feasible, potentially producing several subgrid evaluation levels.

There are two ways in which we select the grid points to be refined at any level of the intrinsic grid. One method is called ‘serial refinement’, where the grid refinement is based on the reduced likelihood (Section 2.4.4) calculated at each grid point. In this method, the reduced likelihood is calculated using Equation 2.52 for every grid point in a grid level. A threshold is set in the likelihood such that all grid points with a reduced likelihood value of 90% (for example) of the the maximum reduced likelihood is refined. The sec-

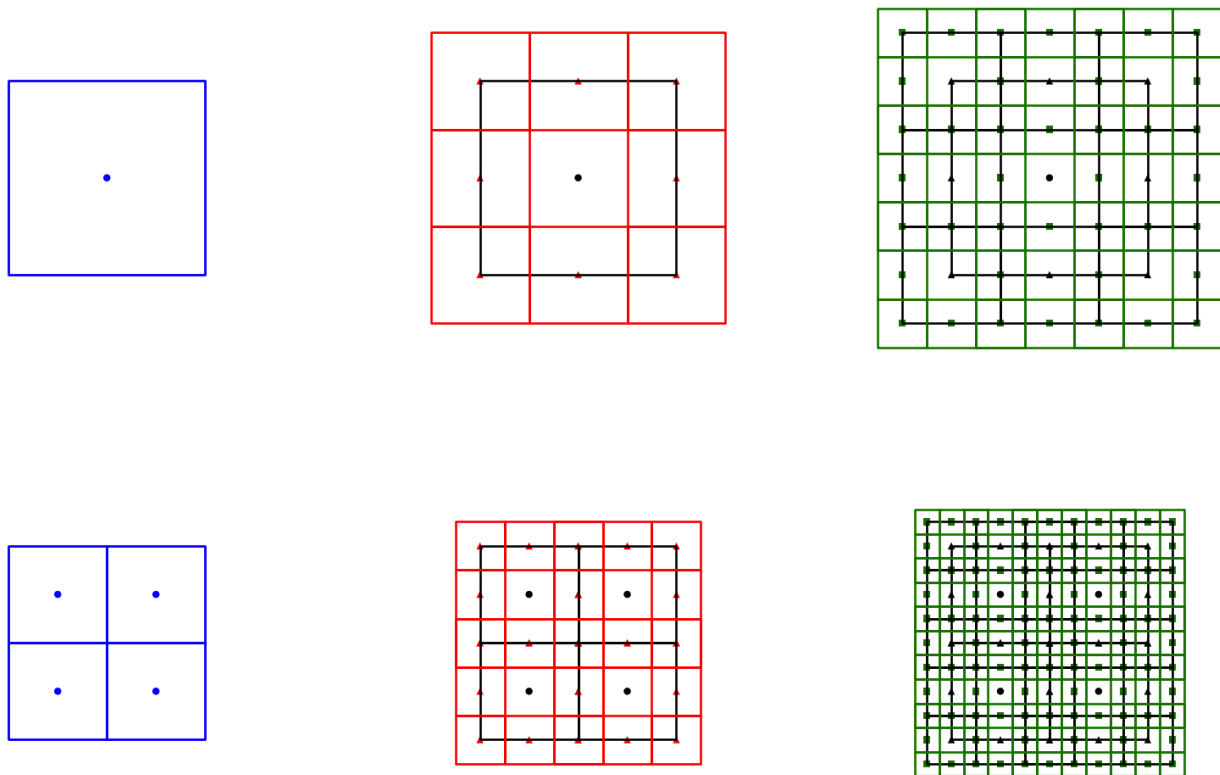


Figure 3.1: The top three panels represent a fiducial cell and inset grid point (blue), a single level of refinement (red), and a second level of refinement (green). The bottom three panels display the same procedure, but with a split initial region to highlight the interlocked but overlapping refined cells. In all cases, the black cells are the previous level underlaid for reference. Grid points that have already been evaluated (the center point, zero offset refined cell) are not included in the next refinement level.

ond refinement method is called ‘pre-refinement’, in which the grid refinement is based on the overlap calculated on the grid points before any reduced likelihood computations are done. In this case, a set of overlap thresholds is fixed in advance corresponding to various refinement levels. Subsequent levels are identified by recalculating the overlap with the search-identified point for each grid point, and those exceeding the predetermined overlap threshold are kept and used for the next level.

Note that we can implement this grid scheme in any number of intrinsic parameters such as masses and spins. However, for the rest of the discussion in this chapter, I will limit the grid to the mass space. So, for the following discussion, the intrinsic grid will be two-dimensional in mass space.

3.2 LIKELIHOOD INTERPOLATION

With reduced likelihood calculated at each each grid point the resolution of the likelihood is limited to the resolution of the grid. To construct a posterior for the intrinsic parameter we need a method to interpolate the reduced likelihood in the intrinsic space. We do this by assuming that the reduced likelihood in the intrinsic space is a sum of Gaussian functions centered at each grid point. Each Gaussian function has an amplitude equal to the reduced likelihood at that grid point and a standard deviation equal to the distance to the nearest grid point.

Let’s denote the mass parameter in which the 2D grid is rectilinear by m_a and m_b . Then reduced likelihood as a function of these parameters is given by

$$\mathcal{L}_{\text{red}}(m_a, m_b) \approx \sum_i \mathcal{L}_i \exp \left\{ \frac{-1}{2\sigma_{a,i}^2} [m_{a,i} - m_a]^2 + \frac{-1}{2\sigma_{b,i}^2} [m_{b,i} - m_b]^2 \right\} \quad (3.1)$$

where $m_{a,i}$ and $m_{b,i}$ are the the parameter of each grid point i and \mathcal{L}_i is the reduced like-

likelihood at that grid point. $\sigma_{a,i}$ and $\sigma_{b,i}$ are the standard deviations of the 2D Gaussian function at each grid point for the m_a coordinate and m_b coordinate respectively. Then the posterior can be constructed as

$$p(m_a, m_b|d) = \frac{\mathcal{L}_{\text{red}}(m_a, m_b)\pi(m_a, m_b)}{\mathcal{Z}} \quad (3.2)$$

3.3 TESTING ON SIMULATED GW EVENTS

The AMR grid scheme is tested on simulated GW events from the First Two Years mock data challenge (F2Y) (Singer et al., 2014; Berry et al., 2015). This dataset is used to simulate the performance of the LIGO-Virgo interferometer network in a realistic configuration during 2015 and 2016 using injected BNS signals with mild ($\chi = c|S|/Gm^2 \leq 0.05$ where $|S|$ is the spin angular momentum and m is the mass of each NS) and isotropic spins. For F2Y, all search pipelines used a non-spinning template bank and only provided estimates for the masses of the injections. So for testing AMR, we ignored spin. While, this can introduce some biases in the search estimated point, later in this section we show that it does not affect the posterior estimate from AMR RapidPE.

In practice, we can choose any coordinate in mass space to construct a rectilinear grid. We chose to place the intrinsic grid rectilinear in $\tau_0 - \tau_3$ space (Equation 2.21 and 2.22). This choice is made because the template banks used by search pipelines in F2Y is generated in $\tau_0 - \tau_3$ coordinates (Singer et al., 2014; Babak et al., 2013).

In the section below I compare the three intrinsic grid methods described earlier, here denoted as ‘Fisher’ for the Fisher matrix approximation scheme, ‘grid refine’ for the iterative refinement procedure using reduced likelihood calculations(‘serial refinement’), and ‘preremote’ for the single step refinement procedure using overlaps. In the section below I will discuss one simulated event which is identified by search ID = 14631 and search ID

= 10184 in the F2Y study.

3.3.1 Comparing different grid placement schemes

For the first example, we select an injection from the F2Y dataset with the search ID #10184, network SNR of 13.6, search-recovered masses of $m_1 = 1.39M_\odot$ and $m_2 = 1.28M_\odot$, injected masses of $m_1 = 1.43M_\odot$ and $m_2 = 1.24M_\odot$, and dimensionless angular momentum aligned spin $\chi_a = -0.009$ and in-plane spin $\chi_p = 0.030$. Figure 3.2 shows the value of the logarithm of the reduced likelihood after the Monte Carlo integration step has been completed for all three cases. The contour in this figure represents the 90% credible region obtained from `lalinference_mcmc`¹ (LIGO Scientific Collaboration et al., 2018). The high likelihood support in this region shows that all three methods perform reasonably well when search biases are negligible. We obtain intrinsic posterior samples from the AMR RapidPE grids by approximating the likelihood function as a sum of Gaussians centered at each grid point with standard deviations of half the spacing between adjacent grid points and weighted by the value of the extrinsic-marginalized likelihood calculated at each grid point. Figure 3.4 shows the posterior plots for event #10184, which are the histograms of the likelihood samples weighted by the mass priors.

The simulated event #14631 has a network SNR of 12.0, search recovered masses of $m_1 = 1.49M_\odot$ and $m_2 = 1.14M_\odot$, injected masses of $m_1 = 1.32M_\odot$ and $m_2 = 1.28M_\odot$, and injected $\chi_a = 0.006$ and $\chi_p = 0.032$. Figure 3.3, illustrates the performance of different grid placement algorithms for this event. Note that this event has a significant bias in its search-identified point. While the pre-refine and Fisher matrix schemes fail to place a grid point to contain the true injection, the grid refines scheme successfully contains the true injection within the initial region. To compare the grid placement to the posterior

¹<https://www.ligo.org/scientists/first2years/>

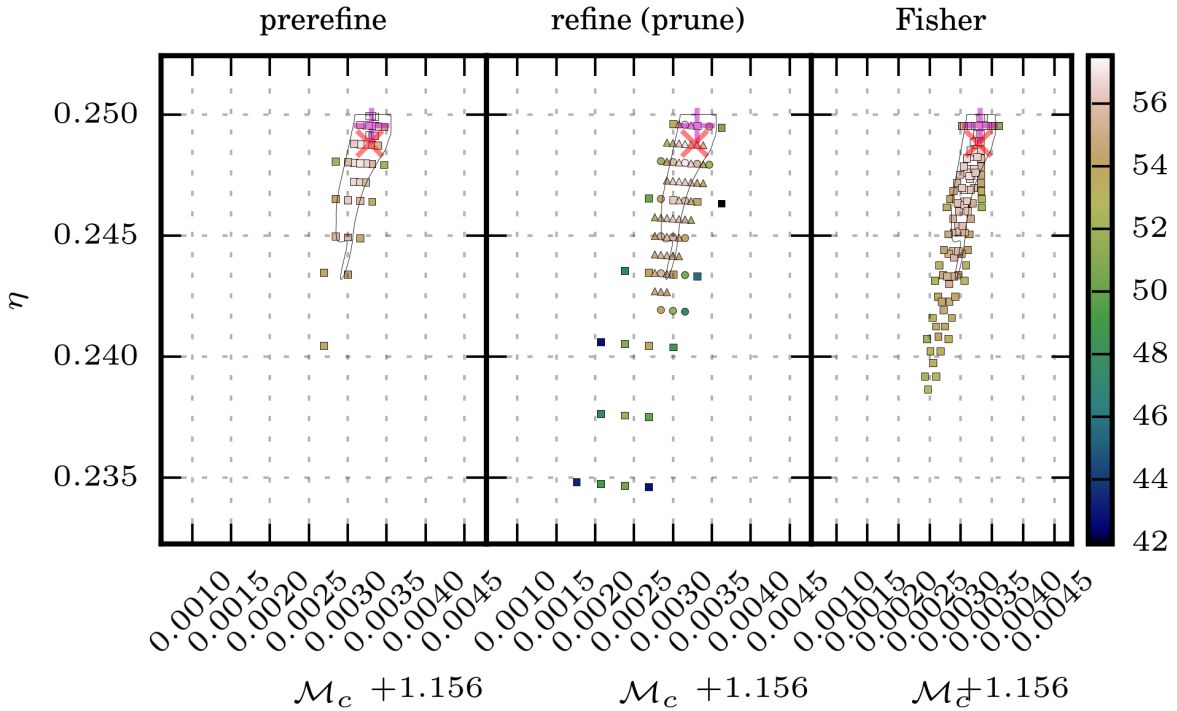


Figure 3.2: This figure shows the logarithm of the reduced likelihood obtained through marginalization scatter plotted against \mathcal{M}_c and η for event #10184. The left panel is the result of the prerrefinement method, the middle is the (pruned) serial grid refinement method, and the right is the Fisher matrix method. The magenta cross marks the search-identified point from which the intrinsic grid was computed, while the red x marks the injected parameters. In this figure, the contour represents the posterior obtained from `lalinference_mcmc`. The squares, circles, and triangles indicate the first, second, and third grid levels, respectively.

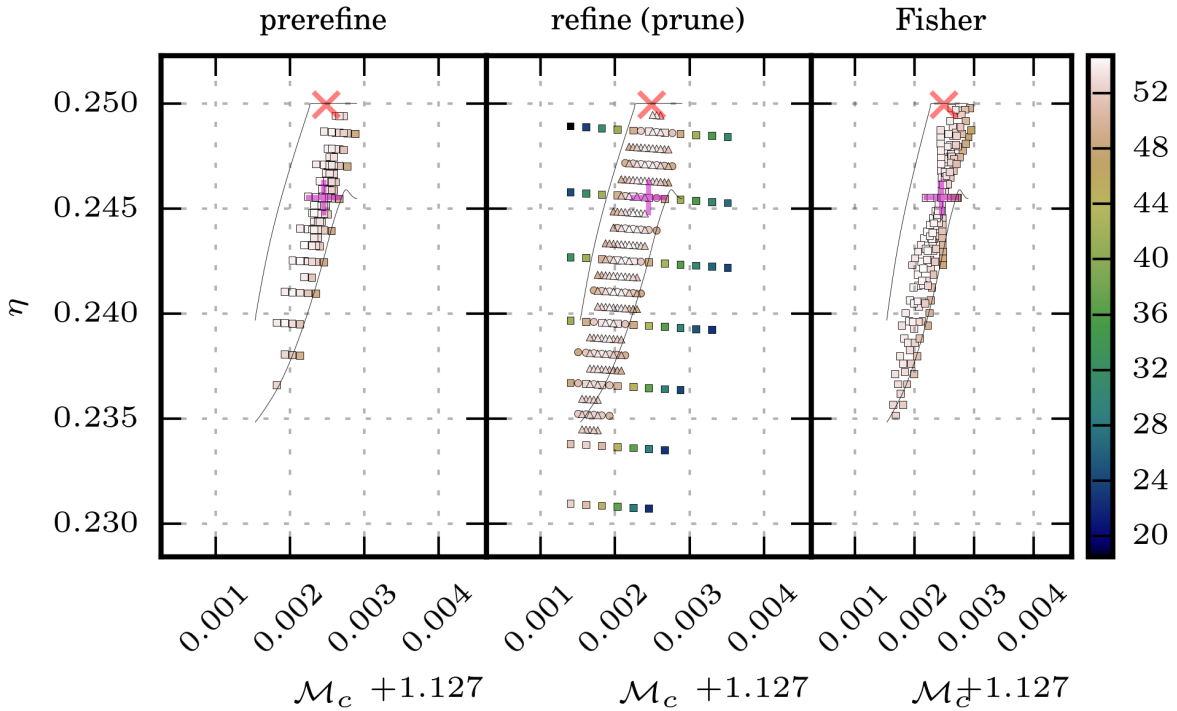


Figure 3.3: This figure shows the logarithm of the reduced likelihood obtained through marginalization scatter plotted against \mathcal{M}_c and η for event #14631. The left panel is the result of the prer refinement method, the middle is the (pruned) serial grid refinement method, and the right is the Fisher matrix method. The magenta cross marks the search-identified point from which the intrinsic grid was computed, while the red x marks the injected parameters. In this figure, the contour represents the posterior obtained from `lalinference_mcmc`. The squares, circles, and triangles indicate the first, second, and third grid levels, respectively.

from `lalinference_mcmc`, the contour in all three panels of this figure represents the 90% credible region from `lalinference_mcmc`. In Figure 3.5, we compare the posterior from the grid refine scheme to the posterior from `lalinference_mcmc`. Figure 3.3 and 3.5 illustrates how even when the initial RapidPE grid based on the search estimate completely misses the true injected intrinsic point, the adaptive grid refinement scheme of RapidPE compensates for search biases well enough to resolve the peak of the posterior, which is much closer to the peak in `lalinference_mcmc`.

3.3.2 Validation of AMR RapidPE

To test the validity of RapidPE, we ran it on 100 of the three-detector simulated signals from the F2Y mock data challenge injected into Gaussian noise (via `gstlal_fake_frames2`) following the mid PSD curve as in the 2016 study (Singer et al., 2014). The initial grids were generated rectilinear in \mathcal{M}_c and η with 5 points per side and an overlap of 0.3 with the injected masses. We used the serial refinement method with a total of three grid levels, including the initial grid. The likelihoods were evaluated using the TaylorF2 waveform (Buonanno et al., 2009) as in Section 2.4.2. We used the results of these runs to calculate the CDF of the posterior up to the injected parameter and check that the correct fraction of events is found within the given probability interval, or confidence interval (C.I.). For gravitational-wave parameter estimation codes, this is traditionally presented as a P-P plot, where the P's could stand for either probability or percent (Romero-Shaw et al., 2020; Veitch et al., 2015b; Biwer et al., 2019).

The F2Y injection set includes component masses uniformly distributed from $m_L =$

²lscsoft.docs.ligo.org/gstlal/gstlal/bin/gstlal_fake_frames.html#gstlal-fake-frames

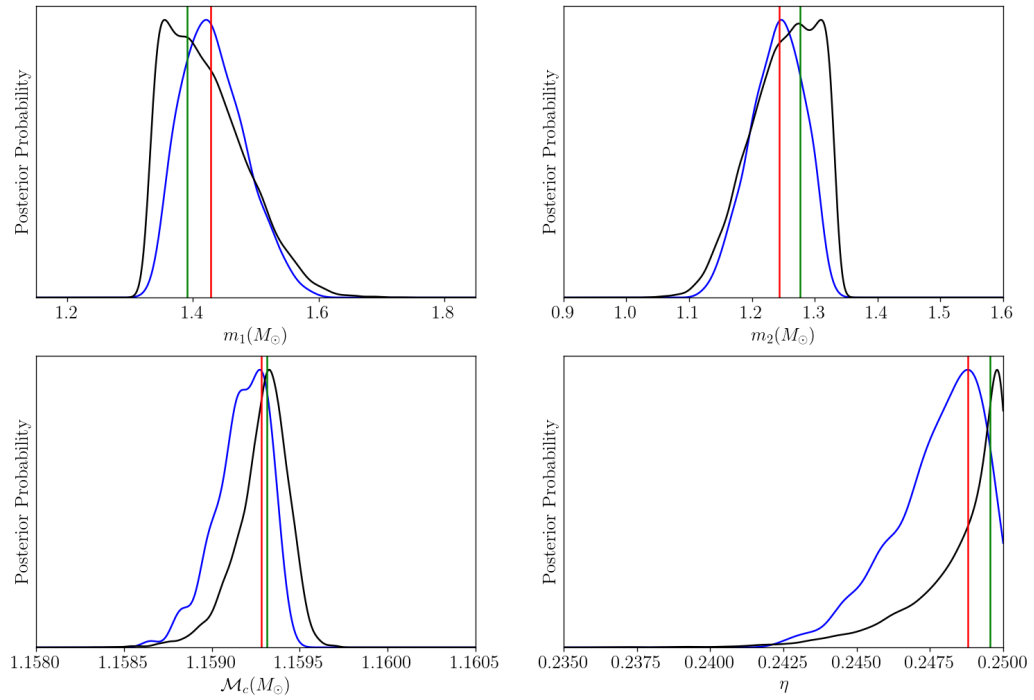


Figure 3.4: Intrinsic posterior plots of event #10184 for three grid levels of the pre-refine scheme. The blue posterior is from RapidPE and the black posterior is from `lalinference_mcmc`. The red lines indicate the injected values, while the green lines indicate the search-recovered values.

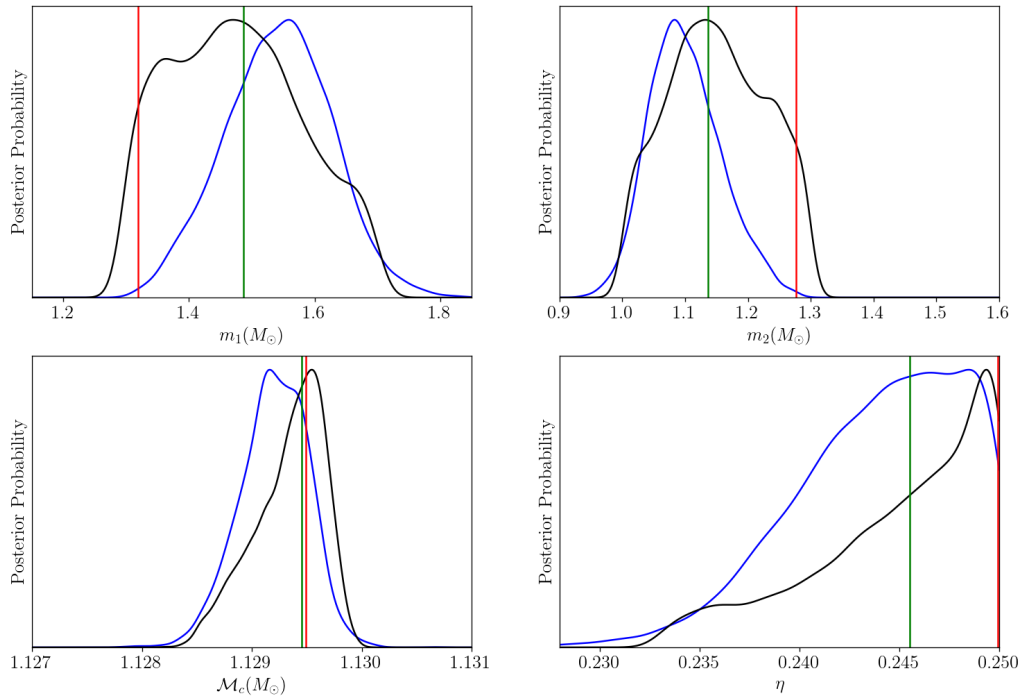


Figure 3.5: Intrinsic posterior plots of event #14631 for three grid levels of the refine (prune) scheme. The blue posterior is from RapidPE and the black posterior is from `lalinference_mcmc`. The red lines indicate the injected values, while the green lines indicate the search-recovered values.

$1.2M_\odot$ to $m_H = 1.6M_\odot$. Therefore the CDF of the posterior over m_1 for each injection is

$$\text{CDF}[\hat{m}_1] = \int_{m_L}^{\hat{m}_1} dm_1 \int_{m_L}^{m_H} dm_2 p(m_1, m_2|d) \quad (3.3)$$

where \hat{m}_1 is the injected value of m_1 and $p(m_1, m_2)$ is the posterior distribution.

By Bayes theorem, the posterior distribution is

$$p(m_1, m_2|d) = \mathcal{L}(m_1, m_2, d) p(m_1, m_2) / \mathcal{Z} \quad (3.4)$$

where $\mathcal{L}(d|m_1, m_2)$ is the likelihood function of the data, $p(m_1, m_2)$ is the prior distribution, and \mathcal{Z} is the evidence

$$\mathcal{Z} = \int_{m_L}^{m_H} dm_1 \int_{m_L}^{m_H} dm_2 \mathcal{L}(m_1, m_2, d) p(m_1, m_2) \quad (3.5)$$

RapidPE implicitly requires $m_1 > m_2$, so our mass prior distribution is

$$p(m_1, m_2) = \frac{\Theta(m_1 - m_2)}{(m_H - m_L)^2} \quad (3.6)$$

where $\Theta(m_1 - m_2)$ is the Heaviside step function.

At each intrinsic grid point, RapidPE calculates the likelihood marginalized over the extrinsic parameters \mathcal{L}_i . To interpolate the marginalized likelihood in intrinsic space, we assume that the marginalized likelihood function is a sum of two-dimensional Gaussian in $\mathcal{M}_c - \eta$ space centered at each grid point with an amplitude of \mathcal{L}_i and a standard deviation of half the grid spacing for each intrinsic parameter. We can approximate the likelihood function as,

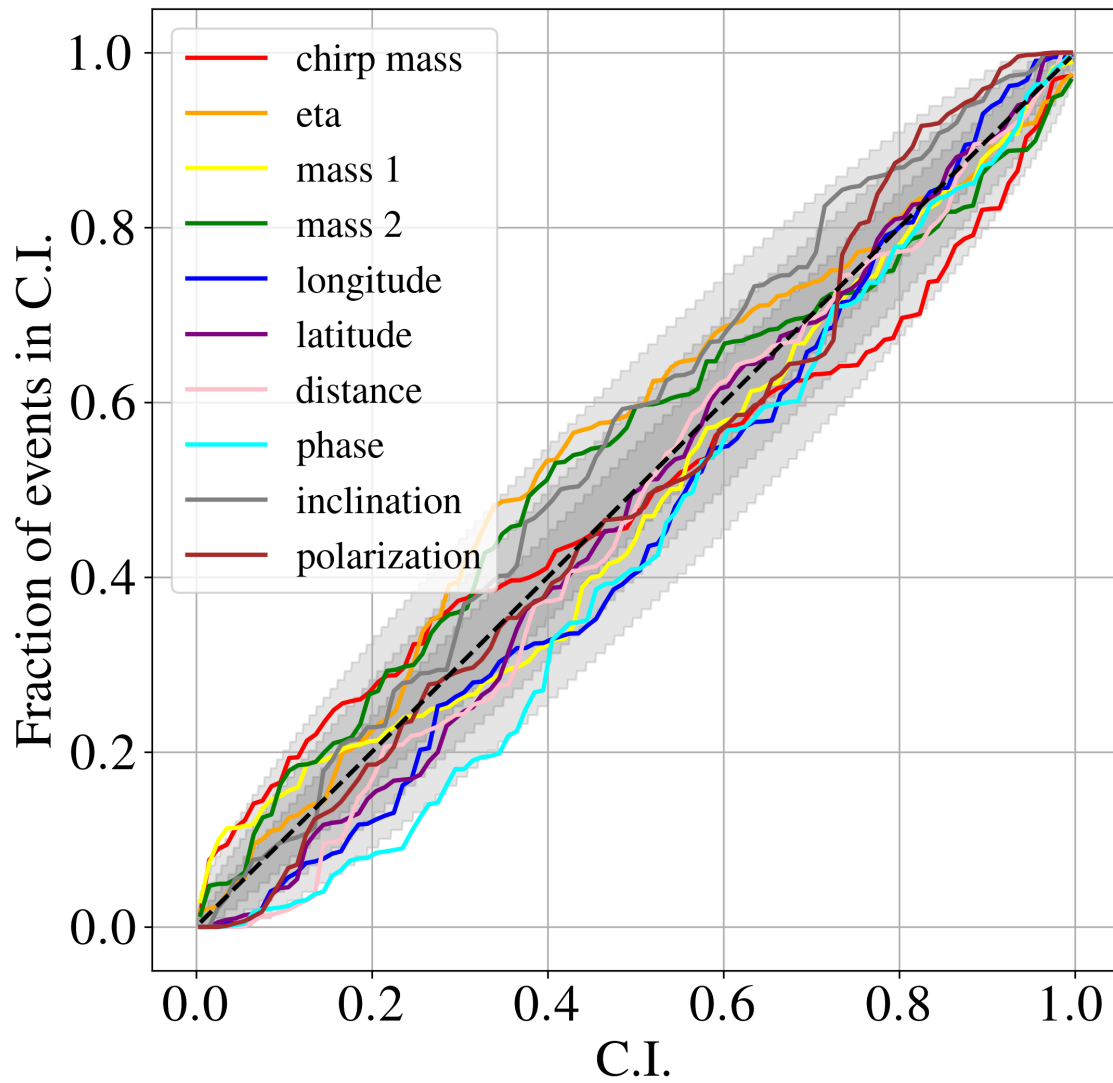


Figure 3.6: AMR RapidPE results on 100 three-detector F2Y 2016 injections for the serial refinement method with three grid levels. The colored lines represent the fraction of events within a given confidence interval (C.I.) for intrinsic and extrinsic parameters. The gray regions mark the cumulative 1-, 2-, and 3- σ confidence intervals in order of decreasing opacity.

$$\mathcal{L}(d|m_1, m_2) \approx \sum_i \mathcal{L}_i \exp \left\{ \frac{-1}{2\sigma_c^2} [\mathcal{M}_c(m_1, m_2) - \mathcal{M}_{ci}]^2 + \frac{-1}{2\sigma_\eta^2} [\eta(m_1, m_2) - \eta_i]^2 \right\} \quad (3.7)$$

where i represents each intrinsic grid point in an injection. σ_c and σ_η are the standard deviations for the Gaussian centered at \mathcal{M}_{ci} and η_i , respectively.

For the extrinsic parameters, we used the likelihood value calculated by RapidPE for each of the extrinsic samples at every grid point along with the given priors to compute the CDF of the posterior up to the injected extrinsic value.

Figure 3.6 shows the result of this validation test, where the confidence interval is plotted against the fraction of injections within that confidence interval. The cumulative 1-, 2-, and 3- σ confidence intervals appear as ovals behind the P-P plots as in [Romero-Shaw et al. \(2020\)](#).

The performance of this parameter estimation algorithm in terms of the computation time will be discussed in the next chapter.

3.4 CONCLUSION

While the original version of RapidPE introduced the method by which we can simplify and parallelize parameter estimation by restricting intrinsic parameters to a grid, it was not flexible enough to overcome search biases. With the AMR grid scheme, we show that the grid can cover more of the posterior without sacrificing sampling efficiency compared previous version. Based on the validity tests illustrated by the P-P plots, we conclude that the updated version of RapidPE presented in this work produces reliable intrinsic and extrinsic results for binary neutron star sources under a variety of conditions and signal-to-noise ratios. This work has shown that the rectilinear grid approach can map the posterior to a point where interpolation is a viable alternative to Markovian sampling and that search biases can be ameliorated through additional grid refinements.

CHAPTER 4

Rapid Parameter Estimation in O4

The fourth observing run (O4) of LIGO detectors (LIGO Hanford Observatory and LIGO Livingston Observatory) started on May 24, 2023, and will continue to take data till early 2025. The Virgo detector has joined this observing run in its second half (O4b) which started on April 2024. KAGRA detector is expected to join O4b in December 2024.

During the first half of the fourth observing run (O4a), there were two high-probability NSBH candidates released as public alerts. Even though expected, there was no significant BNS detection during O4a. Based on the number of detections in the past observing runs and the volume time sensitivity (VT) of current and past observing runs, predictions on the number of detections of BNS and NSBH for O4b are made ([Salafia, 2024](#)). During O4b, the probability of at least one BNS detection is around 73%, and the probability of at least one NSBH detection is 94%. The rate of predicted joint detection of GW+GRB during O4 is $0.75^{+1.16}_{-0.55}\text{yr}^{-1}$ (for Fermi/GBM) ([Colombo et al., 2022](#)). Other works have also predicted the probability of joint detections (GW with electromagnetic counterpart) during O4 as $0.43^{+0.58}_{-0.26}\text{yr}^{-1}$ (for Zwicky Transient Facility) and $1.97^{+2.68}_{-1.2}\text{yr}^{-1}$ (for Rubin Observatory) ([Kiendrebeogo et al., 2023](#))

With these predicted number of BNS and NSBH detections and the joint detections in O4, it is important that the LIGO, Virgo, and KAGRA collaborations are prepared to detect and follow up any BNS and NSBH events in O4 which could potentially lead to a detection like GW170817. Astronomers face numerous considerations when determining whether to attempt observing an electromagnetic counterpart to a GW candidate. To efficiently use the telescope time to follow up a GW candidate, we need to provide the astronomers with accurate sky localization of the GW candidate. Additionally, it is im-

portant to know if we expect the candidate to have an NS component that could have an electromagnetic counterpart. Given these factors, it's important to deliver reliable, low-latency updates on source classification and sky localization of GW candidates to facilitate astronomers' observations of electromagnetic counterparts.

In this chapter, I explain how we use RapidPE for low-latency parameter estimation in O4.

4.1 LOW-LATENCY PIPELINES IN O4

To efficiently follow up on GW events in the electromagnetic spectrum, several tasks must be executed on a low-latency timescale. This includes implementing search pipelines capable of detecting potential signals in the data, as well as subsequent pipelines such as parameter estimation pipelines for data analysis. Additionally, an alert system is necessary to promptly notify astronomers at various observatories for rapid follow-up of these events.

In the current observing run, there are four pipelines utilized for CBC detection. These pipelines (GstLAL ([Messick et al., 2017](#)), PyCBC ([Biwer et al., 2019](#)), MBTA ([Adams et al., 2016](#)), and SPIIR ([Chu et al., 2021](#))) employ matched filtering techniques to detect signals in the GW detector data. They utilize pre-computed banks of gravitational waveform templates, each encompassing a unique combination of mass and spin parameters. Each pipeline utilizes independently constructed template banks. These templates are then used to identify which one produces the highest signal-to-noise ratio (SNR) in the data, with the template yielding the highest SNR designated as the "preferred event" trigger in the online database GraceDB ¹([Moe et al., 2014](#)), the central database and web portal for low-latency LIGO/Virgo analyses.

¹<https://gracedb.ligo.org>

GWCelery² is a package for annotating and orchestrating multiple tasks that need to be done in a low-latency timescale during a detection including collecting and uploading trigger information from the search pipelines to the online database GraceDB, launching multiple data analysis pipelines including parameter estimation pipelines on selected triggers and sends out alerts to astronomers about new events. Search pipelines upload candidate triggers to GraceDB in real-time. Whenever an event is uploaded or altered, GraceDB pushes machine-readable notifications through IGWN Alert³, an alert infrastructure that is powered by Apache Kafka⁴. The role of GWCelery in the LIGO/Virgo alert infrastructure is to drive the workflow of aggregating and annotating GW candidates and sending GCN Notices⁵ to astronomers.

Some of the tasks that are launched by GWCelery in a low-latency timescale are the BAYESTAR skymap, pipelines for source classifications, and pipelines for parameter estimation. BAYESTAR skymap provides the location of the candidate event in the sky and source classification provides an estimated probability of the origin of the trigger being in one of the astrophysical categories(BNS, BBH, and NSBH) and of being a terrestrial origin. I will discuss more on the source classification in Section 4.3.

As part of preparing for O4, we have done multiple developments in RapidPE to assist the multi-messenger astronomy. RapidPE is being launched through GWCelery on GW candidates. In the following sections, I will explain these developments.

4.2 RAPIDPE-RIFT

RIFT (Lange et al., 2018; Wofford et al., 2022) is a parameter estimation scheme that was adapted from RapidPE. RIFT uses the same concept of waveform decomposition, extrin-

²<https://rtd.igwn.org/projects/gwcelery/en/latest/>

³<https://igwn-alert.readthedocs.io/en/latest/index.html>

⁴<https://kafka.apache.org>

⁵<https://gcn.nasa.gov/notices>

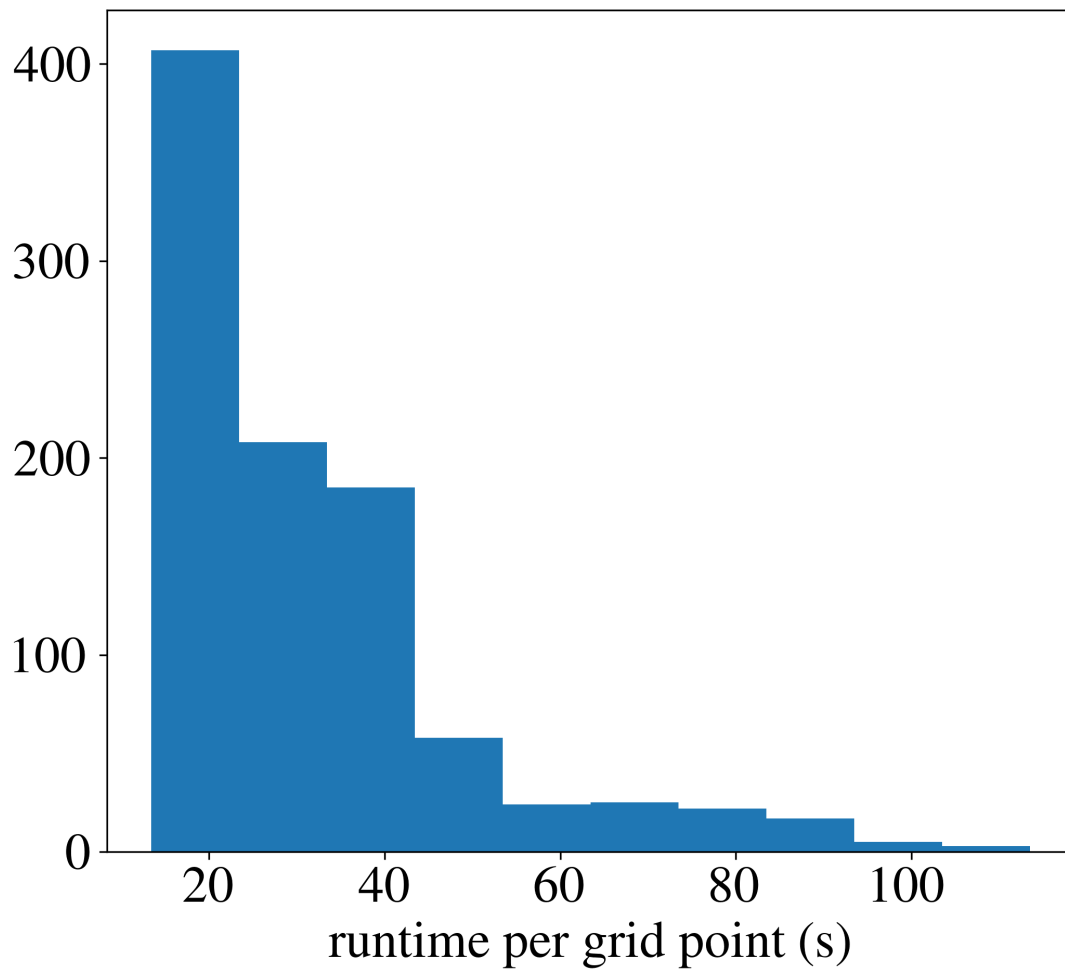
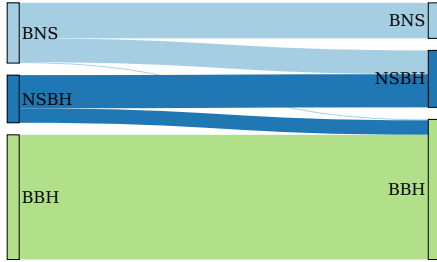


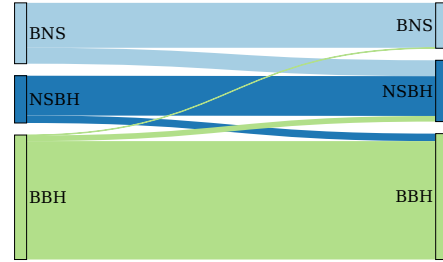
Figure 4.1: Histogram of runtime using RIFT's ILE (with GPU and distance marginalization) on AMR RapidPE estimated for 29 events from O4 each using a 5×5 initial grid for intrinsic parameters with one level of refinement.

sis sampling, and marginalization over extrinsic parameters as in RapidPE. While the new version of RapidPE uses AMR for the intrinsic grid, RIFT uses a Gaussian process interpolation on an unstructured grid. RIFT can rapidly and accurately recover the parameters of GW signal using models and scenarios whose computational cost would be prohibitive for LALInference. While this is not particularly useful for low-latency parameter estimation, RIFT has some speed-up improvements in the extrinsic sampler. RIFT use of GPUs (Wysocki et al., 2019) and distance marginalization is shown to improve the extrinsic sampling by a factor of 10 and 7 respectively. To use these speedup improvements for low-latency we combined the AMR scheme for intrinsic grid placement with the extrinsic sampler from RIFT into a pipeline called RapidPE-RIFT-Pipe (Valsan et al., 2022). The code that computes the marginalized likelihood at each intrinsic point is called Integrate Likelihood Extrinsic (ILE) which does waveform evaluation, extrinsic sampling, and marginalization over extrinsic parameters. The RIFT’s version of ILE includes GPUs and distance marginalization.

The integration of RapidPE-RIFT led to a significant reduction in the average runtime of AMR RapidPE-RIFT, bringing it to less than one minute per grid level when utilizing GPUs. This achievement marks a groundbreaking advancement in Bayesian parameter estimation. Furthermore, completing each additional grid level in approximately half a minute ensures results are delivered well within the required time frame for low-latency alerts. Figure 4.3 plots a histogram of runtime using RIFT’s ILE (with GPU and distance marginalization) on AMR RapidPE estimated for 29 events from O4 each using a 5×5 initial grid for intrinsic parameters with one level of refinement. The figure shows that the average time of evaluation at a grid point is less than a minute. If we have enough computational resources to run ILE on each intrinsic point in a grid parallelly, then the average overall time of the complete parameter estimation with AMR RapidPE-RIFT will



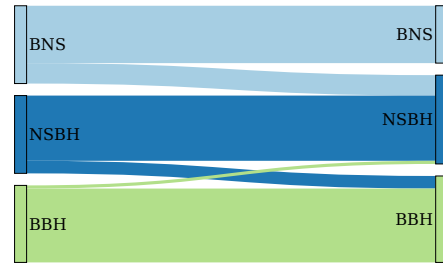
(a) GstLAL by count



(b) RapidPE by count



(c) GstLAL by percent



(d) RapidPE by percent

Figure 4.2: Sankey Diagrams comparing the source classification from RapidPE and GstLAL in count and percentage.

be the number of grid levels multiplied by the average time spent on ILE for each grid point.

For an online run during O4, we typically use ≈ 100 intrinsic grid points with one level of refinement on the initial grid. If we have enough resources (GPUs) to run each grid point in a single grid level parallelly, on an average RapidPE can produce parameter estimation results in two minutes.

True Source	Count		
	BNS	NSBH	BBH
BNS	76.6	51.6	2.8
NSBH	0.0	71.3	31.7
BBH	0.0	0.0	268.0

(a) GstLAL by count

True Source	Count		
	BNS	NSBH	BBH
BNS	96.9	34.1	0.0
NSBH	0.8	85.7	16.5
BBH	2.0	12.8	253.3

(b) Rapid PE by count

True Source	Percentage		
	BNS	NSBH	BBH
BNS	58.4	39.4	2.1
NSBH	0.0	69.3	30.7
BBH	0.0	0.0	100.0

(c) GstLAL by percent

True Source	Percentage		
	BNS	NSBH	BBH
BNS	73.9	26.1	0.0
NSBH	0.8	83.2	16.0
BBH	0.7	4.8	94.5

(d) Rapid PE by percent

Table 4.1: Data for Sankey Diagrams

4.3 P-ASTRO: SOURCE CLASSIFICATION

Accurate and reliable source classification is important for efficient electromagnetic follow-up. Since we expect binaries with an NS component to have electromagnetic counterparts, it is important to know the probability of an event having an NS component to decide if it is worth following up. This information helps astronomers to efficiently use the limited resources and time of telescopes. For this purpose, different pipelines running in the low-latency timescale provide this information to the public. This data product is called P-Astro ([Kapadia et al., 2019](#)).

P-Astro is a source classification scheme that provides estimates for the probability of the source of GW signal being in one of the astrophysical categories (BNS, NSBH, and BBH) and the probability of terrestrial origin, meaning the signal is simply noise. All the search pipelines provide a P-Astro data product based on the search estimated point within a few seconds of detection. While all search pipelines use a matched filtering technique to detect a GW signal in the data, subtle differences such as differences in the template bank, difference in the waveform, differences in the ranking statistics could re-

sult in differences in the search estimated point between each search pipeline and thereby a difference in the P-Astro as well. So, it is important to have a more accurate P-Astro data product based on parameter estimation results within a few minutes of detection. For this, we developed a method to compute P-Astro from RapidPE-RIFT results.

In terms of the Bayesian notation defined in Section 2.3, P-Astro is defined as the probability of the Alternate hypothesis being true given the data ($\mathcal{P}_{\text{astro}} = p(\mathcal{H}_1|d)$). Then, from completeness relation

$$p(\mathcal{H}_1|d) + p(\mathcal{H}_0|d) = 1, \quad (4.1)$$

where $p(\mathcal{H}_0|d)$ is called $\mathcal{P}_{\text{terr}}$ which gives the probability of the signal being of terrestrial origin. We can define $p(\mathcal{H}_0|d)$ as

$$p(\mathcal{H}_0|d) = 1 - \int p(\vec{\mu}, \mathcal{H}_1|d) d\vec{\mu}. \quad (4.2)$$

Using the the equation of posterior (Equation 2.34) and writing in terms of the evidence ratio \mathcal{Z}

$$p(\mathcal{H}_0|d) = \mathcal{P}_{\text{terr}} = 1 - \frac{\mathcal{Z}}{\frac{p(\mathcal{H}_0)}{p(\mathcal{H}_1)} + \mathcal{Z}}. \quad (4.3)$$

Solving for $\frac{p(\mathcal{H}_0)}{p(\mathcal{H}_1)}$,

$$\frac{p(\mathcal{H}_0)}{p(\mathcal{H}_1)} = \frac{\mathcal{Z}\mathcal{P}_{\text{terr}}}{1 - \mathcal{P}_{\text{terr}}}. \quad (4.4)$$

Rewriting Equation 2.34 using Equation 4.4,

$$p(\vec{\mu}, \mathcal{H}_1|d) = (1 - \mathcal{P}_{\text{terr}}) \frac{\mathcal{L}(\vec{\mu}, d) \pi(\vec{\mu}|\mathcal{H}_1)}{\mathcal{Z}}. \quad (4.5)$$

Let's divide the Alternate hypothesis into sub-hypothesis(\mathcal{H}_α) such that each hypothesis provides the probability of the trigger being in a specific astrophysics category. I

will be defining these sub-hypotheses later in this section that satisfies $\mathcal{H}_1 = \cup_\alpha \mathcal{H}_\alpha$ and $\mathcal{H}_\alpha \cap \mathcal{H}_\beta = \emptyset$ for $\alpha \neq \beta$. Rewriting prior as,

$$\pi(\vec{\mu}|\mathcal{H}_1) = \sum_{\alpha} \pi(\vec{\mu}, \mathcal{H}_\alpha|\mathcal{H}_1)p(\mathcal{H}_\alpha|\mathcal{H}_1), \quad (4.6)$$

where $p(\mathcal{H}_\alpha|\mathcal{H}_1)$ is the probability of \mathcal{H}_α under the alternate hypothesis. Substituting Equation 4.6 in to the definition of evidence (Equation 2.33),

$$\mathcal{Z} = \sum_{\alpha} \mathcal{Z}_\alpha p(\mathcal{H}_\alpha|\mathcal{H}_1), \quad (4.7)$$

where \mathcal{Z}_α is

$$\mathcal{Z}_\alpha = \int \mathcal{L}(\vec{\mu}, d)\pi(\vec{\mu}, \mathcal{H}_\alpha|\mathcal{H}_1)d\vec{\mu}. \quad (4.8)$$

Finally, the probability of \mathcal{H}_α being true given the data under the alternate hypothesis is

$$\mathcal{P}_\alpha = p(\mathcal{H}_\alpha, \mathcal{H}_1|d) = (1 - \mathcal{P}_{\text{terr}}) \frac{\mathcal{Z}_\alpha p(\mathcal{H}_\alpha|\mathcal{H})}{\sum_{\beta} \mathcal{Z}_\beta p(\mathcal{H}_\beta|\mathcal{H})}. \quad (4.9)$$

Note that \mathcal{P}_α agrees completeness relation

$$\sum_{\alpha} \mathcal{P}_\alpha = \mathcal{P}_{\text{astro}} = 1 - \mathcal{P}_{\text{terr}}. \quad (4.10)$$

The terms $p(\mathcal{H}_\alpha|\mathcal{H})$ can be rewritten in terms of the rate of occurrence of events in α -category (\mathcal{R}_α) as

$$p(\mathcal{H}_\beta|\mathcal{H}) = \frac{\mathcal{R}_\beta}{\sum_{\beta} \mathcal{R}_\beta}. \quad (4.11)$$

Then we can rewrite 4.9 as,

$$\mathcal{P}_\alpha = (1 - \mathcal{P}_{\text{terr}}) \frac{\mathcal{Z}_\alpha \mathcal{R}_\alpha}{\sum_{\beta} \mathcal{Z}_\beta \mathcal{R}_\beta} \quad (4.12)$$

In O4, we are considering three categories, $\alpha = \{\text{BNS}, \text{NSBH}, \text{BBH}\}$. The template banks used has a boundary of $0.98 < m < 200$. With these, the boundaries of different categories are defined as

$$\text{BNS} : 0.98M_{\odot} \leq (m_1, m_2) < 3M_{\odot} \quad (4.13)$$

$$\text{NSBH} : 0.98M_{\odot} \leq m_2 < 3M_{\odot}; \quad 3M_{\odot} \leq m_1 < 200M_{\odot} \quad (4.14)$$

$$\text{BBH} : 3M_{\odot} \leq (m_1, m_2) < 200M_{\odot} \quad (4.15)$$

By numerically integrating the Gaussian interpolated likelihood, we compute evidence \mathcal{Z} and category-specific evidence \mathcal{Z}_{α} . To estimate the $\mathcal{P}_{\text{terr}}$ we need to know the false alarm rate. Instead of devising a method to estimate $\mathcal{P}_{\text{terr}}$, we rely on the $\mathcal{P}_{\text{terr}}$ estimated by the search pipeline, which I will denote by $\mathcal{P}'_{\text{terr}}$. So, in implementation, instead of computing $\mathcal{P}_{\text{astro}} = \sum_{\alpha} \mathcal{P}_{\alpha}$, we compute normalized category specific probability ($\bar{\mathcal{P}}_{\alpha}$) such that

$$\sum_{\alpha} \bar{\mathcal{P}}_{\alpha} = 1 \quad (4.16)$$

Then \mathcal{P}_{α} can be written in terms of $\mathcal{P}'_{\text{terr}}$ and $\bar{\mathcal{P}}_{\alpha}$ as

$$\mathcal{P}_{\alpha} = \bar{\mathcal{P}}_{\alpha}(1 - \mathcal{P}'_{\text{terr}}) \quad (4.17)$$

4.3.1 Comparison with Search Pipeline P-Astro

The goal of RapidPE-RIFT P-Astro is to provide a source classification estimate as an update to the source classification provided by the search pipelines. We have tested the accuracy of P-Astro source classification from AMR RapidPE-RIFT and compared it against the estimate from the search pipelines. For this, we used simulated BNS, NSBH and BBH injections from the Mock Data Challenge (MDC) performed just before the start of O4.

We have computed P-Astro for 502 simulated signals (injections) from one week of MDC using AMR RapidPE-RIFT. Since these are not real GW events, instead of using astrophysical rates, we used the fraction of injections in each category as their rate in the P-Astro calculation. The prior used in the calculation is the same as the distribution function used to create these injections. The prior used are uniform in both component masses in BNS, uniform in secondary mass and power-law distribution of m_1^{-1} for the primary mass in NSBH and power-law distribution of $m_1^{-2.35}$ for the primary mass and m_2 for the secondary mass in BBH. The results are presented in Figure 4.2 and the corresponding data in Table 4.1. The top panels in this figure compare P-Astro computed by GstLAL with P-Astro computed by AMR RapidPE-RIFT in terms of the count of injections in each category. The bottom panels compare the same but the number of injections in each category is normalized to be the same. Note that in all four plots, we normalized P-Astro values such that the astrophysical probability of each injection adds to 1 (in other words $\mathcal{P}_{\text{terr}} = 0$ for each injection). These figures demonstrate that BNS and NSBH injection gets classified into their true category more accurately for RapidPE. Particularly, the misclassification of BNS and NSBH signals into BBH is comparatively small for RapidPE-RIFT.

4.4 AMR RAPIDPE-RIFT IN O4

During O4, GWCelery submits an AMR RapidPE-RIFT analysis on every GW candidate within the PE FAR threshold ($3.8 \times 10^{-7} s^{-1}$). For all these GW candidates a public alert is sent out to notify astronomers.

For these online runs, we use AMR RapidPE-RIFT with ~ 100 intrinsic grid points with an additional level of refinement around the highest likelihood points. As noted earlier, while we use the AMR grid (a rectilinear grid) in O4, the initial grid is not computed based on the overlap calculation. Instead, we use the measured bias in the estimation of

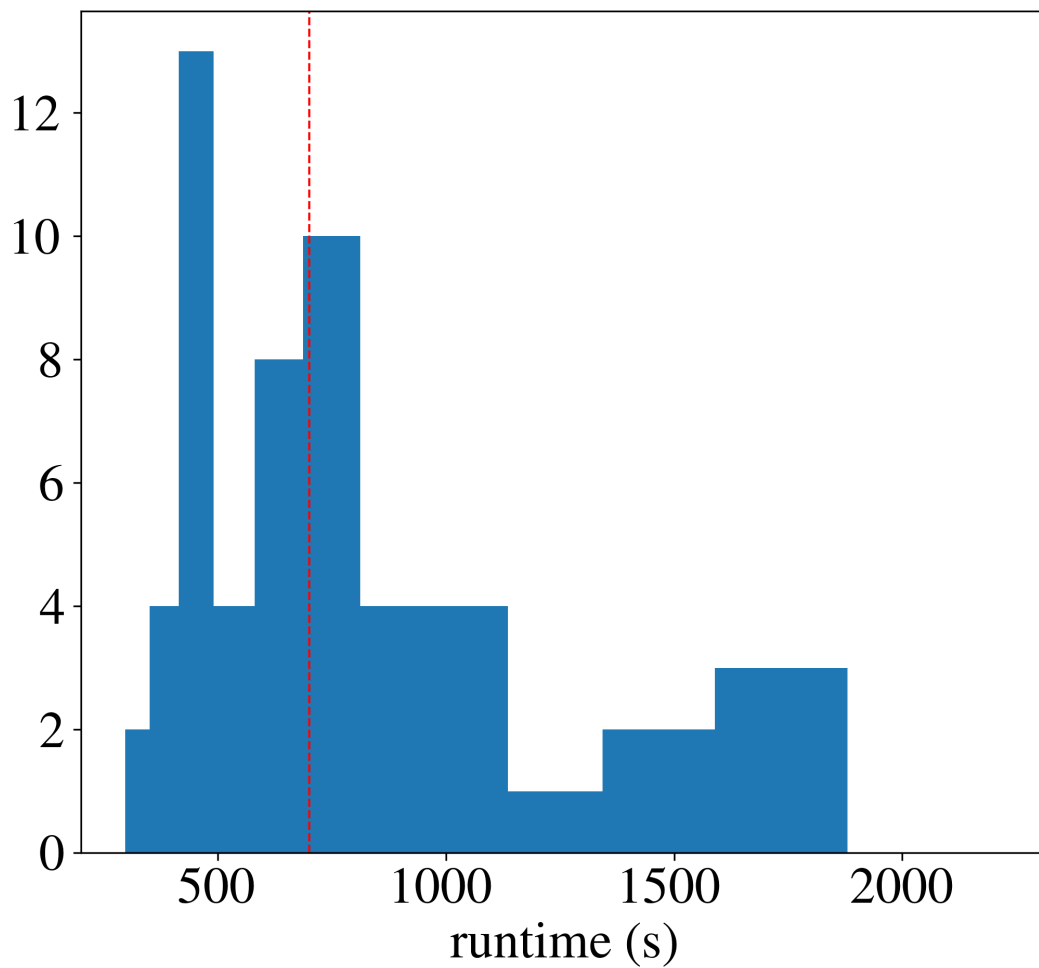


Figure 4.3: Histogram of runtime for AMR RapidPE-RIFT for events in O4. The red dashed line represents the mean of the histogram.



(a) PyCBC: Submitted by LIGO/Virgo EM Follow-Up on April 13, 2024, 02:25:29 UTC

(b) AMR RapidPE-RIFT: Submitted by LIGO/Virgo EM Follow-Up on April 13, 2024, 02:34:46 UTC

Figure 4.4: Comparison between P-Astro from PyCBC and AMR RapidPE-RIFT taken from GraceDB for the event S240413p in O4b

component masses from the search pipelines to generate an informed initial region. The search bias is measured using MDC performed before the start of O4. For more details on this process refer to [Rose \(2024\)](#). This step is pre-computed and does not add to the run time of completing the parameter estimation during the O4 online run.

Figure 4.3 shows a histogram of runtime for completing AMR RapidPE-RIFT runs in O4. Here the runtime represents the time taken by AMR RapidPE-RIFT to complete the parameter estimation starting from identifying the initial grid region to computing the P-Astro source classification. Runtime is calculated for the O4 events for which a RapidPE-RIFT analysis is submitted through GWCelery. The red dashed line in Figure 4.3 represents the mean of the histogram which is ≈ 12 minutes. Note that unlike in Figure 4.3 which shows the histogram of runtime per grid point, the numbers in Figure 4.3 are runtime per trigger which includes the run time for two grid levels, time taken to set up each grid level and the time taken for P-Astro calculation. Additionally, no events in O4 used GPUs for the AMR RapidPE-RIFT runs.

Three kinds of GCN Notices⁶ issued by GWCelery could include AMR RapidPE-RIFT source classification. During the first half of O4 (O4a), AMR RapidPE-RIFT source classification was not included in any of the low-latency Notices but is included in the Update Notice which is sent whenever there is an update to sky localization of source classification through the parameter estimation results. The Update Notice is accompanied by a GCN Circular. In the second half of the fourth observing run (O4b), AMR RapidPE-RIFT source classification is included in the Initial Notice which is issued after human vetting accompanied by a GCN Circular. Another kind of notice, called the Second Preliminary is sent approximately 5 minutes after after a gravitational-wave candidate is detected. These are automatic alerts and are not accompanied by a circular. If AMR RapidPE-RIFT source classification results are available before the Second Preliminary is sent, AMR RapidPE-RIFT source classification can be included in that.

Figure 4.4 shows a sample comparison between the source classification from AMR RapidPE-RIFT and the search pipeline PyCBC. These plots are taken from GraceDB for the event S240413p⁷. For this event, the PyCBC pipeline identified trigger is the highest SNR trigger, and the PyCBC plot in Figure 4.4 is taken from the highest SNR trigger. PyCBC classified this trigger as 54% NSBH, 44% BBH, and 2% Terrestrial, while RapidPE-RIFT after the parameter estimation classified this as 98% BBH. Since RapidPE-RIFT does not calculate the $\mathcal{P}_{\text{terr}}$, the $\mathcal{P}_{\text{terr}}$ calculated by PyCBC gets carried over to RapidPE-RIFT plot. RapidPE-RIFT provided this updated source classification approximately 9 minutes after the PyCBC uploaded the source classification. A GCN Notice (Initial Notice) was sent out with RapidPE-RIFT source classification⁸

In addition to the above-mentioned developments in code bases, I have developed a

⁶<https://emfollow.docs.ligo.org/userguide/content.html>

⁷<https://gracedb.ligo.org/superevents/S240413p/view/>

⁸https://gcn.gsfc.nasa.gov/notices_1/S240413p.lvc

real-time monitoring tool to monitor the AMR RapidPE-RIFT runs during O4b ([Valsan & Wysocki, 2024](#)).

CHAPTER 5

Common Envelope Evolution

5.1 OVERVIEW

Common-envelope evolution (CEE) ([Paczynski, 1976](#)) is an important phase in the life of many binary star systems during which two stars orbit inside a single shared envelope. It is believed to be responsible for the production of many close binary systems including white dwarf binaries, X-ray binaries, BNS, and BBH (for a review see [Ivanova et al. \(2013, 2020\)](#)).

During a CEE, a binary star system consisting of a giant star and a companion star starts to inspiral when the giant star evolves and expands to engulf the companion. The core of the giant star and the companion orbit each other inside this shared envelope and inspiral. During inspiral, orbital energy and angular momentum are lost due to frictional drag eventually bringing the two stars into a close orbit. The loss of energy to the envelope could lead to an envelope ejection and/or the merger of the binary star system. So, a CEE could result in a close binary system or a single star making it an important stage in the evolution of not only binary star systems but also single stars. Figure 5.1 shows some examples of evolution channels involving the common envelope (CE) phase.

CEE has an important role in the evolution of stellar mass gravitational wave sources such as BBH, BNS, and NSBH because it helps bring the stars sufficiently close together to merge within the age of the universe via the emission of gravitational waves ([Belczynski et al., 2001](#)). For instance, figure 5.1 shows an example of a formation channel for a BNS system involving a CE phase.

Formation channels of both short-duration and long-duration GRBs are proposed to involve the CE phase. The discovery of the sGRB GRB170817A as a result of the BNS

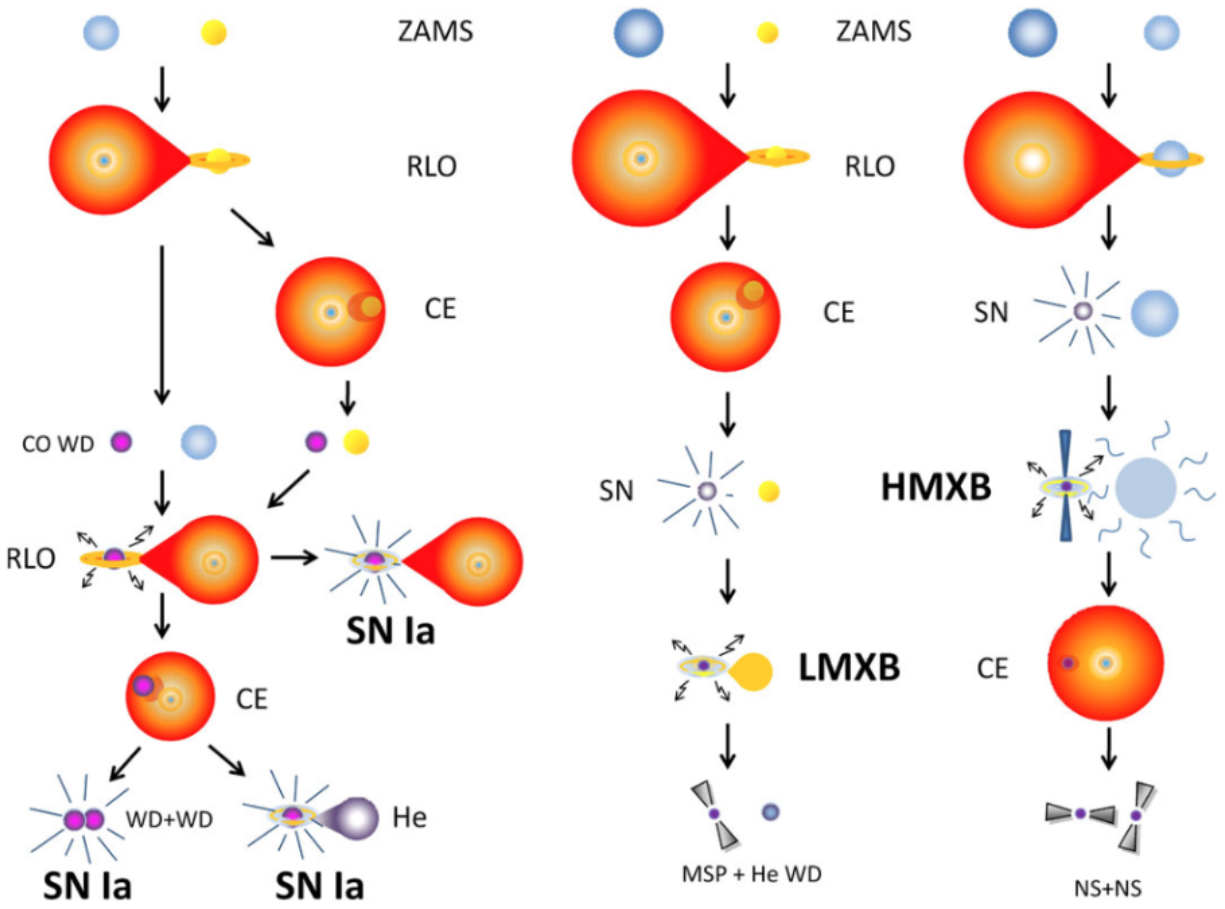


Figure 5.1: Examples of evolutionary channels of some binary star systems involving common envelope phase, reprinted from [Ivanova et al. \(2013\)](#).

merger event GW170817 supports this (Abbott et al., 2017b). The long-duration GRBs are thought to arise from the core collapse of massive stars which are rapidly rotating to cause massive accretion disk and have the envelope stripped to allow the GRB to escape. It is proposed that the spun-up and envelope stripping can be achieved through multiple formation channels involving CE (Fryer et al., 1999, 2007; Podsiadlowski et al., 2010).

Another astrophysical phenomenon that is expected to involve CEE is the merger of carbon-oxygen white dwarfs (CO WDs) which is potentially responsible for Type Ia supernovae (SNe Ia) (Webbink, 1984). The initial separation of such binaries needs to be wide enough to allow one or both stars to evolve to be massive CO WDs. If the orbital separation becomes small enough this can lead to a merger through gravitational wave emission. Figure 5.1 schematically describes two potential channels leading to an SNe Ia. A binary evolution can also involve more than one CE stage as shown in Figure 5.1.

Low-mass X-ray Binaries (LMXBs) are accreting neutron stars or black holes with low-mass companions. The orbital shrinkage in such systems is explained through multiple formation channels involving CE (Kalogera & Webbink, 1998), also shown in Figure 5.1. Other examples of binary systems involving the CE phase are cataclysmic variables, high-mass x-ray binaries, and binary radio pulsars (Taam, 1996).

5.1.1 Phases of CEE

Studying CEE is extremely challenging for both computational and analytic treatments as it involves a complex mix of physics happening over a range of time scales. It is useful to break down the evolution of CE events into distinct phases with their associated time scales and their different physics (Podsiadlowski, 2001).

5.1.1.1 *Loss of Co-rotation*

During this stage, a binary in a stable orbit loses its tidally synchronized orbital dynamics and spirals in towards each other. When the donor star expands beyond its Roche Lobe either as a reaction to sudden mass loss or due to evolution, the tidal forces can no longer maintain the co-rotation leading to inspiral. Loss of co-rotation could also be caused by instabilities such as a Darwin Instability (Darwin, 1879). The Darwin instability occurs when the spin angular momentum of the system is more than a third of its orbital angular momentum. Beyond this threshold of angular momentum, the tidal forces within the binary system become strong enough to induce a runaway transfer of angular momentum from the orbital motion to the spin of the individual stars disrupting the synchronized orbital dynamics of the system. The loss of co-rotation happens in a dynamic time scale. The onset of this dynamical instability largely depends on the mass transfer history of the system which could be happening for hundreds or thousands of years as it operates on a thermal timescale.

5.1.1.2 *Plunge-in*

A radial spiral-in phase starts when the co-rotation between the envelope and the binary is rapidly lost. During this phase, orbital energy is lost from the binary due to friction between the envelope and the binary, causing the binary to spiral in. The energy lost due to friction is deposited in the envelope which could lead to a complete ejection of the envelope from the system or a rapid merger of the binaries.

5.1.1.3 *Self-regulating spiral-in*

Once the orbital decay due to friction deposits enough energy in the envelope causing significant expansion and assuming that it is not completely ejected the binary's spiral-in

slows down. This happens when any additional energy deposited to the envelope due to friction is transported to the surface by convection and radiated away (Meyer & Meyer-Hofmeister, 1979). This stage could last hundreds of years as it happens on a thermal time scale.

5.1.1.4 Termination of Self-Regulating Phase

Depending on the energy deposited in the envelope the self-regulated spiral-in could end in an envelope ejection (Ivanova, 2002; Han et al., 2002) or due to stellar evolution the core of the primary donor star of the companion star could expand to fill the Roche Lobe leading to a secondary stage of Common Envelope evolution. This stage can again lead to envelope ejection or a merger.

5.1.2 Energy Formalism

Energy formalism is the standard analytical way of predicting the fate of a common envelope event by comparing the orbital energy difference between the system before and after the common envelope phase to the energy required to eject the envelope from the system. The difference between orbital energy is given by

$$\Delta E_{\text{orb}} = E_{\text{orb},i} - E_{\text{orb},f} = -\frac{Gm_1m_2}{2a_i} + \frac{Gm_{1,c}m_2}{2a_f} \quad (5.1)$$

Here a_i and a_f are the initial and final orbital radius, m_1 and m_2 are the initial masses of the component stars, and $m_{1,c}$ is the mass of the core of the donor star after it lost $m_{1,\text{env}}$ as the envelope.

The energy required to disperse the envelope to infinity, E_{bind} is given by,

$$E_{\text{bind}} = \frac{m_1m_{1,\text{env}}}{\lambda R_1} \quad (5.2)$$

The parameter λ is introduced to account for the particular structure of the star and is extremely sensitive to the definition of the boundary between the core and the envelope (Tauris & Dewi, 2001). Note that not all orbital energy can be efficiently used to drive the envelope ejection. To account for the fraction of orbital energy used for envelope ejection, a parameter α_{CE} which is called common-envelope efficiency is introduced. If all all envelope material is ejected with precisely the local escape velocity then $\alpha_{\text{CE}} = 1$.

Combining ΔE_{orb} and the concept of α_{CE} with E_{bind} gives the most commonly used form of energy formalism

$$\frac{m_1 m_{1,\text{env}}}{\lambda R_1} = \alpha_{\text{CE}} \left(-\frac{Gm_1 m_2}{2a_i} + \frac{Gm_{1,c} m_2}{2a_f} \right) \quad (5.3)$$

It is important to note that the standard energy formalism in Equation 5.3 presumes that the only energy available for the envelope is the orbital energy stored in the binary system. This assumption is valid as long as the Common Envelope is taking place in a dynamic time scale and other sources of energy do not play an important role. In a less ideal common envelope, there will be more sources and sinks for energy which becomes important depending on the time scale in which the common envelope evolves.

Potential sources are the energy from nuclear burning which either could be happening at the base of the common envelope or the surface of the accretor. Possible sinks of energy are radiative losses for the common envelope and energy that gets stored as the internal energy or the thermal energy of the matter in the envelope.

How long the common envelope phase lasts may determine which of these energy sources and sinks becomes important in our description. If the common envelope is evolving in a thermal timescale, then more will be the energy lost through radiation. In this time scale, we might also need to consider the energy input from the burning core. Similarly, considering nuclear burning in the energy formalism is not as straightforward

as nuclear burning and the associated energy output could increase or decrease as the stars in the binary system evolve through different stages due to accretions and/or mass loss. It is very difficult to make general statements about the energy involved in the envelope ejection once the CE becomes non-dynamical and in this scenario, the general energy formalism above is not expected to work. Below I will discuss different energy sinks and sources.

5.1.2.1 *Loss of Orbital Energy*

There are multiple ways the energy lost from the orbital decay can be deposited in the envelope. Generally, it is assumed to heat the material locally due to friction. Another possibility is that the spiral shocks in the tidal arms trailing the orbital binary can transfer angular momentum to the envelope. This can also result in heating the matter far from the boundary between the envelope and the stars or near the accretion. It is also possible that the orbital energy can be directly converted to kinetic energy through these spiral shocks and as a result, some matter is flung out of the system.

5.1.2.2 *Components of Energy*

The contribution of internal energy in envelope ejection was first applied in [Han et al. \(1994\)](#) and later it became standard to consider internal energy in these discussions. It is natural to consider internal energy as an energy source and modify the definition of E_{bind} accordingly.

$$E_{\text{bind}} = \int_{\text{core}}^{\text{surface}} (\Psi(m) + \epsilon(m)) dm \quad (5.4)$$

where $\Psi(m) = -Gm/r$ is the gravitational potential energy and $\epsilon(m)$ is the internal energy.

One component of internal energy is the thermal energy (U_{th}). This includes the internal kinetic energy stored in the particles and the energy stored in radiation. Another component of internal energy is the recombination energy (E_{recomb}). This is the energy released when the plasma recombines to form molecules from atoms. Another energy source that could play a role in envelope ejection is nuclear fusion (Ivanova, 2002; Ivanova & Podsiadlowski, 2003). I will discuss more about the contribution of these energies in the envelope ejection in Chapter 6.

5.2 OBSERVATIONS

Following a binary star system through its stellar evolution to study CEE is difficult as different time scales are involved in each stage of the stellar evolution. Therefore the most natural way to study the observational appearance of a CEE is through its characteristic post-common envelope outcomes such as the compact binaries and the nebulae and the pre-common envelope stages such as the evolution of the binary stars.

Paczynski (1976) proposed that a discovery of a short-period binary as the nucleus of a planetary nebulae (PNe) would provide support for CEE. Following this, the UU Sge/Abell 63 (Bond et al., 1978) system which contains a hot star that has ionized the planetary nebulae (Abell 63) is proposed to be the core of a red giant exposed by a common envelope ejection. The central binary in this system (UU Sge) has a close separation of $3R_{\odot}$ as a consequence of the orbital decay during CEE. This study is regarded as central for developing common envelope evolution as an important process in the formation of close binaries. We expect that over 20% of PNe contains a post-CE close binary central star of planetary nebulae (close binary CSPNe) (Jones, 2018). These systems are examples of post-common envelope configuration relatively soon after the envelope ejection.

Besides the near existence of close binaries as CSPNe, observation of PNe can give

information about the fluid flows in the ejected envelope such as the velocity and angular momentum distribution in the material and the shape of the PNe. If the dense material is ejected through the orbital plane and the less dense faster material ejects through polar regions, it is natural to associate the bipolar PNe with CE ejections. Using the population model, [Han et al. \(1995\)](#) and [Soker & Rappaport \(2000\)](#) showed that the formation of bipolar PNe is consistent with being dominated by systems in which binary interactions. Interestingly, Abell 63, which has not previously been classified as a bipolar PNe was determined to be so by [Mitchell et al. \(2007\)](#) through difference in the velocity of ejecta in the orbital plane and the polar directions.

Over the past few decades, observers have identified a subclass of transients that are brighter than novae but dimmer than supernovae with total output energy between 10^{45} to 10^{47} ergs and are proposed to be the outcome of a stellar merger. These are called Intermediate Luminosity Optical Transients (ILOT) due to their luminosity or Luminous Red Novae (LRN) as their light curve is predominantly red ([Kasliwal, 2012](#)). Over the past few decades, multiple transient observations have been proposed to have originated from a stellar merger. For example, the well-studied ten-year observation of V1309 Sco showed a decaying orbital period over 5 years before its outburst ([Tylenda et al., 2011](#)). As the orbital period weakened, the second maximum in the light-curve which corresponds to the secondary star became weaker because it was engulfed by the primary. It was also confirmed that following the outburst the remnant shows no sign of a binary. Another The outburst of V838 Mon has also been interpreted as a stellar merger ([Bond et al., 2003](#); [Tylenda et al., 2005](#)). Other proposed candidates of this class are M85 OT2006-1 ([Kulkarni et al., 2007](#)), 1994 outburst of V4332 Sagittarii ([Martini et al., 1999](#)), M31LRN 2015 ([MacLeod et al., 2017](#)) and PTF 10fqs ([Kasliwal, 2012](#)).

5.3 SIMULATING CEE

Simulations of CEE are difficult as they involve complex physics and different time scales. We do not have codes that can evolve a CE phase from beginning to end and hence the convention is to break CEE into different phases explained in Section 5.1.1 for each of which a different physics will be dominant.

During the rapid inspiral phase, dynamical processes dominate and in this case, two numerical methods are widely used in simulating the evolution of astrophysical objects or astrophysical phenomena. These numerical methods are smoothed-particle hydrodynamics (SPH) and Eulerian grid codes. Each method has its advantages and limitations. There is a method that is a combination of both SPH and Eulerian methods called the Arbitrary Lagrangian-Eulerian (ALE) code. In Section 5.3.2-5.3.4, I will discuss the advantages and disadvantages of each of these methods.

Before I discuss the different methods used in simulation CEE, it is useful to understand the basic equations of hydrodynamics that define the evolution of the fluid in these hydrodynamic simulations.

5.3.1 Equations of Hydrodynamics

The fundamental equations of fluid dynamics, known as the Navier-Stokes equations, govern the behavior of fluid flow. These equations describe the conservation of mass, momentum, and energy for a fluid. Under conditions where viscosity is negligible, the Navier-Stokes equations simplify to the Euler equations, governing the motion of an inviscid fluid (non-viscous fluid). This is generally a valid approximation in astrophysical simulation due to the high Reynolds number, where inertial forces outweigh viscous

forces. The Euler equation in conservative form in 3D is given by,

$$\frac{\partial \rho}{\partial t} + \nabla \cdot (\rho \mathbf{v}) = 0 \quad (5.5)$$

$$\frac{\partial \rho \mathbf{v}}{\partial t} + \nabla \cdot \rho \mathbf{v} \mathbf{v} + \nabla P = -\rho \nabla \Phi \quad (5.6)$$

$$\frac{\partial \rho e}{\partial t} + \nabla \cdot (\rho e + P) \mathbf{v} + \nabla P = -\rho \mathbf{v} \cdot \nabla \Phi \quad (5.7)$$

where ρ is the density of the fluid, \mathbf{v} is the velocity, Φ is the gravitational potential, $e = \epsilon + v^2/2$ is the specific energy, ϵ is the internal energy. The pressure term $P(\rho, \epsilon)$ is the equation of state (EOS). Equations 5.5-5.7 can be written in a compact form as

$$\frac{\partial \mathbf{u}}{\partial t} + \int_V \nabla \cdot \mathcal{F} dV = \mathcal{S}, \quad (5.8)$$

where the state vector $\mathbf{u} = (\rho, \rho \mathbf{v}, \rho e)$, the flux $\mathcal{F} = (\rho \mathbf{v}, \rho \mathbf{v} \mathbf{v}, (\rho e + P) \mathbf{v})$ and the source term $\mathcal{S} = (0, -\rho \nabla \Phi, -\rho \mathbf{v} \cdot \nabla \Phi)$.

5.3.2 Smooth Particle Hydrodynamics

SPH is a Lagrangian particle-based approach to solving hydrodynamical equations. This is one of the oldest methods used in astrophysical simulation. SPH simulation works by dividing the fluid into a collection of particles with masses and position and the gas density field is represented by a kernel density sum. The properties of this particle evolve following Euler Equations, written in the Lagrangian reference frame. For a review of SPH methods, see [Lucy \(1977\)](#); [Gingold & Monaghan \(1977\)](#); [Monaghan \(1992\)](#); [Springel \(2010\)](#). Some SPH codes that are currently used in studying CEE include GADGET ([Springel et al., 2001](#)), StarSmasher ([Gaburov et al., 2010](#)), StarCrash ([Rasio & Livio, 1996](#)), Phantom ([Price et al., 2018](#)), MAGMA ([Rosswog & Price, 2007](#)), Vine ([Wetzstein](#)

et al., 2009), SNSPH (Fryer et al., 2006)

By construction, the SPH method has excellent conservation properties. Mass, energy, linear momentum, and angular momentum are all simultaneously conserved. Due to its completely mesh-free construction and Lagrangian nature, local properties follow the properties of mass flow in that region a property that is useful in studying density contrasts such as complex boundary dynamics. By representing the fluid as a collection of particles, SPH inherently adapts to varying resolutions in space based on fluid density.

Despite its many advantages, SPH also has several limitations that need to be considered. SPH simulations can be computationally expensive, particularly for large-scale problems, due to the need to calculate interactions between each pair of particles. Due to the smoothing nature, when simulating phenomena with sharp changes in velocity or density, such as shock waves, the standard SPH formulation may lead to numerical errors. To overcome this, most implementations of SPH use artificial viscosity to model shocks. However, this can introduce some errors as well as the artificial viscosity may overestimate the amount of friction in the flow.

5.3.3 Eulerian Grid Codes

While Lagrangian methods followed the evolution and motion of particles to define the fluid, in Eulerian grid codes, the space is discretized into a finite number of static points to sample the fluid field. By construction, this allows the application of finite-volume methods to solve the Euler Equations which are superior at modeling shocks and other discontinuities. This is because the the structured approach allows for efficient computation of fluxes across the finite volume cell boundaries, crucial for accurately conserving mass, momentum, and energy, and resolving abrupt changes typical of shocks. Some examples of the codes using Eulerian grid methods are FLASH (Fryxell et al., 2000), RAM-

SES (Teyssier, 2002), HARM (Gammie et al., 2003), Athena (Stone et al., 2008), Enzo (Bryan et al., 2014) and, AstroBEAR (Cunningham et al., 2009).

Eulerian grid methods offer several advantages in simulating fluid dynamics, particularly for low-mass flows and scenarios such as winds, mass streams in accreting binaries, and low-density cavities formed during CEE. The presence of a mesh allows the application of finite-volume methods, which are suitable for modeling shocks and other discontinuities by solving the Euler equations. Many grid-based codes incorporate Adaptive Mesh Refinement (AMR), allowing for enhanced and customizable resolution where needed. This adaptive capability provides better spatial fidelity, enabling the simulation to focus computational resources on regions of interest while conserving resources elsewhere.

Eulerian grid methods come with drawbacks too. Static grids define preferred directions, e.g., axes, which break isotropy of space and, thus, lead to imperfect conservation of angular momentum. Static grids lack Galilean invariance, meaning that the simulation's results may be influenced by the choice of reference frame. Furthermore, even with adaptive mesh refinement, grid-based solvers encounter difficulty with highly refined regions that move with large velocities relative to the mesh.

5.3.4 Arbitrary Lagrangian-Eulerian Schemes

In recent decades, a new method has been developed combining the Lagrangian-based methods with the Grid-based method called Arbitrary Lagrangian-Eulerian Schemes (ALE). Like in a grid-based scheme, the space is discretized into the mesh in ALE, but these meshes can flow and deform like in the Lagrangian scheme (For review, see Donea et al. (2004)). By combining Lagrangian and Eulerian features, the ALE method offers several advantages. Since the mesh moves along with the fluid, ALE schemes inherit certain ad-

vantages such as Galilean invariance, and automatic resolution adjustment enabling the grid to adapt dynamically to the evolving flow features. It provides better resolution and accuracy compared to purely Lagrangian methods, especially in scenarios with complex or highly dynamic fluid behavior. Additionally, the ALE method retains the computational efficiency of Eulerian methods by allowing the grid to remain stationary in regions where fluid motion is relatively steady, reducing computational costs compared to fully Lagrangian simulations.

The AREPO code ([Springel, 2010](#)) is an example of a Moving Mesh (MM) code that was first used for CEE simulation in [Ohlmann et al. \(2016\)](#). This method has also led to the development of multiple other codes including TESS ([Duffell & MacFadyen, 2011](#)), FVMHD3D ([Gaburov et al., 2012](#)) and, RICH ([Yalinewich et al., 2015](#)). [Prust & Chang \(2019\)](#) has used an independently developed MM code MANGA ([Chang et al., 2017](#)) to preform CEE simulation.

5.3.4.1 MANGA

MANGA ([Chang et al., 2017](#)) is a moving-mesh (MM) hydrodynamic solver for the N-body simulation code CHANGA (Charm N-body GrAvity solver) ([Jetley et al. \(2008, 2010\); Menon et al. \(2015\)](#)). MANGA used Voronoi tessellation to construct the cells in the moving mesh. A mesh generating point and its boundary are defined as a Voronoi cell where every point in this cell is closer to its mesh generating point than the neighboring mesh generating points ([Okabe et al., 1992](#)). MANGA uses VORO++ library ([Rycroft, 2009](#)) to construct Voronoi cells. Refer to [Chang et al. \(2017\); Prust & Chang \(2019\)](#) for a detailed description of the MANGA algorithm.

5.4 CEE: AN EXTRAORDINARY PHYSICS PROBLEM

The physics and astrophysics of CEE systems have been a subject of continuous study for the last 50 yr. Despite the importance of CEE, many fundamental questions about its physics are still unanswered. The complex physics of this process, which includes gravity, hydrodynamics, nuclear burning, recombination, and radiation, has precluded much analytic and computational progress in modeling CEE. Additionally, the short period of a CE phase in comparison to the stellar lifetime makes CEE observations difficult. So, most of our understanding of CEE comes from evolutionary necessity. However, some observations are attributed to CEE as described in Section 5.2. There are also advancements in the computational techniques used in simulating CEE, which are explained in Section 5.3.

In the last decade, advances in computing and algorithms have made high-resolution, long-timescale simulations of CEE possible. Being able to simulate a CEE through its different phases within a reasonable computing time is extremely useful as it helps to unravel many relevant physics of CEE. One longstanding question about CEE is the time scale and the efficiency of envelope ejection. Once a binary enters a CE phase, when it leads to a merger and when it leads to an envelope ejection is still unclear to us from our theoretical understanding. Some three-dimensional numerical computations of CEE have found a wide variance in the ejection efficiency of the envelope. Early studies with 3D hydro-dynamical simulations show 10 to 80 percent efficiency in envelope ejections (e.g. [de Kool \(1987\)](#); [Rasio & Livio \(1996\)](#); [Livio & Soker \(1988\)](#); [Terman et al. \(1994, 1995\)](#); [Sandquist et al. \(1998, 2000\)](#)). However, the resolution of these studies is poor. Some recent work also shows a variance between 5 to 100 percent in efficiency (e.g. [Passy et al. \(2012\)](#); [Ricker & Taam \(2012\)](#); [Nandez et al. \(2015\)](#); [Ohlmann et al. \(2016\)](#)). One should note that some of this variance is due to the difference in the binary system studied in these works. Following the work in [Prust & Chang \(2019\)](#); [Prust \(2020\)](#), where authors

used MANGA to simulate and study CEE, I have used MANGA to simulate a CEE with some improvements in the initial condition to achieve speed-ups in the simulation. With these speedup improvements, we conduct a long timescale (5000d) 3D simulation of a CEE event with a red giant and a main-sequence companion to study the time scale and efficiency of envelope ejection in these systems. I will also discuss and compare results from some of the recent works addressing the same question. This work is discussed in detail in Chapter 6.

While there are some observations of transients attributed to CEE as described in Section 5.2, there aren't many works that use simulations to compute the expected observations appearances such as the luminosity evolution of a CEE, and compare that with transient observations. One reason for the absence of such work is due to the complication of including radiation in the current 3D hydro-dynamics codes. However, radiation transfer codes are used in computing the light curve and spectra of other astrophysics events such as supernovae explosions under the assumption that these explosions are spherically symmetric. This is possible because the code can work in 1D instead of 3D due to spherical symmetry. In Chapter 6, I show that the envelope in a CEE eventually becomes spherical and homologous. This implies that the radiation transfer codes that are used to calculate supernova light curves and spectra can be adapted to compute light curves and spectra from CEE events.

CHAPTER 6

Envelope Ejection and Homologous Expansion

*This chapter is reproduced from [Valsan et al. \(2023\)](#), which is published in *Monthly Notices of the Royal Astronomical Society*, Volume 526, Issue 4 under the title "Envelope ejection and the transition to homologous expansion in common-envelope events".*

In the last decade, advances in computing and algorithms have made high-resolution, long-timescale simulations of CEE possible. These long-timescale simulations have begun to unravel the relevant physics of CEE and its astrophysical impact. In particular, studies carried out by several groups on low-mass binaries such as an asymptotic giant branch (AGB) primary with a main-sequence (MS) companion star ([Sand et al., 2020](#); [Chamandy et al., 2020](#); [Ondratschek et al., 2022](#)) and a red-giant branch (RGB) primary with an MS star ([Iaconi et al., 2019](#)) have demonstrated that the envelope is completely ejected on sufficiently long timescales (years to decades). These groups differ in their conclusions of what physics is important. For instance, [Iaconi et al. \(2019\)](#), [Sand et al. \(2020\)](#), and [Ondratschek et al. \(2022\)](#) argue that recombination energy is crucial in envelope ejection, but [Chamandy et al. \(2020\)](#) argue otherwise. This difference is likely due to the limited number of cases studied and future studies will likely bring this physics into sharper focus.

In addition, recent work by [Iaconi et al. \(2019\)](#) argues that the expansion of the envelope leads to homologous expansion on long timescales. This should not come as a surprise because any expansion leads to homologous expansion so long as the trajectories remain ballistic. However, if the envelope expands homologously, this helps to simplify the theory of CEE and would provide an easier means to compute observables.

Recent observations have also hinted at the presence of homologously expanding ejecta in CEE and stellar merger events. For instance, the properties of observed CO emission in V4332 Sgr is well reproduced with the homologous expansion model (Kamiński et al., 2018). Additionally, Kamiński et al. (2020) showed that the observed properties of the molecular remnant of Nova 1670 (CK Vulpeculae) are satisfactorily reproduced by linear velocity fields.

In this paper, we study the physics of the ejection of the envelope using long-timescale simulations. Starting with recent work in Prust & Chang (2019); Prust (2020), we optimize our numerical techniques to allow for an order of magnitude increase in integration time. We show that for the case of a $2 M_{\odot}$ RGB and a $1 M_{\odot}$ MS companion, we achieve complete envelope ejection in 1500 d. We also show that the envelope enters a homologous phase early on (about 550 d) and that the morphology of the ejected material is roughly spherical.

6.1 NUMERICAL SETUP

We use the moving-mesh hydrodynamic solver for CHANGA, which we call MANGA (Chang et al., 2017; Prust & Chang, 2019), to study CEE. MANGA is a moving-mesh hydrodynamic simulation code based on the algorithms described by Springel (2010). A detailed description of MANGA is presented by Chang et al. (2017). Improvements such as the multiple time-stepping algorithms and integration of stellar equations of state are presented by Prust & Chang (2019). A discussion of its use for simulations of main sequence tidal disruption events is presented by Spaulding & Chang (2021). Finally, recent code improvements are discussed by Chang et al. (2020) for radiation hydrodynamics, Chang & Etienne (2020) for general relativistic hydrodynamics, Prust (2020) for moving-boundary conditions, and Prust & Chang (in preparation) for magnetohydrodynamics.

We refer the interested reader to this literature for a detailed description of MANGA.

6.1.1 Initial Conditions

We use the same procedure as [Prust & Chang \(2019\)](#) to construct initial conditions. We evolve a $2 M_{\odot}$ star with MESA ([Paxton et al., 2011, 2013, 2015, 2018, 2019](#); [Jermyn et al., 2023](#)) from the pre-main sequence to the red giant phase and stop when it reaches a radius of around $52 R_{\odot}$. As done by [Prust & Chang \(2019\)](#), we construct a star of mass $2 M_{\odot}$, whose entropy profile matches that of the original star. The core of the newly constructed star is modeled as a dark matter particle with gravitational softening for computational expediency. We then map the radial profile of density and temperature to an unstructured particle (mesh-generating point) mesh. The simulation consists of 430K mesh-generating points, of which 80K model the star. The companion star, which is also modeled as a softened dark matter particle, is then placed at the surface of the red giant.

We should note that placing the companion on the surface of the red giant as an initial condition is unrealistic for a couple of reasons. First, the red giant model used at the beginning of the simulation is only in hydrostatic equilibrium in isolation and thus does not account for the effects of the companion. Second, a more realistic scenario would involve the binary system evolving, allowing the red giant to slowly expand on a nuclear timescale until it fills its Roche lobe. At this point, it undergoes unstable mass transfer, driving the system into CEE. However, this more realistic scenario is not easily realizable in numerical simulation as it involves the slow evolution of the red giant in the thermal timescale and would demand a realistic treatment of nuclear burning and radiation. The computational costs of such a simulation would be prohibitive. Thus, we have simplified the initial conditions to the ones stated and anticipate that for the long-term evolution of the CEE event, the initial conditions do not play a large role.

In this paper, we have made a number of modifications in an effort to reduce the computational cost. First, we use an adiabatic equation of state ($\gamma = 5/3$) instead of a MESA equation of state. The simulation using the MESA equation of state is significantly more computationally expensive than the adiabatic case. The primary advantage of using the MESA equation of state is that it encodes additional information in regard to recombination energy, which may be important in ejecting the envelope for low-mass systems. Nevertheless, as we will demonstrate below, orbital energy alone achieves complete envelope ejection without the need for recombination energy. We also improved the grid generation for the tenuous atmosphere surrounding the stars. In particular, we increase the spacing between grid points exponentially outside the stars up to the final coarsest resolution instead of the power-law increase used previously by [Prust & Chang \(2019\)](#). This reduces the number of nearest-neighbor searches for mesh-generating points near the boundary of the star and atmosphere. We find that this improves the performance of the code by around a factor of 2.

These reductions in computational costs and improved computing power allow us to run our simulation for 5000 d, which is longer than our previous simulations ([Prust & Chang, 2019](#)) by a factor of around 20. It is also in line with other recent long-timescale simulations ([Iaconi et al., 2019](#); [Sand et al., 2020](#)).

6.2 RESULTS

We show a series of projected density plots in Figure 6.1, projected along the axis of the orbital plane (z-axis, right column) and projected along a direction in the orbital plane (x-axis, left column) at 503 d, 1006 d and 2013 d. The '+' sign marks the center of mass of the system. Initially, these projections demonstrate that the ejected matter is axisymmetric, but not spherical. The overall shape remains fairly constant, though it does become

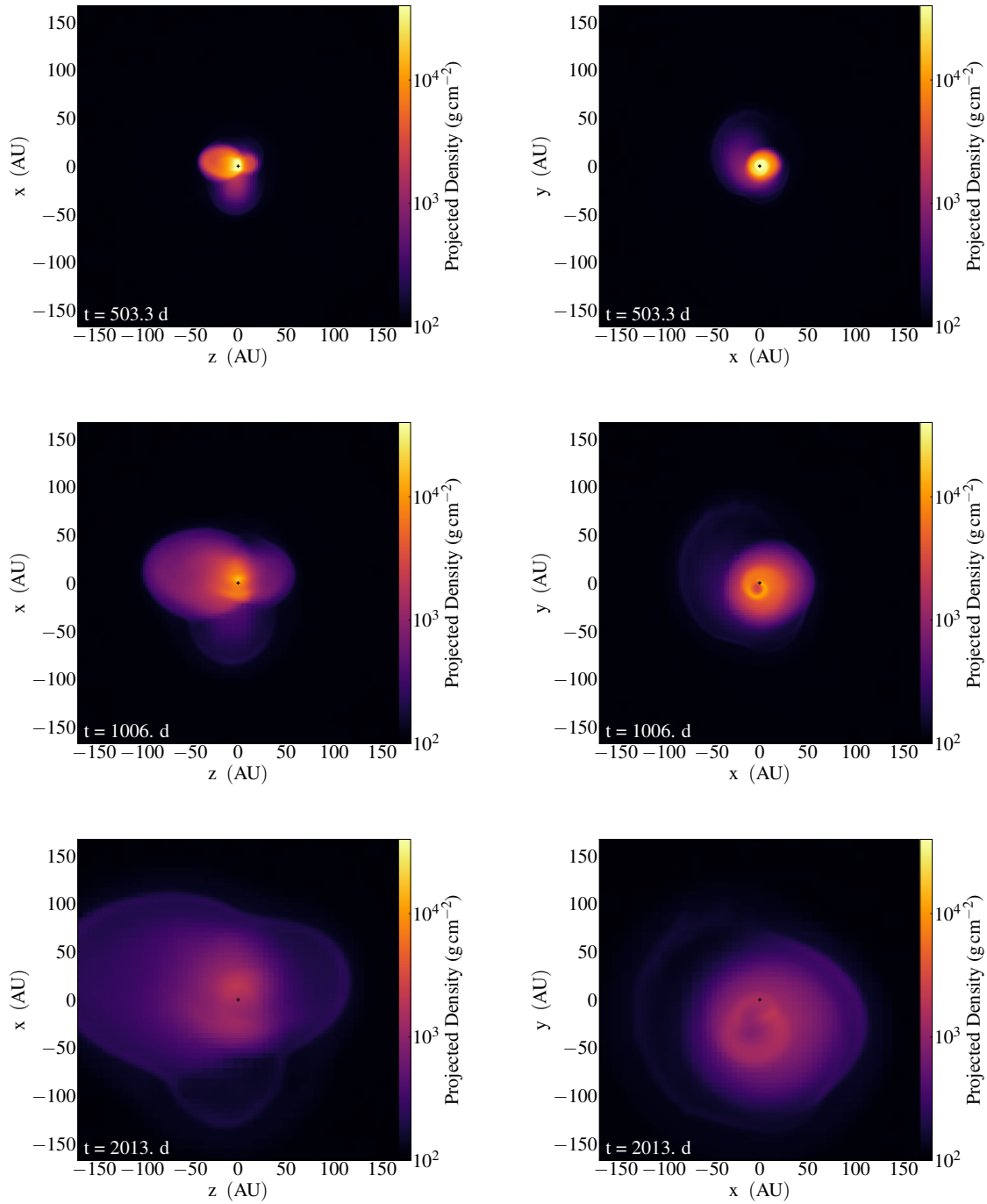


Figure 6.1: Projection of density on to the $x - z$ plane (left panel) and $x - y$ plane (right panel) at different time slices (503 d, 1006 d, 2013 d) from the simulation. The '+' sign marks the center of mass of the system.

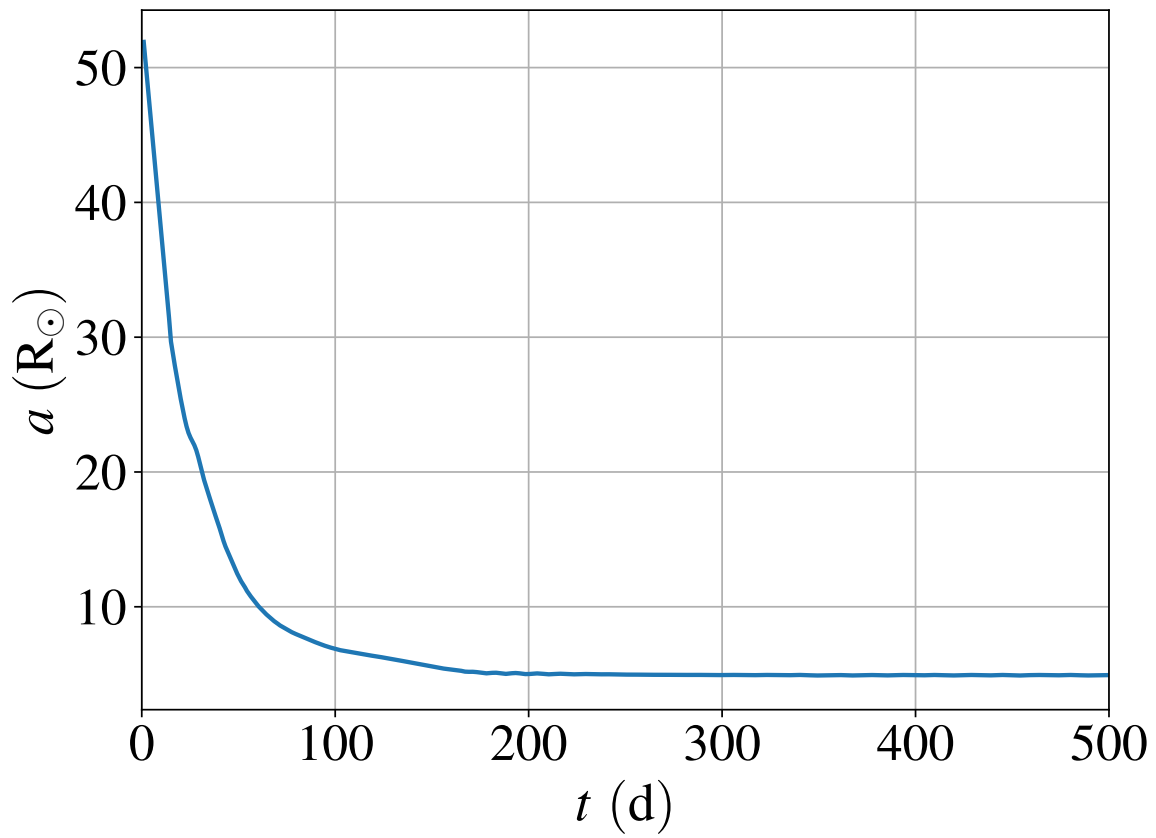


Figure 6.2: Smoothed separation between the center of mass of the red giant and the main-sequence star as a function of t . There is an initial rapid plunge of the two centers toward each other, but this plateaus to about $5 R_{\odot}$ after 200 d.

more spherical as it evolves. This constancy of the overall shape and evolution to greater spherical symmetry will be important in our discussion of homologous expansion and the spherical approximation.

In Figure 6.2, we plot the orbital separation, a , between the centers of the stars. Each a in the plot is taken to be the average of a in a time interval of 14 d. In the beginning, the two centers plunge toward one another in a period of rapid orbital decay. This starts to slow down and at 200 d, the orbital decay plateaus to an orbital separation of $a \approx 5 R_{\odot}$, which is similar to our previous result of $a \approx 3.6 R_{\odot}$ (Prust & Chang, 2019).

For each i -th particle/mesh-generating point in the system, the total mechanical energy is defined as

$$E_{\text{mech},i} = m_i \left(\frac{1}{2} v_i^2 + \phi_i \right), \quad (6.1)$$

where m_i is the total mass of the mesh-generating point, v_i is the fluid velocity of the mesh-generating point relative to the bound center of mass of the system, and ϕ_i is the gravitational potential. Particles with $E_{\text{mech},i} < 0$ are bound to the binary while those with $E_{\text{mech},i} > 0$ are unbound. As discussed by Prust & Chang (2019), we must carefully define the velocities relative to that of the center of mass of the bound material. This involves an iterative computation to find the bound mass and the center of mass velocity. The unbound mass fraction is then defined as the fractional mass of the material with positive total energy.

In Figure 6.3 we plot the unbound mass fraction, f_{unb} , as a function of time. Nearly all gas from the red giant is unbound after 1500 d and over 80 percent at 400 d. At 250 d, the fraction of mass that is unbound compared to our previous result (Prust & Chang, 2019) is substantially larger (40 percent vs. 10 percent), considering just the mechanical energy. However, the equation of state is different between the two simulations (ideal

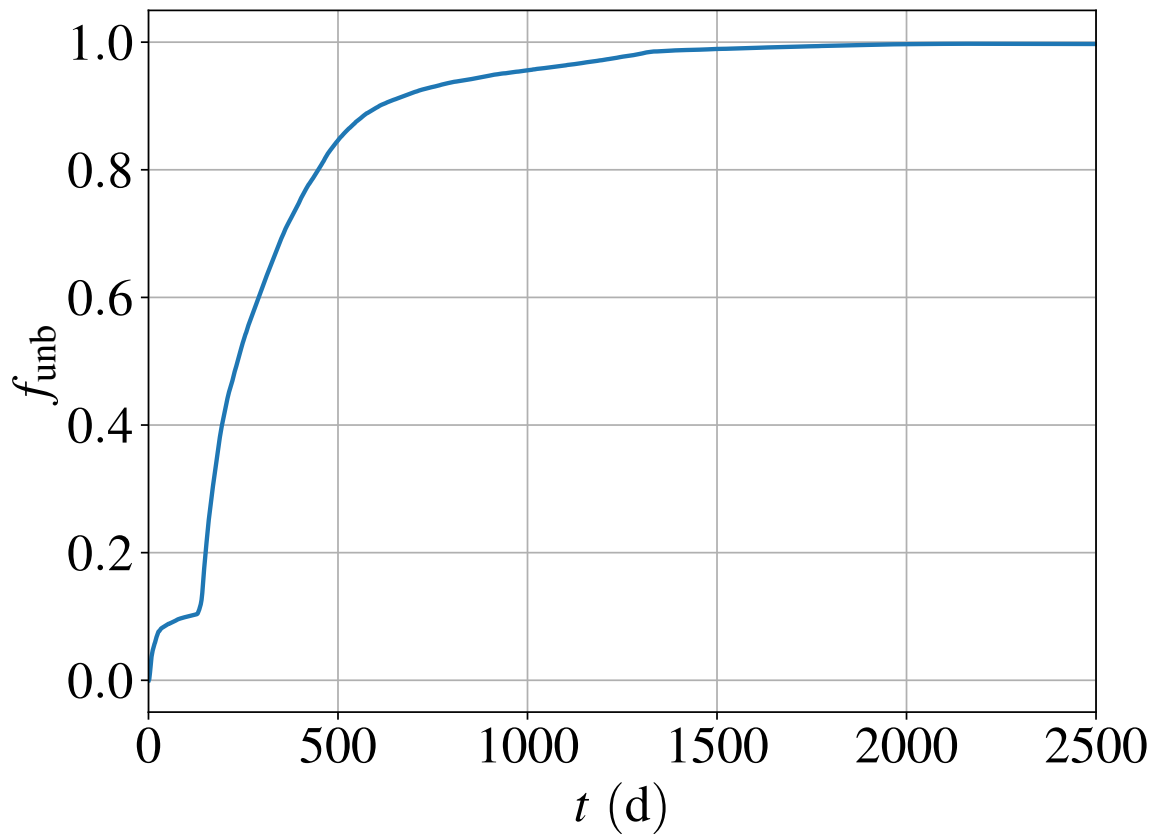


Figure 6.3: Fraction of unbound mass, f_{unb} , as a function of time, t . We only consider the mechanical energy in this case.

gas vs MESA). In addition, envelope ejection occurs in the absence of additional late-time energy injection via hydrogen recombination and/or jets. Other work has also recently demonstrated complete envelope ejection on a time scale of about 1000 d, but these results can rely on additional late-time energy injection.

6.2.1 Homologous Expansion

Recently, [Iaconi et al. \(2019\)](#) showed in their long-timescale CEE simulations that the envelope ejection follows a homologous expansion approximation. In their work, they simulate the evolution of a $0.88 M_{\odot}$, $83 R_{\odot}$ RGB and a $0.6 M_{\odot}$ companion star and follow the system for about 15 yr. They show that the external layers of the envelope become homologous as soon as they are ejected, but that it takes about 14 yr for the bulk of the unbound gas to enter homologous expansion. Motivated by this result, we investigate the onset of homologous expansion in our simulations.

To begin, we recall that the distinguishing characteristic of homologous expansion is that the velocity follows a radial profile $v \propto r$. In essence, this means that fluid elements are on ballistic trajectories with little or no interaction between fluid elements or external forces. As such, the radial position of a fluid element can then be written as

$$r(t) = v_r t_h, \tag{6.2}$$

where v_r is the radial velocity of the fluid element and t_h is the homologous expansion time. We note that while the formalism of homologous expansion is relatively simple and discussed widely in the literature, we discuss it here again to define it in terms of computational quantities like time, which is defined as zero at the beginning of a simulation and has no relation to the zero time in homologous expansion. Thus, we define $t_h = t - t_0$, where t is the time since the start of the simulation and t_0 is some fitted time that defines

the $t = 0$ point of homologous expansion. Indeed, t_h is mapped exactly to the time in most discussions of homologous expansion. We can rewrite equation (6.2) as

$$v_r = \frac{r}{t - t_0} = \frac{r}{t_h}, \quad (6.3)$$

and by differentiating and integrating the above equation, we can write the position of a fluid particle at time t with respect to an initial time t_i as

$$r(t) = r_i \frac{t - t_0}{t_i - t_0} = r_i \frac{t_h}{t_{h,i}}, \quad (6.4)$$

where r_i is the radial position at a time $t_i > t_0$. From equation (6.4), we now define a scaled radius with respect to the initial time given the current radius for any fluid element in the simulation

$$r_s(r, t) = r \frac{t_{h,i}}{t_h} = r \frac{t_i - t_0}{t - t_0}. \quad (6.5)$$

In other words, r_s maps the position of a fluid element, r , at a particular time t to the position of a fluid element at the initial time t_i . Having defined the scaled radius, r_s , we also define the scaled density and velocity as

$$\rho_s(r, t) = \rho_i(r_s(r, t)) \left(\frac{t_h}{t_{h,i}} \right)^3 \quad (6.6)$$

$$v_{r,s}(r, t) = v_{r,i}(r_s(r, t)). \quad (6.7)$$

The simple rescaling given in equations (6.6) and (6.7) is insufficient to describe the entire system. While it works for the expanding envelope, it does not describe the tenuous atmosphere. Toward that end, we define the radius of the envelope, $R(t)$, which is the position of the outer boundary of the homologously expanding region inside which

equations (6.5), (6.6) and (6.7) are valid. We define a dimensionless radius η as

$$\eta = \frac{r}{R}, \quad (6.8)$$

so that $\eta = 0$ at the centre of the CE and $\eta = 1$ at the envelope's outer boundary. From equation (6.4), we can estimate R for any given time with respect to the initial time t_i : $R = R_i(t_h/t_{h,i})$. We can then redefine scaled density, ρ_s , and scaled velocity, $v_{r,s}$, for regions inside and outside of the envelope. This gives

$$\begin{aligned} \rho_s &= \begin{cases} \rho_i(r_s(r, t)) \left(\frac{t_h}{t_{h,i}}\right)^3 & \text{if } \eta \leq 1 \\ \rho_b & \text{if } \eta > 1 \end{cases} \\ v_{r,s} &= \begin{cases} v_{r,i}(r_s(r, t)) & \text{if } \eta \leq 1 \\ 0 & \text{if } \eta > 1 \end{cases} \end{aligned} \quad (6.9)$$

To show that our simulations follow the scaling defined by equations (6.5) and (6.9), we select $t_i \approx 800$ d and fit $t_0 \approx 550$ d so that the re-scaled radial velocities $v_{r,s}$ match one another between a few $\times 10^2 R_\odot$ and a few $\times 10^3 R_\odot$. We show this result in the top plot of Figure 6.4. As this plot shows, the velocities for $r_s > \text{a few } \times 10^2 R_\odot$ match each other for a number of different time steps. We also fit a power law between $6 \times 10^2 R_\odot$ and $5 \times 10^3 R_\odot$, and the resulting fit is

$$v_r = 4.8 \left(\frac{r_s}{100 R_\odot} \right)^{0.86} \text{ km s}^{-1}. \quad (6.10)$$

The radial power law exponent is about 1, which is consistent with homologous expansion. Thus we find that by 2000 d since the start of the simulation, homologous expansion is definitively reached.

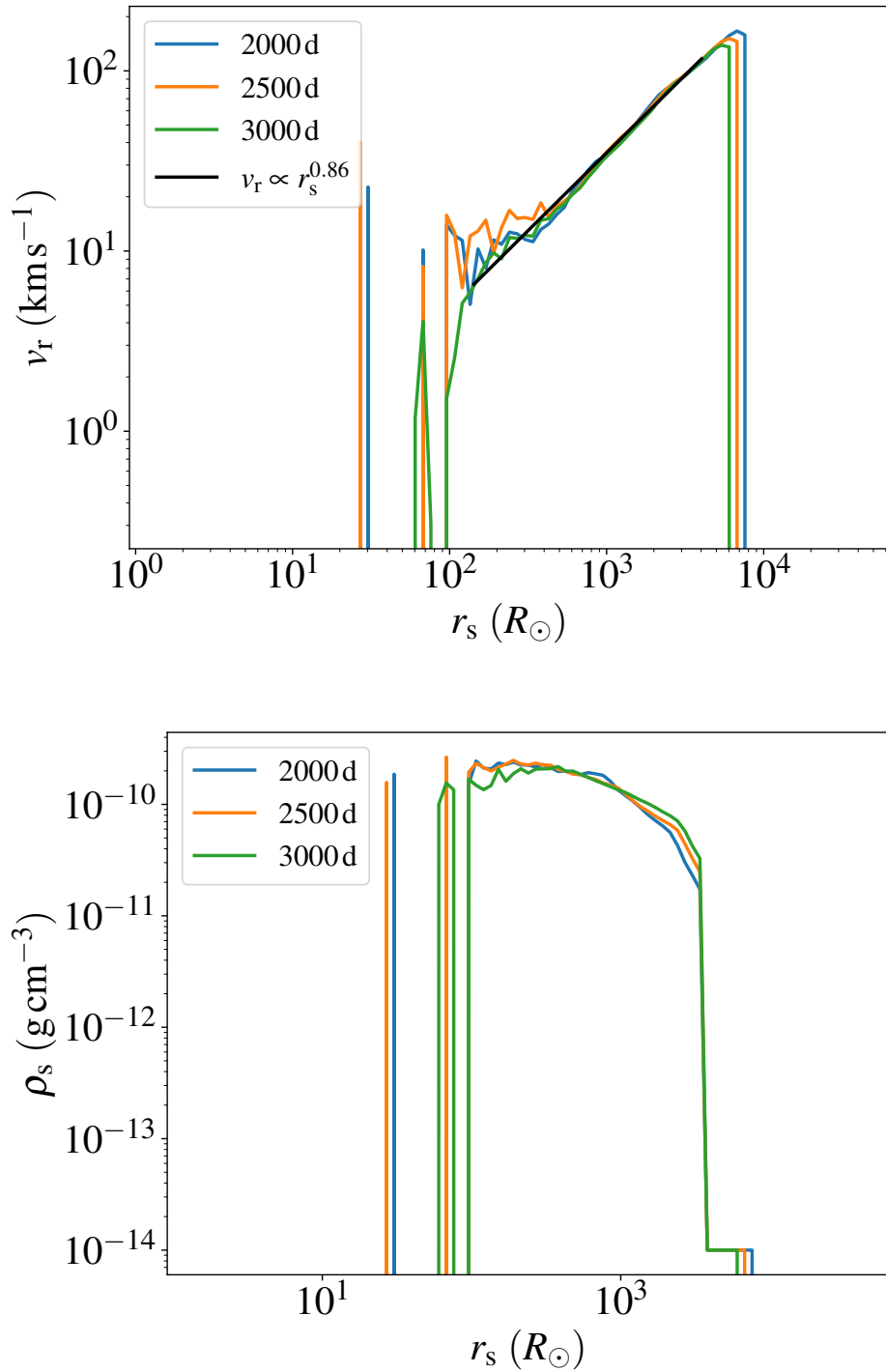


Figure 6.4: Radial velocity (top) and scaled density (bottom) as a function of scaled radius for different times (2000 d, 2500 d and 3000 d). We also show a power-law fit (solid black line) for $v_r \propto r_s^{0.86}$ (top).

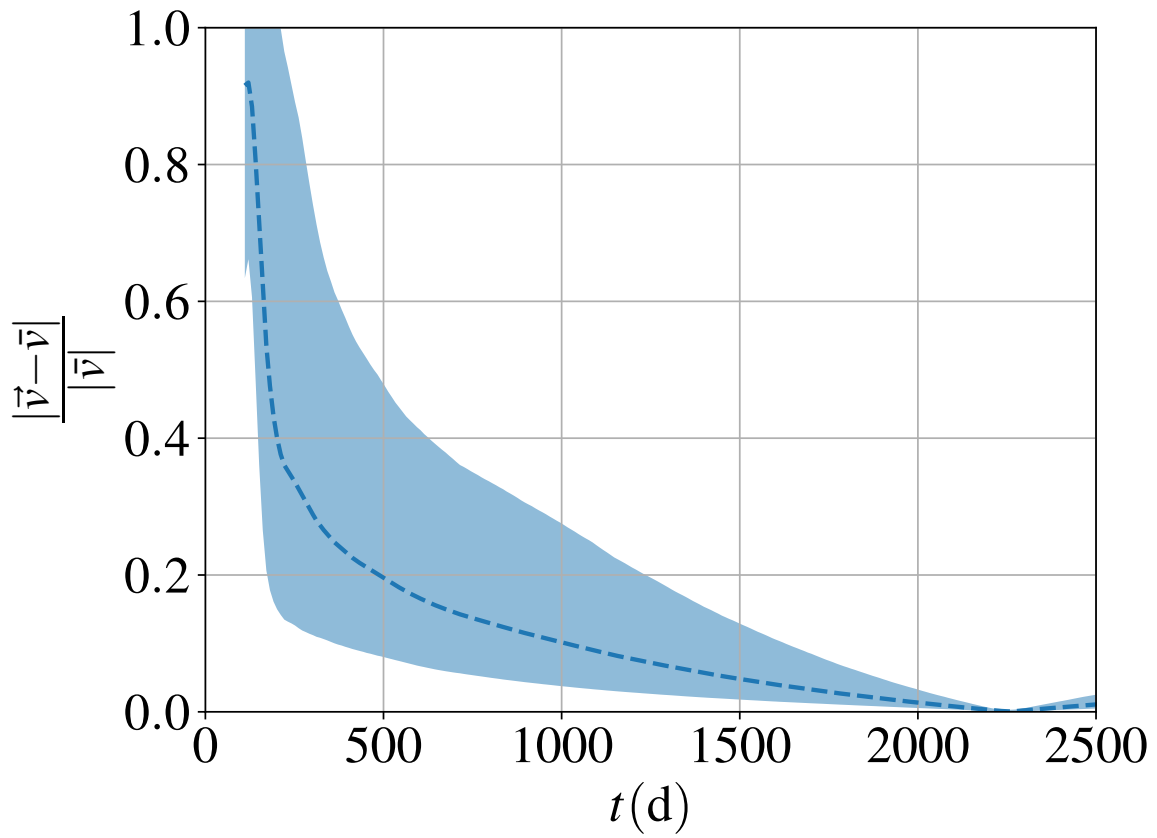


Figure 6.5: The fractional change in the velocity of all particles compared to the final average velocity as a function of time. The dashed line represents the mean and the shaded area represents the standard deviation of the fractional change in the particle velocity.

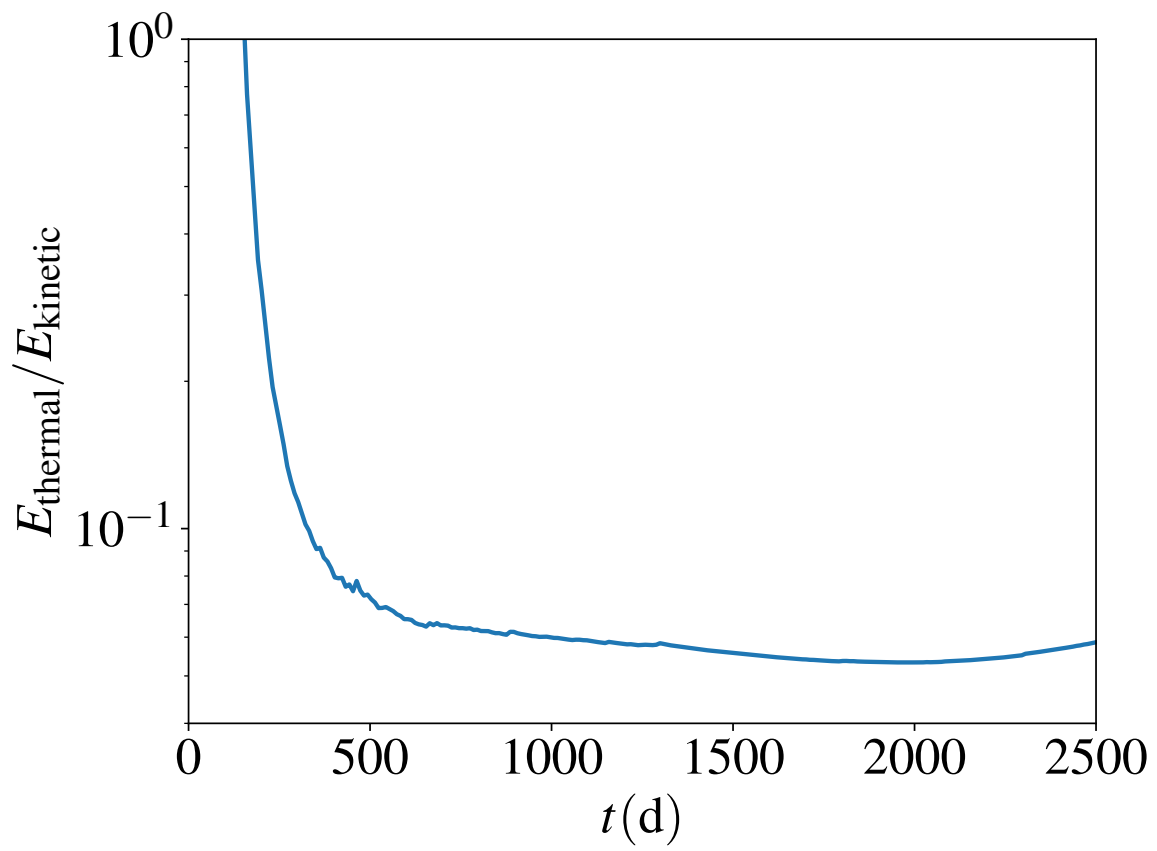


Figure 6.6: Ratio of thermal energy to kinetic energy as a function of time.

We also plot the scaled density ρ_s in the bottom plot of Figure 6.4. Similar to the behavior of v_r , we observe that the ρ_s match one another for a few different epochs when rescaled by r_s . This is expected in the case of homologous expansion when the (scaled) density structure is frozen.

In Figure 6.5, we show the fractional change in the absolute 3-D velocity of all fluid elements relative to their asymptotic (late-time) velocities approach zero as the envelope evolves. The fractional change is computed based on the late-time velocity of each fluid element, defined as the average of the velocity between 2000 d to 2500 d. The dotted line in Figure 6.5 represents the mean of the fractional change in the particle velocity. The shaded region represents the standard deviation from the mean. Thus, the velocities of fluid elements do not change by more than 5 percent either in the magnitude or direction after about 1500 d on average. This implies that the fluid elements are on ballistic trajectories.

In addition, we plot the ratio of total thermal energy in the system to the total kinetic energy as a function of time in Figure 6.6. The thermal energy is smaller than 5 percent of the kinetic energy after 500 d. The fact that this thermal energy does not continue to drop due to adiabatic expansion is because we use a temperature floor in our simulations to maintain numerical stability. In any case, thermal energy is a negligible fraction of the energy budget of the system.

Finally, for a homologously expanding system under adiabatic conditions, the average density scales like

$$\bar{\rho} \propto t_h^{-3}. \quad (6.11)$$

This has also been previously demonstrated numerically by [Iaconi et al. \(2019\)](#) for their SPH simulations. Here we confirm the same result by plotting the average density of unbound particles (solid line) in the envelope as a function of t in Figure 6.7. We also plot

a t^{-3} power law fit (dashed line) that is fitted for $t \in [500, 2000]$ d. The average density from our simulation follows the t^{-3} power law.

6.2.2 1-D Model

Motivated by the results of the previous section, we now study a simplified 1-D spherically symmetric model of the ejected envelope. We have developed a 1-D finite-volume spherically symmetric hydrodynamics code in Python that uses an HLLC Riemann solver (Harten et al., 1983; Einfeldt, 1988) with piecewise-constant (first-order) reconstruction to study this ejected envelope¹. Our models consist of 350 grid points that are logarithmically spaced, starting from $r = 3 R_{\odot}$ to $r = 3 \times 10^7 R_{\odot}$, giving 50 grid points per decade. We set the origin to the center of mass of the binary and use free (von Neumann) boundary conditions on the inner and outer boundaries.

Rewriting the Euler equation (Equation 5.8) in 1-D,

$$\frac{\partial \mathbf{U}}{\partial t} + \frac{1}{r^2} \cdot \frac{\partial \mathcal{F}}{\partial r} = \mathcal{S}, \quad (6.12)$$

where $\mathbf{U} = (\rho, \rho v_r, \rho e)$ is the state vector, $\mathcal{F} = (r^2 \rho v_r, r^2(\rho v_r v_r + P), r^2(\rho e + P)v_r)$ is the flux function, $\mathcal{S} = (0, -\rho \frac{GM_r}{r^2}, -\rho v_r \frac{GM_r}{r^2} + \mathcal{S}_h)$ is the source function, e is the specific energy, G is the gravitational constant, and M_r accounts for the mass of the central binary and the envelope enclosed within radius r . The extra term, \mathcal{S}_h , is added to study the effect of the heating supplied to the envelope from the central binary. We discuss this below. For the initial conditions of the 1-D model, we take the fitted results from the 3-D numerical simulation at $t = 800$ d.

The 1-D model computes 1000 outputs over 100 yr, each one separated by 0.1 yr. We present the results in Figs. 6.8 and 6.9 for 10, 20, 50, and 100 yr. These times are relative

¹This 1-D code will be shared on reasonable request to the corresponding author.

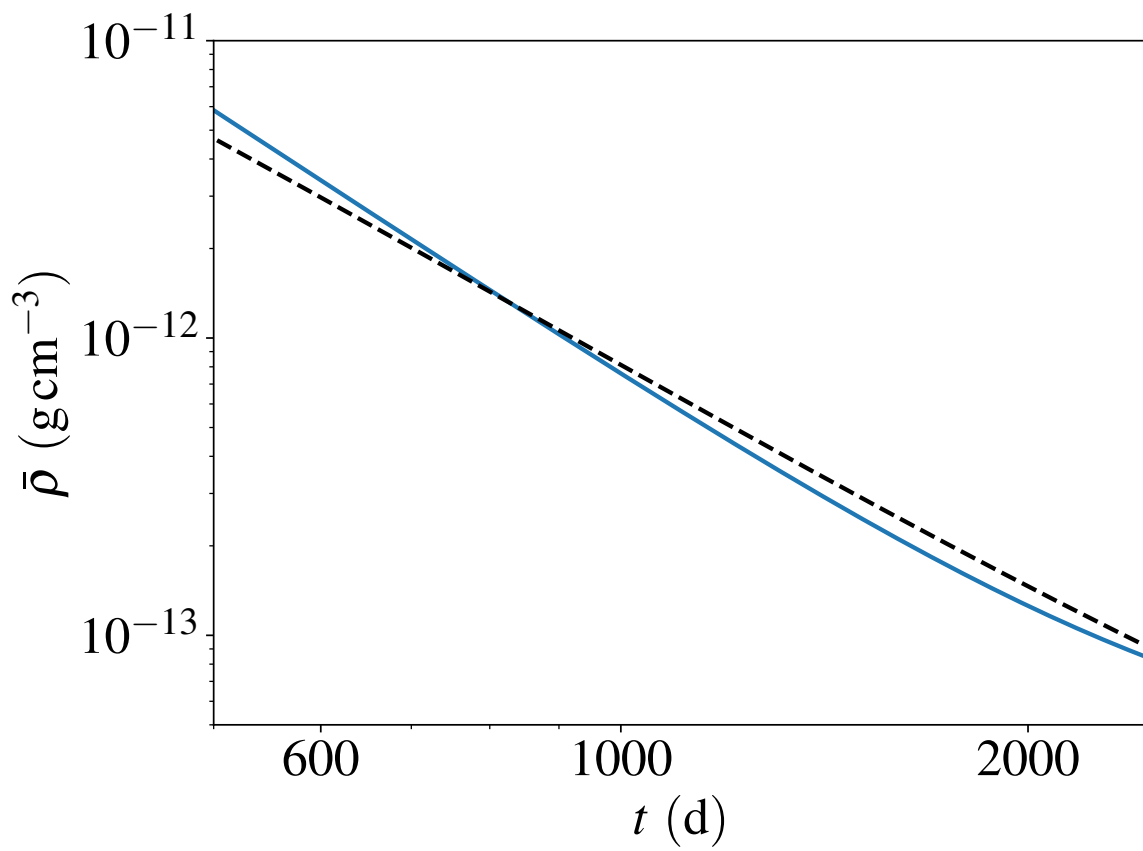


Figure 6.7: Mean density ($\bar{\rho}$) of the envelope as a function of t (blue solid curve). The black dotted curve is the t^{-3} fit and is fitted for $t \in [500, 2000]$ d . Note that the average density profile follows a t^{-3} power-law closely.

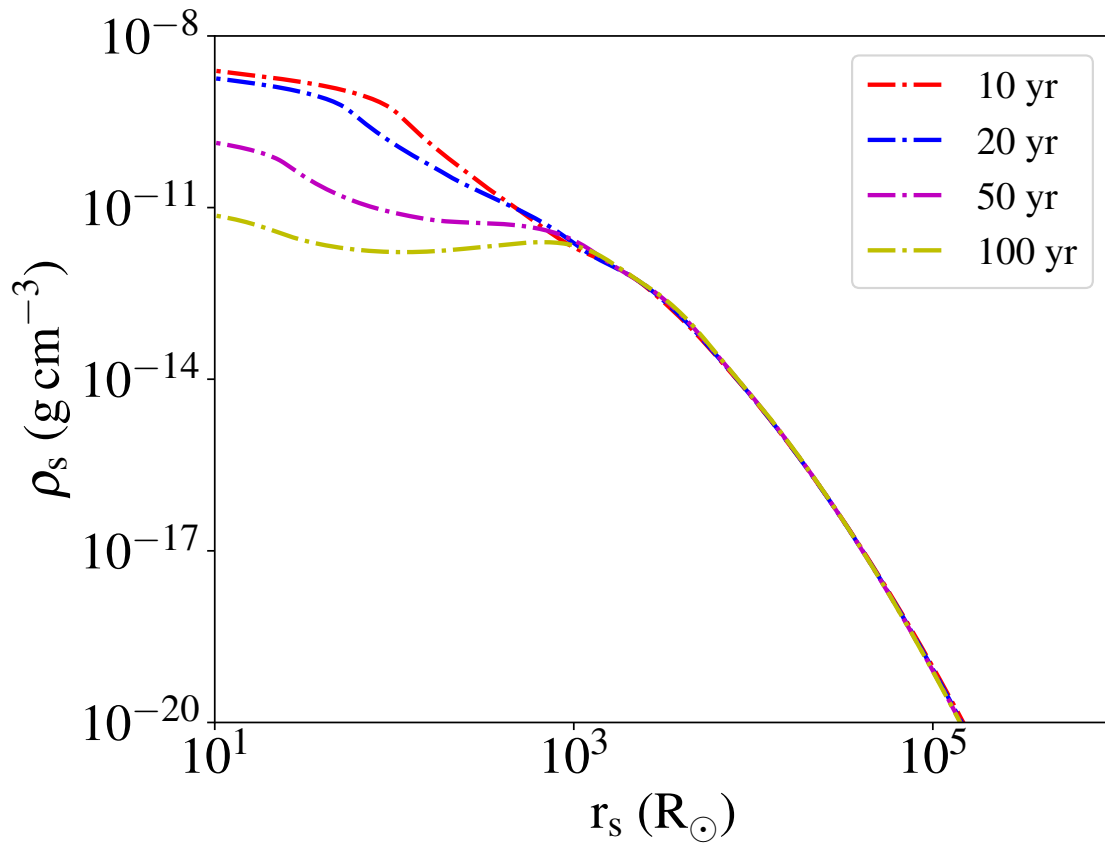


Figure 6.8: Scaled density, ρ_s as a function of scaled radius, r_s from 1-D simulations, for 10 (red), 20 (blue), 50 (magenta), and 100 (yellow) yr and a heating parameter of $\lambda = 1$.

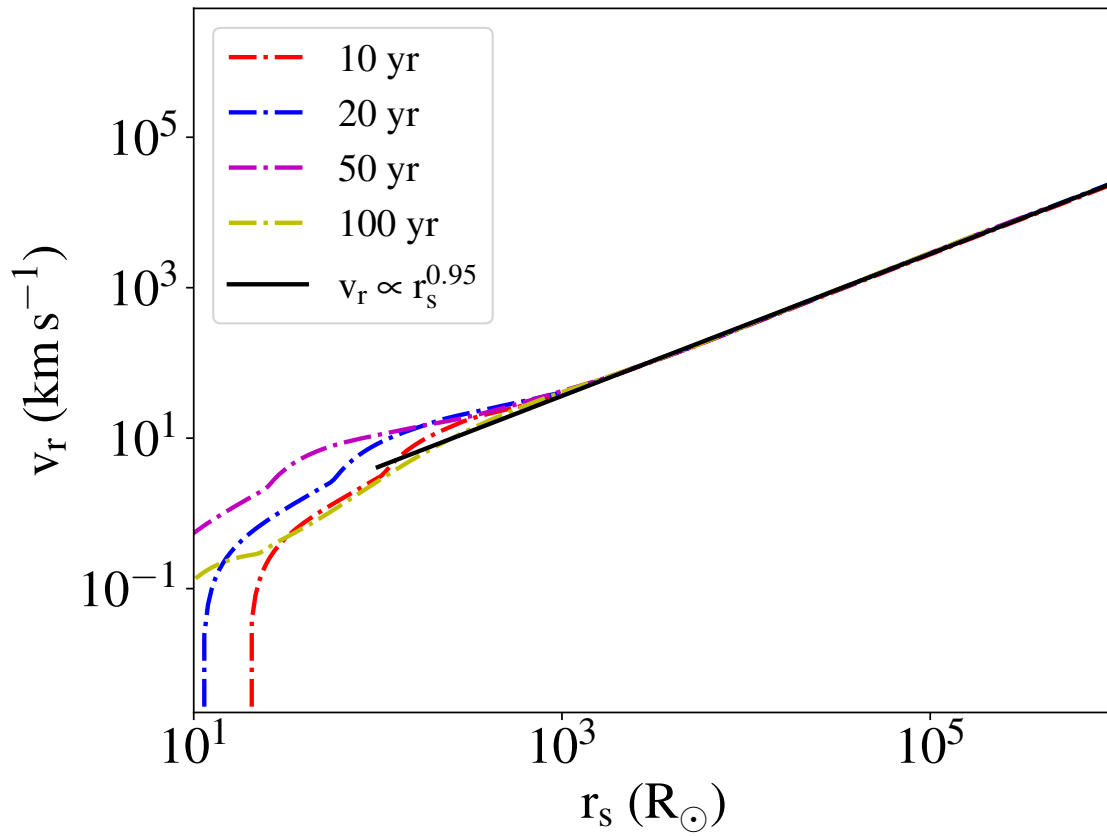


Figure 6.9: Radial velocity, v_r , as a function of scaled radius from 1-D simulations. The times and λ are the same as in Figure 6.8. The solid black line is the best fit of $v_r \propto r_s^{0.95}$.

to the start of the 3-D simulation so that the same time between the two simulations can be directly compared. The scaled radius and density follow equations (6.5) and (6.6), respectively. We calculate the best fit of the linear part to get the power-law relation between v_r and r_s . We fit each time step separately and average them to produce a best fit of $v_r \propto r_s^{0.95}$.

We note that the 1-D model is intentionally not constrained to adhere to the homologous expansion model, though we did use initial conditions that correspond to the beginning of the homologous phase. One feature that is observed in these 1-D models, but not in the full 3-D models, is evident in Figure 6.9. Here at a radius below about a few $\times 10 R_\odot$, the radial velocity becomes negative. This manifests as the vertical rise in Figure 6.9. This is due to the gravitational potential from the inner binary being much larger than the total energy of the envelope in this region. However, these negative radial velocities are not seen in full 3-D models though the data is quite noisy in this region (Figure 6.4).

This difference may be attributed to the periodic forcing of the orbiting binary on the gas in this inner region. To examine this, we develop a simple model of binary heating for this 1-D model.

For a fluid element in a circumbinary orbit around two point masses, we model the periodic forcing from the inner binary as a forced simple harmonic oscillator with a natural resonant frequency of κ , which is the epicyclic frequency. The periodic forcing term has a frequency of $m(\Omega_b - \Omega)$, where m is some natural number, Ω_b is the orbital frequency of the binary and Ω is the orbital frequency of the fluid element.

A general driven damped harmonic oscillator equation is then

$$\frac{d^2 \delta r}{dt^2} + \Gamma \frac{d \delta r}{dt} + \kappa^2 \delta r = f_0 \cos m(\Omega_b - \Omega)t, \quad (6.13)$$

where Γ is a damping term that arises from fluid dissipation and f_0 is the overall forcing amplitude. Letting $\omega = m(\Omega_b - \Omega)$, the complex form of this equation is

$$\frac{d^2\delta r}{dt^2} + \Gamma \frac{d\delta r}{dt} + \kappa^2 \delta r = \frac{F_0}{m} \exp(i\omega t), \quad (6.14)$$

Starting with an ansatz, $\delta = \mathcal{A} \exp i\omega t$, we can show

$$\mathcal{A} = f_0 \frac{\kappa^2 - \omega^2 - i\omega\Gamma}{(\kappa^2 - \omega^2)^2 + (\Gamma\omega)^2}, \quad (6.15)$$

where we can write

$$\mathcal{A} = A \exp i\delta \quad (6.16)$$

where

$$A = \frac{f_0}{\sqrt{(\kappa^2 - \omega^2)^2 + (\Gamma\omega)^2}} \quad (6.17)$$

$$\delta = \tan^{-1} \left(-\frac{\omega\Gamma}{\kappa^2 - \omega^2} \right) \quad (6.18)$$

The specific energy is then

$$\epsilon = \frac{1}{2} \dot{\delta r}^2 + \frac{1}{2} \kappa^2 \delta r^2 \quad (6.19)$$

The maximum amplitude, A , occurs when $\omega = \kappa$ and is:

$$A = \frac{f_0}{\Gamma\kappa}, \quad \text{and} \quad \delta = \frac{\pi}{2}, \quad (6.20)$$

and the maximum specific energy is:

$$\epsilon_{\max} = \frac{1}{2} \frac{(f_0)^2}{\Gamma^2} \quad (6.21)$$

The specific energy dissipation is thus,

$$\dot{\epsilon} = 2\epsilon_{\max}\Gamma = \frac{f_0^2}{\Gamma} \quad (6.22)$$

For our case, we can model the forcing from the inner binary as a tidal forcing

$$f_0 = \beta \frac{GM_{\text{bin}}a_{\text{bin}}}{r^3}, \quad (6.23)$$

where β is some constant, M_{bin} is the mass of the binary, r is the orbital radius of the fluid element, and a_{bin} is the separation of the two stars. Likewise, we can set the damping rate as some fraction of the epicyclic frequency $\Gamma = \alpha\kappa$. The volumetric heating rate is then

$$\mathcal{S}_h = \frac{2\beta^2}{\alpha} \frac{\kappa GM_{\text{bin}}\rho}{r} \left(\frac{a_{\text{bin}}}{r} \right)^2. \quad (6.24)$$

Here we define the relevant constant as $\lambda \equiv 2\beta^2/\alpha$. Combining these terms together and setting $\kappa = \Omega$ in Keplerian potentials, we get,

$$\mathcal{S}_h = \lambda\Omega \frac{GM_{\text{bin}}\rho}{r} \left(\frac{a_{\text{bin}}}{r} \right)^2, \quad (6.25)$$

Here, we set $M_{\text{bin}} = 1.36 M_{\odot}$, and $a_{\text{bin}} = 5 R_{\odot}$. The heating from the central binary can be thought of as a periodic forcing from the binary driving a damped simple harmonic oscillator with a frequency equal to the epicyclic frequency, $\kappa = \Omega$.

Figure 6.10 shows v_r and ρ_s at 10 yr for different heating parameters λ . The heating

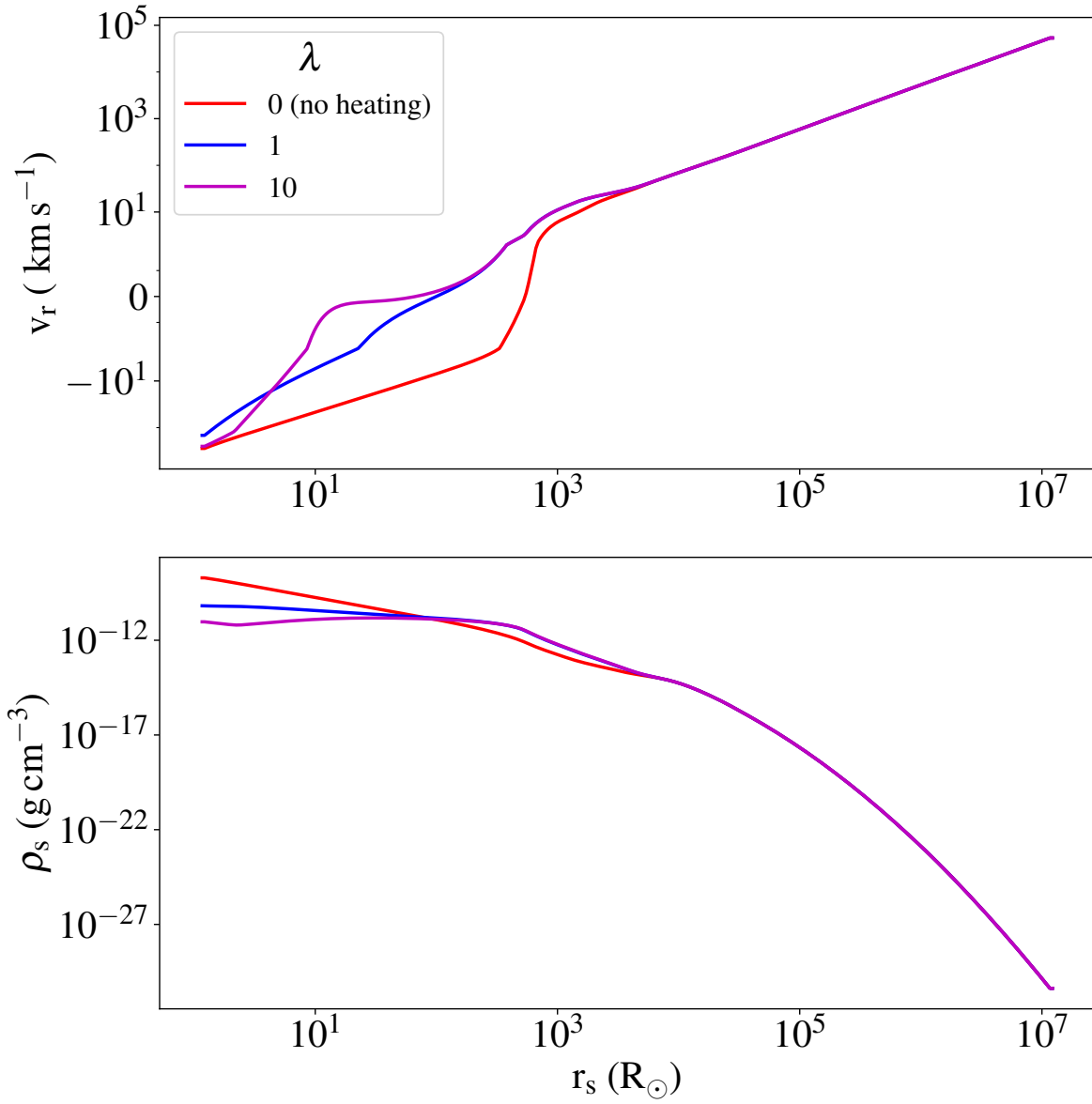


Figure 6.10: Scaled density (ρ_s) and radial velocity (v_r) as a function of scaled radius (r_s), for 10 yr and different heating parameters λ .

term \mathcal{S}_h impacts the inner envelope and has little impact in the outer regions ($r_s > 10^4 R_\odot$). For the case of no heating ($\lambda = 0$, red line), the inner regions follow a free-fall inflow solution. For larger heating rates, this inflow is suppressed but not completely eliminated, though the infall region occurs at substantially smaller radii than is effectively probed by our 3-D simulations. In either case, the heating rate makes no impact on either the density or velocity profile at large radii. We thus conclude that binary heating or any other late-time heating has little effect on the ultimate expansion and ejection of the envelope, but is required to prevent the infall of the innermost envelope. In the 3-D simulations, angular momentum or turbulence of the gas close to the binary may play a similar role, but this is not well modeled in the 1-D simulation. In any case, it is evident that there is extra physics that is not entirely accounted for in the 1-D model that leads to homologous expansion (at smaller radii) in the 3-D model.

6.3 DISCUSSION

In this work, we study the long-timescale evolution of CEE and the homologous nature of envelope expansion. We simulate a CE event using MANGA for a $2 M_\odot$ RGB and a $1 M_\odot$ MS star binary system. We show that nearly all gas from the red giant is unbound in 1500 d using an adiabatic equation of state and relying only on the release of orbital energy.

This is in agreement with and in contrast to other work. For instance, [Chamandy et al. \(2020\)](#) evolved a binary system of an AGB + white dwarf or MS star system through 20 orbits using an adiabatic equation of state. In agreement with our findings, they show that the envelope unbinds at a constant rate and would become unbound in less than 10 yr.

On the other hand, a number of others suggest that additional energy injection is nec-

essary. [Ondratschek et al. \(2022\)](#) studied a binary system consisting of an AGB primary similar to [Sand et al. \(2020\)](#) with a white dwarf or an MS star such that the mass ratio is 0.25 using the OPAL equation of state ([Rogers & Nayfonov, 2002](#)). They find a complete envelope ejection in about 1000 d when considering thermal and ionization energy along with mechanical energy, and in about 3400 d when ignoring the thermal and ionization energy. [Sand et al. \(2020\)](#) studied the fraction of unbound mass in two different simulations, one using the ideal gas equation of state and the other using the OPAL equation of state ([Rogers & Nayfonov, 2002](#)) for a binary system with an AGB primary and a white dwarf or an MS companion star such that the mass ratio is 0.5. In the case of the ideal gas equation of state, only 20 percent of the mass becomes unbound and the rate of mass ejection is slower if the internal energy is ignored. In their OPAL runs, 80 per cent of the mass is unbound in about 2500 d considering only the mechanical energy, and 100 per cent is ejected in about 1000 d considering mechanical energy along with thermal and recombination energy. Finally, [Iaconi et al. \(2019\)](#) find that the envelope of a binary system with $0.88 M_{\odot}$ RGB and a $0.6 M_{\odot}$ MS companion star is completely ejected in about 500 d when considering mechanical and recombination energies.

One crucial difference between our work and that of [Sand et al. \(2020\)](#) and [Ondratschek et al. \(2022\)](#) is that the cores of the stars end up in a much tighter binary in our case. In particular, [Sand et al. \(2020\)](#) starts the binary at $236 R_{\odot}$ but ends up at $41 R_{\odot}$. In our case, we start at around $50 R_{\odot}$, but end up at $5 R_{\odot}$. Hence, our orbit shrinks by a factor of nearly 10 whereas [Sand et al. \(2020\)](#)'s orbit shrinks by a factor of about 5. The corresponding relative gravitational energy release is hence a factor of 2 greater in our case.

In addition, we also show that the envelope reaches homologous expansion starting around a few hundred days (550 d). In comparison, [Iaconi et al. \(2019\)](#) showed that it takes about 5000 d for the bulk of the unbound gas to become homologously expanding,

even though the external layers of the envelope become homologous as soon as they are ejected. This difference may be due to the analysis methodology. Namely, [Iaconi et al. \(2019\)](#) traced the ballistic trajectories of SPH particles whereas we looked at the velocities of fluid elements and fit the velocities and associated radii to a $t_h = 0$ point. We are also simulating these events at substantially higher resolution through a combination of greater particle count and the use of a moving-mesh methodology.

Inspired by the homologous expansion in our 3-D simulation, we also study a 1-D model for $t > 800$ d. Unsurprisingly, we find that initializing the 1-D simulation with the spherical approximation of the 3-D simulation data produces homologous expansion in the bulk of the envelope. However, the inner regions require some additional physics not modeled in the 1-D simulation to preclude fallback and, hence, the breaking of homology. Here, we attribute this additional physics to heating from the periodic forcing of the binary but note that turbulence or angular momentum may play the same role.

The fact that simulated common-envelope events follow both a (roughly) spherical and homologous expansion approximation is likely useful for their theoretical and observational studies. First, CEE need not be numerically simulated for extremely long timescales. Instead, they only need to be simulated to the point where they begin homologous expansion, which occurs on a timescale of years as opposed to decades. This will result in significant computational savings and an associated expansion in the parameter space that can be explored.

Secondly, the fact that they obey both the spherical and homologous expansion approximations implies that radiation transfer codes that are used to calculate supernova light curves and spectra can be adapted to compute light curves and spectra from CEE events. Homologous expansion kinematic models are widely accepted as a good first-order approximation to model radiation transfer in supernova explosions ([Ropke, 2005](#);

[Kerzendorf & Sim, 2014](#); [Liu et al., 2018](#)). These radiation transfer codes typically assume a spherical and homologous expansion profile for the ejecta to greatly speed up the calculation. This fact has already been utilized by [Kamiński et al. \(2018\)](#) to model the CO emission in V4332 Sgr as a homologously expanding bipolar flow. Similarly [Kamiński et al. \(2020\)](#) show that the observed properties of the molecular remnant of Nova 1670 (CK Vulpeculae) are reproduced by assuming linear velocity fields.

Finally, we note that we have neglected effects, such as magnetic fields ([Ondratschek et al., 2022](#)) and jets (see for instance [Soker & Kaplan, 2021](#)) that could cause the outflow to become more non-spherical at late times. The effect of jets in CEE is still unclear, as [Zou et al. \(2022\)](#) found that jets are quickly choked within the envelope. On the other hand, [Ondratschek et al. \(2022\)](#) showed that late-time jet-like outflows produce the bipolar morphology seen in many planetary nebular systems. These effects will be a topic of future work.

CHAPTER 7

Conclusion

7.1 RAPID PARAMETER ESTIMATION OF GRAVITATIONAL WAVES

The discovery of GW170817, and the subsequent detection of GRB170817A and kilonovae, opened an era of multi-messenger astronomy. This pivotal observation underscored the necessity of promptly conducting electromagnetic follow-ups upon detecting CBCs involving NSs. The precise determination of the source’s location and the characterization of the stellar components are imperative for effectively conducting such follow-ups. [Pankow et al. \(2015\)](#) devised a parameter estimation framework designed to provide parameter estimation outcomes within minimal time frames. This is achieved by parallelizing likelihood computations across a grid of intrinsic parameters and employing Monte Carlo sampling for extrinsic parameters. However, the intrinsic parameter grid employed in this framework has some limitations, potentially compromising accuracy due to biases from the detection pipelines. To overcome this, I (and my collaborators) developed an alternate simplified grid placement algorithm that is rectilinear in shape. This grid placement algorithm is explained in Chapter 3 and is introduced in [Rose et al. \(2022\)](#). This pipeline named AMR RapidPE is combined with a faster extrinsic sampler (with the capability of using GPU and distance marginalization) from RIFT and is called RapidPE-RIFT. AMR RapidPE-RIFT is used in the fourth observing run and provides a source classification for CBC detection.

7.1.1 Current and Future Work

7.1.1.1 SNR Time Series from Search Pipeline

As noted earlier, the likelihood calculation is the main time-consuming step in RapidPE. Most of this cost is coming from estimating the term Equation 2.47. During detection, search pipelines need to estimate terms like this or proportional to this (referred to as SNR time series) for every template in the template bank. Additionally, there are ongoing efforts from GstLAL to interpolate this discrete SNR time series so that the SNR time series can be calculated for any non-template bank point. If RapidPE can use these SNR time series directly from the search pipelines, the overall RapidPE run time can be brought down to seconds. This is an ongoing effort and we are hoping to have this implemented in the next observing run.

7.1.1.2 Sky Localization

One main purpose of developing RapidPE is to provide an update to the sky localization after BAYESTAR sky localization in a low-latency timescale. To speed up the sampling in the extrinsic parameter space and to avoid sampling in low-likelihood regions, RapidPE can use the BAYESTAR skymap as a prior for sampling on the sky localization parameters. Additionally, one of our ongoing works is to use triangulation based on the arrival time at each detector to limit the extrinsic parameter space (Fairhurst, 2009). So, RapidPE already produces samples in the sky localization parameters for each intrinsic grid point. Since sampling is done for each intrinsic grid point, every extrinsic sample has a weight associated with it. There are modules used by LIGO, Virgo, and KAGRA to produce skymap from weighted samples such as `ligo.skymap`¹. However, the Kernel Density Estimation (KDE) on RapidPE samples with this module seems slow. An alternative is to

¹<https://lscsoft.docs.ligo.org/ligo.skymap/index.html>

plot the weighted samples without a KDE. One of the methods that we have tried is to assign each pixel in the skymap a weighed as a sum of the weight of all samples in that pixel. This needs to be carefully parametrized to have production quality resolution.

7.2 ENVELOPE EJECTION AND TRANSITION TO HOMOLOGOUS EXPANSION IN COMMON ENVELOPE EVOLUTION

In Chapter 6, we have analyzed the nature of expansion and the timescale of complete envelope ejection in common-envelope evolution. We used the moving-mesh hydrodynamic solver MANGA to perform a long-timescale simulation of a CE system involving a $2 M_{\odot}$ red giant and a $1 M_{\odot}$ main sequence star. We let the system evolve for around 13 yr. Starting at an orbital radius of $52 R_{\odot}$, the binary plateaus to an orbital radius of $5 R_{\odot}$ in 200 d. We observe that nearly all envelope material is unbound after 1500 d, and 80 percent is unbound in 400 d. This timescale is similar to that found by others who also studied envelope ejection in low-mass binary systems. However, we find that there is no need for additional energy injection from recombination.

Motivated by previous work by [Iaconi et al. \(2019\)](#), we also show that the envelope enters a phase of homologous expansion after 550 d. This is likely important for theoretical and observational work on CEE. First, one can have significant computational savings by doing numerical simulations up to the homologous start time and using the homologous expansion model afterward. Secondly, the radiative transfer codes used for finding light curves and spectra for supernovae can be adapted for use in CEE simulations.

Finally, we study the homologous expansion model in 1-D simulations using the power-law fits of the homologous phase as initial conditions. From this study, we found that periodic heating from the binary star at late times can affect the inner regions of the envelope but does not impact the homologous expansion.

7.2.1 Current and Future Work

7.2.1.1 *Radiation Hydrodynamics and Observational appearance of CEE*

As noted in Chapter 6, the fact that CEE eventually reaches homologous expansion is useful for the numerical modeling of CEE.

Firstly, one of the challenges in CEE simulation is to simulate CEE over long timescales to study different phases in the evolution. This challenge is primarily associated with the computational cost of such simulations. This is where the homologous expansion model becomes helpful. Once a CEE evolution in 3-D simulation reaches spherical and homologous expansion as described in Chapter 6, due to the spherical nature, only 1-D simulation is required thereafter to describe the evolution. This reduces the computational cost and enables us to simulate CEE for long timescales.

Secondly, spherical and homologous expansion provides a valuable framework for studying observational aspects of CEE through simulations. Even though there are a handful of optical transients attributed to CEE, generating light curves from simulation and comparing them with the observed transients is a relatively unexplored topic. There aren't many studies simulating CEE light curves and comparing them with observations is notable, primarily due to computational challenges in 3-D simulations over extended duration. However, the spherical and homologous nature of the envelope enables the utilization of 1-D hydrodynamics codes coupled with radiation transfer equations for light curve computation. [Chang et al. \(2020\)](#) implements radiation hydrodynamic for MANGA in 3-D. However, under the spherical approximation, this implementation can be simplified to a radial dimension in spherical coordinates.

BIBLIOGRAPHY

- Aasi, J., et al. (2015). Characterization of the LIGO detectors during their sixth science run. Classical and Quantum Gravity, 32(11), 115012.
- Abbott, B. P., et al. (2016a). GW151226: Observation of Gravitational Waves from a 22-Solar-Mass Binary Black Hole Coalescence. Phys. Rev. Lett., 116(24), 241103.
- Abbott, B. P., et al. (2016b). Observation of Gravitational Waves from a Binary Black Hole Merger. Phys. Rev. Lett., 116(6), 061102.
- Abbott, B. P., et al. (2017a). A gravitational-wave standard siren measurement of the Hubble constant. Nature, 551(7678), 85–88.
- Abbott, B. P., et al. (2017b). Gravitational Waves and Gamma-rays from a Binary Neutron Star Merger: GW170817 and GRB 170817A. Astrophys. J. Lett., 848(2), L13.
- Abbott, B. P., et al. (2017c). GW170817: Observation of Gravitational Waves from a Binary Neutron Star Inspiral. Phys. Rev. Lett., 119(16), 161101.
- Abbott, B. P., et al. (2017d). Multi-messenger Observations of a Binary Neutron Star Merger. Astrophys. J. Lett., 848(2), L12.
- Abbott, B. P., et al. (2020a). GW190425: Observation of a Compact Binary Coalescence with Total Mass $\sim 3.4M_{\odot}$. Astrophys. J. Lett., 892(1), L3.
- Abbott, R., et al. (2020b). GW190521: A Binary Black Hole Merger with a Total Mass of $150M_{\odot}$. Phys. Rev. Lett., 125(10), 101102.
- Abbott, R., et al. (2020c). GW190814: Gravitational Waves from the Coalescence of a 23 Solar Mass Black Hole with a 2.6 Solar Mass Compact Object. Astrophys. J. Lett., 896(2), L44.
- Abbott, R., et al. (2021a). GWTC-2: Compact Binary Coalescences Observed by LIGO and Virgo During the First Half of the Third Observing Run. Phys. Rev. X, 11, 021053.
- Abbott, R., et al. (2021b). GWTC-2: Compact Binary Coalescences Observed by LIGO and Virgo During the First Half of the Third Observing Run. Phys. Rev. X, 11, 021053.
- Abbott, R., et al. (2021c). Observation of Gravitational Waves from Two Neutron Star–Black Hole Coalescences. Astrophys. J. Lett., 915(1), L5.
- Abbott, R., et al. (2023). GWTC-3: Compact Binary Coalescences Observed by LIGO and Virgo during the Second Part of the Third Observing Run. Phys. Rev. X, 13(4), 041039.

- Abbott, R., et al. (2024). GWTC-2.1: Deep extended catalog of compact binary coalescences observed by LIGO and Virgo during the first half of the third observing run. Phys. Rev. D, 109(2), 022001.
- Acernese, F., et al. (2015). Advanced Virgo: a second-generation interferometric gravitational wave detector. Class. Quant. Grav., 32(2), 024001.
- Adams, T., Buskulic, D., Germain, V., Guidi, G. M., Marion, F., Montani, M., Mours, B., Piergiovanni, F., & Wang, G. (2016). Low-latency analysis pipeline for compact binary coalescences in the advanced gravitational wave detector era. Classical and Quantum Gravity, 33(17), 175012.
- Akutsu, T., et al. (2021). Overview of KAGRA: Detector design and construction history. PTEP, 2021(5), 05A101.
- Ashton, G., et al. (2019). BILBY: A user-friendly Bayesian inference library for gravitational-wave astronomy. Astrophys. J. Suppl., 241(2), 27.
- Babak, S., Biswas, R., Brady, P. R., Brown, D. A., Cannon, K., Capano, C. D., Clayton, J. H., Cokelaer, T., Creighton, J. D. E., Dent, T., & et al. (2013). Searching for gravitational waves from binary coalescence. Physical Review D, 87(2).
- Belczynski, K., Kalogera, V., & Bulik, T. (2001). A Comprehensive study of binary compact objects as gravitational wave sources: Evolutionary channels, rates, and physical properties. Astrophys. J., 572, 407–431.
- Belczynski, K., et al. (2020). Evolutionary roads leading to low effective spins, high black hole masses, and O1/O2 rates for LIGO/Virgo binary black holes. Astron. Astrophys., 636, A104.
- Berger, M. J., & Colella, P. (1989). Local adaptive mesh refinement for shock hydrodynamics. Journal of Computational Physics, 82, 64–84.
- Berry, C. P. L., et al. (2015). Parameter estimation for binary neutron-star coalescences with realistic noise during the Advanced LIGO era. Astrophys. J., 804(2), 114.
- Bethe, H. A., & Brown, G. E. (1998). Evolution of binary compact objects which merge. Astrophys. J., 506, 780–789.
- Biver, C. M., Capano, C. D., De, S., Cabero, M., Brown, D. A., Nitz, A. H., & Raymond, V. (2019). PyCBC Inference: A Python-based parameter estimation toolkit for compact binary coalescence signals. Publ. Astron. Soc. Pac., 131(996), 024503.
- Bond, H. E., Henden, A., Levay, Z. G., Panagia, N., Sparks, W. B., Starrfield, S., Wagner, R. M., Corradi, R. L. M., & Munari, U. (2003). An energetic stellar outburst accompanied by circumstellar light echoes. Nature, 422, 405–408.

- Bond, H. E., Liller, W., & Mannery, E. J. (1978). UU Sagittae: eclipsing nucleus of the planetary nebula Abell 63. , 223, 252–259.
- Bryan, G. L., Norman, M. L., O’Shea, B. W., Abel, T., Wise, J. H., Turk, M. J., Reynolds, D. R., Collins, D. C., Wang, P., Skillman, S. W., Smith, B., Harkness, R. P., Bordner, J., Kim, J.-h., Kuhlen, M., Xu, H., Goldbaum, N., Hummels, C., Kritsuk, A. G., Tasker, E., Skory, S., Simpson, C. M., Hahn, O., Oishi, J. S., So, G. C., Zhao, F., Cen, R., & Li, Y. (2014). Enzo: An adaptive mesh refinement code for astrophysics. The Astrophysical Journal Supplement Series, 211(2), 19.
- Buonanno, A., Iyer, B., Ochsner, E., Pan, Y., & Sathyaprakash, B. S. (2009). Comparison of post-Newtonian templates for compact binary inspiral signals in gravitational-wave detectors. Phys. Rev. D, 80, 084043.
- Chamandy, L., Blackman, E. G., Frank, A., Carroll-Nellenback, J., & Tu, Y. (2020). Common envelope evolution on the asymptotic giant branch: unbinding within a decade? , 495(4), 4028–4039.
- Chang, P., Davis, S. W., & Jiang, Y.-F. (2020). Time-dependent radiation hydrodynamics on a moving mesh. Mon. Not. Roy. Astron. Soc., 493(4), 5397–5407.
- Chang, P., & Etienne, Z. (2020). General relativistic hydrodynamics on a moving-mesh I: static space-times. Mon. Not. Roy. Astron. Soc., 496(1), 206–214.
- Chang, P., Wadsley, J., & Quinn, T. R. (2017). A moving-mesh hydrodynamic solver for ChaNGa. , 471(3), 3577–3589.
- Chatziioannou, K. (2020). Neutron star tidal deformability and equation of state constraints. Gen. Rel. Grav., 52(11), 109.
- Chini, R., Hoffmeister, V. H., Nasserri, A., Stahl, O., & Zinnecker, H. (2012). A spectroscopic survey on the multiplicity of high-mass stars. , 424(3), 1925–1929.
- Chu, Q., Kovalam, M., Wen, L., Slaven-Blair, T., Bosveld, J., Chen, Y., Clearwater, P., Codoreanu, A., Du, Z., Guo, X., Guo, X., Kim, K., Li, T. G. F., Oloworaran, V., Panther, F., Powell, J., Sengupta, A. S., Wette, K., & Zhu, X. (2021). The spiir online coherent pipeline to search for gravitational waves from compact binary coalescences.
- Colombo, A., Salafia, O. S., Gabrielli, F., Ghirlanda, G., Giacomazzo, B., Perego, A., & Colpi, M. (2022). Multi-messenger Observations of Binary Neutron Star Mergers in the O4 Run. Astrophys. J., 937(2), 79.
- Coulter, D. A., Kilpatrick, C. D., Siebert, M. R., Foley, R. J., Shappee, B. J., Drout, M. R., Simon, J. S., Piro, A. L., Rest, A., & One-Meter Two-Hemisphere (1M2H) Collaboration (2017). LIGO/Virgo G298048: Potential optical counterpart discovered by Swope telescope. GRB Coordinates Network, 21529, 1.

- Creighton, J., & Anderson, W. (2011). Gravitational-Wave Physics and Astronomy: An Introduction to Theory, Experiment and Data Analysis.
- Cunningham, A. J., Frank, A., Varniere, P., Mitran, S., & Jones, T. W. (2009). Simulating Magnetohydrodynamical Flow with Constrained Transport and Adaptive Mesh Refinement: Algorithms & Tests of the AstroBEAR Code. Astrophys. J. Suppl., 182, 519–542.
- Damour, T., Nagar, A., & Villain, L. (2012). Measurability of the tidal polarizability of neutron stars in late-inspiral gravitational-wave signals. Phys. Rev. D, 85, 123007.
- Damour, T., Soffel, M., & Xu, C.-m. (1992). General relativistic celestial mechanics. 2. Translational equations of motion. Phys. Rev. D, 45, 1017–1044.
- Darwin, G. H. (1879). The Determination of the Secular Effects of Tidal Friction by a Graphical Method. Proceedings of the Royal Society of London Series I, 29, 168–181.
- de Kool, M. (1987). Models of interacting binary stars. Ph.D. thesis, -.
- de Mink, S. E., & Mandel, I. (2016). The chemically homogeneous evolutionary channel for binary black hole mergers: rates and properties of gravitational-wave events detectable by advanced LIGO. Mon. Not. Roy. Astron. Soc., 460(4), 3545–3553.
- Dominik, M., Belczynski, K., Fryer, C., Holz, D., Berti, E., Bulik, T., Mandel, I., & O’Shaughnessy, R. (2012). Double Compact Objects I: The Significance of the Common Envelope on Merger Rates. Astrophys. J., 759, 52.
- Dominik, M., Berti, E., O’Shaughnessy, R., Mandel, I., Belczynski, K., Fryer, C., Holz, D. E., Bulik, T., & Pannarale, F. (2015). Double Compact Objects III: Gravitational Wave Detection Rates. Astrophys. J., 806(2), 263.
- Donea, J., Huerta, A., Ponthot, J.-P., & Rodríguez-Ferran, A. (2004). Arbitrary Lagrangian–Eulerian Methods, chap. 14. John Wiley Sons, Ltd.
- Dubey, A., Almgren, A., Bell, J., Berzins, M., Brandt, S., Bryan, G., Colella, P., Graves, D., Lijewski, M., Löffler, F., O’Shea, B., Schnetter, E., Straalen, B. V., & Weide, K. (2014). A survey of high level frameworks in block-structured adaptive mesh refinement packages. Journal of Parallel and Distributed Computing, 74(12), 3217 – 3227. Domain-Specific Languages and High-Level Frameworks for High-Performance Computing.
- Duchêne, G., & Kraus, A. (2013). Stellar Multiplicity. , 51(1), 269–310.
- Duffell, P. C., & MacFadyen, A. I. (2011). TESS: A Relativistic Hydrodynamics Code on a Moving Voronoi Mesh. Astrophys. J. Suppl., 197, 15.

- Duquennoy, A., & Mayor, M. (1991). Multiplicity among Solar Type Stars in the Solar Neighbourhood - Part Two - Distribution of the Orbital Elements in an Unbiased Sample. , 248, 485.
- Einfeldt, B. (1988). On Godunov-Type Methods for Gas Dynamics. SIAM Journal on Numerical Analysis, 25(2), 294–318.
- Einstein, A. (1916). The foundation of general relativity. Annals of Physics, 354(7), 769–822.
- Fairhurst, S. (2009). Triangulation of gravitational wave sources with a network of detectors. New J. Phys., 11, 123006. [Erratum: New J. Phys. 13, 069602 (2011)].
- Flanagan, E. E., & Hinderer, T. (2008). Constraining neutron star tidal Love numbers with gravitational wave detectors. Phys. Rev. D, 77, 021502.
- Foreman-Mackey, D., Hogg, D. W., Lang, D., & Goodman, J. (2013). emcee: The MCMC Hammer. , 125(925), 306.
- Fraleley, G. S. (1968). Supernovae Explosions Induced by Pair-Production Instability. , 2(1), 96–114.
- Fryer, C. L., Rockefeller, G., & Warren, M. S. (2006). Snsph: a parallel 3d smoothed particle radiation hydrodynamics code. Astrophys. J., 643, 292–305.
- Fryer, C. L., Woosley, S. E., & Hartmann, D. H. (1999). Formation rates of black hole accretion disk gamma-ray bursts. Astrophys. J., 526, 152.
- Fryer, C. L., et al. (2007). Constraints on Type Ib/c and GRB Progenitors. Publ. Astron. Soc. Pac., 119, 1211.
- Fryxell, B., Olson, K., Ricker, P., Timmes, F. X., Zingale, M., Lamb, D. Q., MacNeice, P., Rosner, R., Truran, J. W., & Tufo, H. (2000). FLASH: An Adaptive Mesh Hydrodynamics Code for Modeling Astrophysical Thermonuclear Flashes. , 131(1), 273–334.
- Gaburov, E., Johansen, A., & Levin, Y. (2012). Magnetically-levitating disks around supermassive black holes. Astrophys. J., 758, 103.
- Gaburov, E., Lombardi, J., James C., & Portegies Zwart, S. (2010). On the onset of runaway stellar collisions in dense star clusters - II. Hydrodynamics of three-body interactions. , 402(1), 105–126.
- Gammie, C. F., McKinney, J. C., & Toth, G. (2003). HARM: A Numerical scheme for general relativistic magnetohydrodynamics. Astrophys. J., 589, 444–457.
- Gilks, W. R., Richardson, S., & Spiegelhalter, D. J. (1998). Markov chain Monte Carlo in practice. Chapman Hall.

- Gingold, R. A., & Monaghan, J. J. (1977). Smoothed particle hydrodynamics: theory and application to non-spherical stars. , 181, 375–389.
- Goldstein, A., et al. (2017). An Ordinary Short Gamma-Ray Burst with Extraordinary Implications: Fermi-GBM Detection of GRB 170817A. Astrophys. J. Lett., 848(2), L14.
- Han, Z., Podsiadlowski, P., & Eggleton, P. P. (1994). A possible criterion for envelope ejection in asymptotic giant branch or first giant branch stars. , 270, 121–130.
- Han, Z., Podsiadlowski, P., & Eggleton, P. P. (1995). The formation of bipolar planetary nebulae and close white dwarf binaries. , 272(4), 800–820.
- Han, Z., Podsiadlowski, P., Maxted, P. F. L., Marsh, T. R., & Ivanova, N. (2002). The Origin of subdwarf B stars. 1. The Formation channels. Mon. Not. Roy. Astron. Soc., 336, 449–466.
- Harten, A., Lax, P. D., & Leer, B. v. (1983). On upstream differencing and godunov-type schemes for hyperbolic conservation laws. SIAM Review, 25(1), 35–61.
- Hulse, R. A., & Taylor, J. H. (1975). Discovery of a pulsar in a binary system. , 195, L51–L53.
- Iaconi, R., Maeda, K., De Marco, O., Nozawa, T., & Reichardt, T. (2019). Properties of the post-inspiral common envelope ejecta - I. Dynamical and thermal evolution. , 489(3), 3334–3350.
- Ivanova, N. (2002). Slow mergers of massive stars. Ph.D. thesis.
- Ivanova, N., Justham, S., Chen, X., De Marco, O., Fryer, C. L., Gaburov, E., Ge, H., Glebbeek, E., Han, Z., Li, X. D., Lu, G., Marsh, T., Podsiadlowski, P., Potter, A., Soker, N., Taam, R., Tauris, T. M., van den Heuvel, E. P. J., & Webbink, R. F. (2013). Common envelope evolution: where we stand and how we can move forward. , 21, 59.
- Ivanova, N., Justham, S., & Ricker, P. (2020). Common Envelope Evolution.
- Ivanova, N., & Podsiadlowski, P. (2003). The slow merger of massive stars. In ESO / MPA / MPE Workshop: From Twilight to Highlight: The Physics of Supernovae, ESO Astrophysics Symposia European Southern Observatory, (pp. 19–22).
- Jermyn, A. S., et al. (2023). Modules for Experiments in Stellar Astrophysics (MESA): Time-dependent Convection, Energy Conservation, Automatic Differentiation, and Infrastructure. Astrophys. J. Suppl., 265(1), 15.
- Jetley, P., Gioachin, F., Mendes, C., Kale, L. V., & Quinn, T. (2008). Massively parallel cosmological simulations with changa. In 2008 IEEE International Symposium on Parallel and Distributed Processing, (pp. 1–12).

- Jetley, P., Wesolowski, L., Gioachin, F., Kalé, L. V., & Quinn, T. R. (2010). Scaling hierarchical n-body simulations on gpu clusters. In *SC '10: Proceedings of the 2010 ACM/IEEE International Conference for High Performance Computing, Networking, Storage and Analysis*, (pp. 1–11).
- Jones, D. (2018). The importance of binarity in the formation and evolution of planetary nebulae. *arXiv e-prints*, (p. arXiv:1806.08244).
- Kalogera, V., & Webbink, R. F. (1998). Formation of low mass x-ray binaries. 2. Common envelope evolution of primordial binaries with extreme mass ratios. *Astrophys. J.*, *493*, 351.
- Kamiński, T., Menten, K. M., Tylenda, R., Wong, K. T., Belloche, A., Mehner, A., Schmidt, M. R., & Patel, N. A. (2020). Molecular remnant of Nova 1670 (CK Vulpeculae). I. Properties and enigmatic origin of the gas. , *644*, A59.
- Kamiński, T., Steffen, W., Tylenda, R., Young, K. H., Patel, N. A., & Menten, K. M. (2018). Submillimeter-wave emission of three Galactic red novae: cool molecular outflows produced by stellar mergers. , *617*, A129.
- Kapadia, S. J., et al. (2019). A self-consistent method to estimate the rate of compact binary coalescences with a Poisson mixture model.
- Kasliwal, M. M. (2012). Systematically Bridging the Gap Between Novae and Supernovae. , *29*(4), 482–488.
- Kerzendorf, W. E., & Sim, S. A. (2014). A spectral synthesis code for rapid modelling of supernovae. , *440*(1), 387–404.
- Kiendrebeogo, R. W., et al. (2023). Updated Observing Scenarios and Multimessenger Implications for the International Gravitational-wave Networks O4 and O5. *Astrophys. J.*, *958*(2), 158.
- Kulkarni, S. R., et al. (2007). An unusually brilliant transient in the galaxy Messier 85. *Nature*, *447*, 458–460.
- Lange, J., O’Shaughnessy, R., & Rizzo, M. (2018). Rapid and accurate parameter inference for coalescing, precessing compact binaries.
- Lattimer, J. M., & Schramm, D. N. (1974). Black-hole-neutron-star collisions. *Astrophys. J. Lett.*, *192*, L145.
- Li, L.-X., & Paczynski, B. (1998). Transient events from neutron star mergers. *Astrophys. J. Lett.*, *507*, L59.

- LIGO Scientific Collaboration, Virgo Collaboration, & KAGRA Collaboration (2018). LIGO Algorithm Library - LALSuite. Free software (GPL).
- Liu, L.-D., Zhang, B., Wang, L.-J., & Dai, Z.-G. (2018). Photospheric Radius Evolution of Homologous Explosions. *Astrophys. J. Lett.*, 868(2), L24.
- Livio, M., & Soker, N. (1988). The Common Envelope Phase in the Evolution of Binary Stars. , 329, 764.
- Lück, H., et al. (2006). Status of the GEO600 detector. *Class. Quant. Grav.*, 23, S71–S78.
- Lucy, L. B. (1977). A numerical approach to the testing of the fission hypothesis. , 82, 1013–1024.
- MacLeod, M., Macias, P., Ramirez-Ruiz, E., Grindlay, J., Batta, A., & Montes, G. (2017). Lessons from the Onset of a Common Envelope Episode: the Remarkable M31 2015 Luminous Red Nova Outburst. , 835(2), 282.
- Mapelli, M., & Giacobbo, N. (2018). The cosmic merger rate of neutron stars and black holes. *Mon. Not. Roy. Astron. Soc.*, 479(4), 4391–4398.
- Martini, P., Wagner, R. M., Tomaney, A., Rich, R. M., Della Valle, M., & Hauschildt, P. H. (1999). Nova sagittarii 1994 #1 (v4332 sagittarii): the discovery and evolution of an unusual luminous red variable star. *Astron. J.*, 118, 1034–1042.
- Menon, H., Wesolowski, L., Zheng, G., Jetley, P., Kale, L., Quinn, T., & Governato, F. (2015). Adaptive techniques for clustered N-body cosmological simulations. *Computational Astrophysics and Cosmology*, 2, 1.
- Messick, C., Blackburn, K., Brady, P., Brockill, P., Cannon, K., Cariou, R., Caudill, S., Chamberlin, S. J., Creighton, J. D., Everett, R., & et al. (2017). Analysis framework for the prompt discovery of compact binary mergers in gravitational-wave data. *Physical Review D*, 95(4).
- Metzger, B. D. (2020). Kilonovae. *Living Rev. Rel.*, 23(1), 1.
- Meyer, F., & Meyer-Hofmeister, E. (1979). Formation of cataclysmic binaries through common envelope evolution. , 78, 167–176.
- Mitchell, D. L., Pollacco, D., O'Brien, T. J., Bryce, M., Lopez, J. A., Meaburn, J., & Vaytet, N. M. H. (2007). Proof of polar ejection from the close-binary core of the planetary nebula Abell 63. *Mon. Not. Roy. Astron. Soc.*, 374, 1404–1412.
- Moe, B., Brady, P., Stephens, B., Katsavounidis, E., Williams, R., Zhang, F., et al. (2014). Ligo-t1400365-v5: Gracedb: A gravitational wave candidate event database. <https://dcc.ligo.org/LIGO-T1400365/public>.

- Monaghan, J. J. (1992). Smoothed particle hydrodynamics. , 30, 543–574.
- Nandez, J. L. A., Ivanova, N., & Lombardi, J. C. J. (2015). Recombination energy in double white dwarf formation. , 450, L39–L43.
- Nestle (2014). <http://kylebarbary.com/nestle/>.
- Nissanke, S., Holz, D. E., Hughes, S. A., Dalal, N., & Sievers, J. L. (2010). Exploring short gamma-ray bursts as gravitational-wave standard sirens. Astrophys. J., 725, 496–514.
- Ohlmann, S. T., Röpke, F. K., Pakmor, R., & Springel, V. (2016). Hydrodynamic Moving-mesh Simulations of the Common Envelope Phase in Binary Stellar Systems. , 816(1), L9.
- Okabe, A., Boots, B., & Sugihara, K. (1992). Spatial tessellations. Concepts and Applications of Voronoi diagrams.
- Ondratschek, P. A., Röpke, F. K., Schneider, F. R. N., Fendt, C., Sand, C., Ohlmann, S. T., Pakmor, R., & Springel, V. (2022). Bipolar planetary nebulae from common-envelope evolution of binary stars. , 660, L8.
- Paczynski, B. (1976). Common Envelope Binaries. In P. Eggleton, S. Mitton, & J. Whelan (Eds.) Structure and Evolution of Close Binary Systems, vol. 73, (p. 75).
- Pankow, C., Brady, P., Ochsner, E., & O’Shaughnessy, R. (2015). Novel scheme for rapid parallel parameter estimation of gravitational waves from compact binary coalescences. Phys. Rev. D, 92(2), 023002.
- Passy, J.-C., De Marco, O., Fryer, C. L., Herwig, F., Diehl, S., Oishi, J. S., Mac Low, M.-M., Bryan, G. L., & Rockefeller, G. (2012). Simulating the Common Envelope Phase of a Red Giant Using Smoothed-particle Hydrodynamics and Uniform-grid Codes. , 744(1), 52.
- Paxton, B., Bildsten, L., Dotter, A., Herwig, F., Lesaffre, P., & Timmes, F. (2011). Modules for Experiments in Stellar Astrophysics (MESA). , 192(1), 3.
- Paxton, B., Cantiello, M., Arras, P., Bildsten, L., Brown, E. F., Dotter, A., Mankovich, C., Montgomery, M. H., Stello, D., Timmes, F. X., & Townsend, R. (2013). Modules for Experiments in Stellar Astrophysics (MESA): Planets, Oscillations, Rotation, and Massive Stars. , 208(1), 4.
- Paxton, B., Marchant, P., Schwab, J., Bauer, E. B., Bildsten, L., Cantiello, M., Dessart, L., Farmer, R., Hu, H., Langer, N., Townsend, R. H. D., Townsley, D. M., & Timmes, F. X. (2015). Modules for Experiments in Stellar Astrophysics (MESA): Binaries, Pulsations, and Explosions. , 220(1), 15.

- Paxton, B., Schwab, J., Bauer, E. B., Bildsten, L., Blinnikov, S., Duffell, P., Farmer, R., Goldberg, J. A., Marchant, P., Sorokina, E., Thoul, A., Townsend, R. H. D., & Timmes, F. X. (2018). Modules for Experiments in Stellar Astrophysics (MESA): Convective Boundaries, Element Diffusion, and Massive Star Explosions. , 234(2), 34.
- Paxton, B., Smolec, R., Schwab, J., Gaudy, A., Bildsten, L., Cantiello, M., Dotter, A., Farmer, R., Goldberg, J. A., Jermyn, A. S., Kanbur, S. M., Marchant, P., Thoul, A., Townsend, R. H. D., Wolf, W. M., Zhang, M., & Timmes, F. X. (2019). Modules for Experiments in Stellar Astrophysics (MESA): Pulsating Variable Stars, Rotation, Convective Boundaries, and Energy Conservation. , 243(1), 10.
- Podsiadlowski, P. (2001). Common-envelope evolution and stellar mergers. In P. Podsiadlowski, S. Rappaport, A. R. King, F. D'Antona, & L. Burderi (Eds.) Evolution of Binary and Multiple Star Systems, vol. 229 of Astronomical Society of the Pacific Conference Series, (p. 239).
- Podsiadlowski, P., Ivanova, N., Justham, S., & Rappaport, S. (2010). Explosive common-envelope ejection: implications for gamma-ray bursts and low-mass black-hole binaries. Monthly Notices of the Royal Astronomical Society, 406(2), 840–847.
- Price, D. J., et al. (2018). PHANTOM: A Smoothed Particle Hydrodynamics and Magnetohydrodynamics Code for Astrophysics. Publ. Astron. Soc. Austral., 35, 31.
- Prust, L. J. (2020). Moving and reactive boundary conditions in moving-mesh hydrodynamics. , 494(4), 4616–4626.
- Prust, L. J., & Chang, P. (2019). Common envelope evolution on a moving mesh. , 486(4), 5809–5818.
- Raghavan, D., McAlister, H. A., Henry, T. J., Latham, D. W., Marcy, G. W., Mason, B. D., Gies, D. R., White, R. J., & ten Brummelaar, T. A. (2010). A Survey of Stellar Families: Multiplicity of Solar-type Stars. , 190(1), 1–42.
- Rasio, F. A., & Livio, M. (1996). On the formation and evolution of common envelope systems. Astrophys. J., 471, 366.
- Read, J. S., Baiotti, L., Creighton, J. D. E., Friedman, J. L., Giacomazzo, B., Kyutoku, K., Markakis, C., Rezzolla, L., Shibata, M., & Taniguchi, K. (2013). Matter effects on binary neutron star waveforms. Phys. Rev. D, 88, 044042.
- Ricker, P. M., & Taam, R. E. (2012). An AMR Study of the Common-envelope Phase of Binary Evolution. , 746(1), 74.
- Rodriguez, C. L., Chatterjee, S., & Rasio, F. A. (2016). Binary Black Hole Mergers from Globular Clusters: Masses, Merger Rates, and the Impact of Stellar Evolution. Phys. Rev. D, 93(8), 084029.

- Rogers, F. J., & Nayfonov, A. (2002). Updated and Expanded OPAL Equation-of-State Tables: Implications for Helioseismology. , 576(2), 1064–1074.
- Romero-Shaw, I. M., Talbot, C., Biscoveanu, S., D’Emilio, V., Ashton, G., Berry, C. P. L., Coughlin, S., Galaudage, S., Hoy, C., Hübner, M., & et al. (2020). Bayesian inference for compact binary coalescences with bilby: validation and application to the first ligo–virgo gravitational-wave transient catalogue. Monthly Notices of the Royal Astronomical Society, 499(3), 3295–3319.
- Ropke, F. K. (2005). Following multi-dimensional Type Ia supernova explosion models to homologous expansion. Astron. Astrophys., 432, 969.
- Rose, C. (2024). Rapid Parameter Estimation of Compact Binary Coalescences with Gravitational Waves. Ph.D. thesis.
- Rose, C. A., Valsan, V., Brady, P. R., Walsh, S., & Pankow, C. (2022). Supplementing rapid Bayesian parameter estimation schemes with adaptive grids.
- Rosswog, S., & Price, D. (2007). MAGMA: a 3D, Lagrangian magnetohydrodynamics code for merger applications. Mon. Not. Roy. Astron. Soc., 379, 915–931.
- Rycroft, C. H. (2009). VORO++: A three-dimensional Voronoi cell library in C++. Chaos, 19(4), 041111.
- Salafia, O. (2024). Forecasting the probability of the detection of a compact binary merger in a science run based on previous detections.
- Salvatier, J., Wiecki, T., & Fonnesbeck, C. (2015). Probabilistic Programming in Python using PyMC. arXiv e-prints, (p. arXiv:1507.08050).
- Sand, C., Ohlmann, S. T., Schneider, F. R. N., Pakmor, R., & Röpke, F. K. (2020). Common-envelope evolution with an asymptotic giant branch star. , 644, A60.
- Sandquist, E. L., Taam, R. E., & Burkert, A. (2000). On the formation of helium double degenerate stars and pre-cataclysmic variables. Astrophys. J., 533, 984.
- Sandquist, E. L., Taam, R. E., Chen, X., Bodenheimer, P., & Burkert, A. (1998). Double core evolution x. through the envelope ejection phase. Astrophys. J., 500, 909.
- Savchenko, V., et al. (2017). INTEGRAL Detection of the First Prompt Gamma-Ray Signal Coincident with the Gravitational-wave Event GW170817. Astrophys. J. Lett., 848(2), L15.
- Schutz, B. F. (1986). Determining the Hubble constant from gravitational wave observations. , 323(6086), 310–311.

- Singer, L. P., & Price, L. R. (2016). Rapid Bayesian position reconstruction for gravitational-wave transients. *Phys. Rev. D*, 93(2), 024013.
- Singer, L. P., et al. (2014). The First Two Years of Electromagnetic Follow-Up with Advanced LIGO and Virgo. *Astrophys. J.*, 795(2), 105.
- Skilling, J. (2012). Bayesian computation in big spaces-nested sampling and Galilean Monte Carlo. *AIP Conference Proceedings*, 1443(1), 145–156.
- Soker, N., & Kaplan, N. (2021). Explaining recently studied intermediate luminosity optical transients (ILOTs) with jet powering. *Res. Astron. Astrophys.*, 21(4), 090.
- Soker, N., & Rappaport, S. (2000). The formation of very narrow waist bipolar planetary nebulae. *Astrophys. J.*, 538, 241–259.
- Spaulding, A., & Chang, P. (2021). The Effect of Impact Parameter on Tidal Disruption Events. *Mon. Not. Roy. Astron. Soc.*, 501(2), 1748–1754.
- Speagle, J. S. (2020). DYNESTY: a dynamic nested sampling package for estimating Bayesian posteriors and evidences. , 493(3), 3132–3158.
- Springel, V. (2010). E pur si muove: Galilean-invariant cosmological hydrodynamical simulations on a moving mesh. , 401(2), 791–851.
- Springel, V., Yoshida, N., & White, S. D. M. (2001). GADGET: A Code for collisionless and gasdynamical cosmological simulations. *New Astron.*, 6, 79.
- Stone, J. M., Gardiner, T. A., Teuben, P., Hawley, J. F., & Simon, J. B. (2008). Athena: A New Code for Astrophysical MHD. *Astrophys. J. Suppl.*, 178, 137.
- Taam, R. E. (1996). Common-Envelope Evolution, the Formation of CVs, LMXBs, and the Fate of HMXBs. In J. van Paradijs, E. P. J. van den Heuvel, & E. Kuulkers (Eds.) *Compact Stars in Binaries*, vol. 165, (p. 3).
- Takahashi, R., & TAMA Collaboration (2004). Status of TAMA300. *Classical and Quantum Gravity*, 21(5), S403–S408.
- Tanaka, M., & Hotokezaka, K. (2013). Radiative Transfer Simulations of Neutron Star Merger Ejecta. *Astrophys. J.*, 775, 113.
- Tauris, T. M., & Dewi, J. D. M. (2001). On the binding energy parameter of common envelope evolution. dependency on the definition of the stellar core boundary during spiral-in. *Astron. Astrophys.*, 369, 170.
- Terman, J. L., Taam, R. E., & Hernquist, L. (1994). Double-Core Evolution. V. Three-dimensional Effects in the Merger of a Red Giant with a Dwarf Companion. , 422, 729.

- Terman, J. L., Taam, R. E., & Hernquist, L. (1995). Double Core Evolution. VII. The Infall of a Neutron Star through the Envelope of Its Massive Star Companion. , 445, 367.
- Teyssier, R. (2002). Cosmological hydrodynamics with adaptive mesh refinement: a new high resolution code called RAMSES. Astron. Astrophys., 385, 337–364.
- Tylenda, R., Hajduk, M., Kamiński, T., Udalski, A., Soszyński, I., Szymański, M. K., Ku-
biak, M., Pietrzyński, G., Poleski, R., Wyrzykowski, Ł., & Ulaczyk, K. (2011). V1309
Scorpii: merger of a contact binary. , 528, A114.
- Tylenda, R., Soker, N., & Szczerba, R. (2005). On the progenitor of V838 Monocerotis.
Astron. Astrophys., 441, 1099.
- Valsan, V., Borges, S. V., Prust, L., & Chang, P. (2023). Envelope ejection and the transition
to homologous expansion in common-envelope events. Mon. Not. Roy. Astron. Soc.,
526(4), 5365–5373.
- Valsan, V., & Wysocki, D. (2024). Rapidpe-rift / rapidpe-rift rota tools · gitlab. <https://git.ligo.org/rapidpe-rift/rapidpe-rift-rota-tools>.
- Valsan, V., Wysocki, D., Rose, C., Walsh, S., & Brady, P. (2022). Rapidpe-rift / rapidpe-rift
pipeline · gitlab. <https://git.ligo.org/rapidpe-rift/rapidpe-rift-pipe>.
- Veitch, J., Pozzo, W. D., Lyttle, A., Williams, M., Talbot, C., Pitkin, M., Ashton, G., Cody,
Hübner, M., Nitz, A., & et al. (2022). Johnveitch/cpnest: V0.11.3. <https://doi.org/10.5281/zenodo.4470001>.
- Veitch, J., et al. (2015a). Parameter estimation for compact binaries with ground-based
gravitational-wave observations using the LALInference software library. Phys. Rev.
D, 91(4), 042003.
- Veitch, J., et al. (2015b). Parameter estimation for compact binaries with ground-based
gravitational-wave observations using the LALInference software library. Phys. Rev.
D, 91(4), 042003.
- Vigna-Gómez, A., et al. (2018). On the formation history of Galactic double neutron stars.
Mon. Not. Roy. Astron. Soc., 481(3), 4009–4029.
- Vines, J., Flanagan, E. E., & Hinderer, T. (2011). Post-1-Newtonian tidal effects in the
gravitational waveform from binary inspirals. Phys. Rev. D, 83, 084051.
- Vousden, W. D., Farr, W. M., & Mandel, I. (2016). Dynamic temperature selection for
parallel tempering in Markov chain Monte Carlo simulations. , 455(2), 1919–1937.
- Webbink, R. F. (1984). Double white dwarfs as progenitors of R Coronae Borealis stars
and type I supernovae. , 277, 355–360.

- Weber, J. (1960). Detection and Generation of Gravitational Waves. Physical Review, 117(1), 306–313.
- Weisberg, J. M., & Taylor, J. H. (2005). The Relativistic Binary Pulsar B1913+16: Thirty Years of Observations and Analysis. In F. A. Rasio, & I. H. Stairs (Eds.) Binary Radio Pulsars, vol. 328 of Astronomical Society of the Pacific Conference Series, (p. 25).
- Wetzstein, M., Nelson, A. F., Naab, T., & Burkert, A. (2009). Vine—A Numerical Code for Simulating Astrophysical Systems Using Particles. I. Description of the Physics and the Numerical Methods. , 184(2), 298–325.
- Wofford, J., Yelikar, A., Gallagher, H., Champion, E., Wysocki, D., Delfavero, V., Lange, J., Rose, C., Valsan, V., Morisaki, S., Read, J., Henshaw, C., & O’Shaughnessy, R. (2022). Expanding RIFT: Improving performance for GW parameter inference. arXiv e-prints, (p. arXiv:2210.07912).
- Wysocki, D., O’Shaughnessy, R., Lange, J., & Fang, Y.-L. L. (2019). Accelerating parameter inference with graphics processing units. Phys. Rev. D, 99, 084026.
- Yalinewich, A., Steinberg, E., & Sari, R. (2015). Rich: Open-source hydrodynamic simulation on a moving voronoi mesh. The Astrophysical Journal Supplement Series, 216(2), 35.
- Zou, Y., Chamandy, L., Carroll-Nellenback, J., Blackman, E. G., & Frank, A. (2022). Jets from main sequence and white dwarf companions during common envelope evolution. , 514(2), 3041–3057.